The Pennsylvania State University

The Graduate School

MODELING, DESIGN, AND EXPERIMENTAL TESTING OF INTEGRATED FLUIDIC FLEXIBLE MATRIX COMPOSITE STRUCTURES

A Dissertation in

Mechanical Engineering

by

Bin Zhu

Submitted in Partial Fulfillment
of the Requirements
for the Degree of

Doctor of Philosophy

August 2014

The dissertation of Bin Zhu was reviewed and approved* by the following:

Christopher D. Rahn
Professor of Mechanical Engineering
Dissertation Co-Advisor, Co-Chair of Committee

Charles E. Bakis
Distinguished Professor of Engineering Mechanics
Dissertation Co-Advisor, Co-Chair of Committee

Martin W. Trethewey
Arthur L. Glenn Professor of Mechanical Engineering

Alok Sinha
Professor of Mechanical Engineering

George A. Lesieutre
Professor of Aerospace Engineering

Karen A. Thole
Professor of Mechanical Engineering
Department Head of Mechanical and Nuclear Engineering

*Signatures are on file in the Graduate School

ABSTRACT

Fluidic Flexible Matrix Composites (F^2MCs) consist of a highly anisotropic FMC laminate that encloses a working fluid. The FMC laminate is basically a composite shell that has reinforcements orientated at a particular angle with respect to the longitudinal axis. F^2MC tubes have been shown to provide actuation, stiffness change, and vibration reduction in applications that require isolated tubes or multiple tubes embedded in a soft matrix. Structural applications, however, often require stiff and strong materials. The objective of this research is to integrate relatively soft F^2MC tubes into rigid host structures, by either embedding or bonding, such that the F^2MC integrated structures can have tunable shape, stiffness, fluid pumping, vibration damping, or vibration absorption characteristics.

First, we explore the functionality of F^2MC tubes embedded into a stiff matrix. The geometry and anisotropy of the tube can be tailored for either highly leveraged fluid pumping under mechanical deformation or highly leveraged stiffness change by preventing fluid flow into or out of the tube. A bilayer analytical model is developed using Lekhnitskii's solution for an anisotropic tube under axial and pressure loading. The analysis shows a confining effect of the surrounding rigid matrix on the performance of F^2MC tubes. With tailoring of the tube wall thickness (thick) and wind angle (near-axial), however, F^2MC tubes can pump 250 times more fluid than a piston of the same diameter. Furthermore, axial stiffness can be increased by a factor of 2.2 when fluid flow is prevented.

Secondly, the actuation performance of F^2MC tubes embedded in structural media is investigated. The unit cell models examined are cylindrical and bi-layer with the inner layer being a thick walled F^2MC tube and the outer layer representing the surrounding rigid composite and composed of either homogeneous epoxy or a second FMC layer made with stiffer matrix material. The analytical models are validated using ABAQUS. The analytical results show that actuation performance is generally reduced compared to that of an isolated F^2MC tube due to the radial and longitudinal constraints. Free strain is generally two orders of magnitude smaller for an F^2MC tube in structural media, requiring higher actuation pressures for bi-layer F^2MC structures. The blocking force of F^2MC in either epoxy or composite is roughly an order of magnitude smaller than that of an isolated F^2MC tube.

Thirdly, we propose damping the vibration of a cantilever beam by bonding multiple F^2MC tubes to the beam and using the strain induced fluid pumping to dissipate energy. Transverse beam vibration strains the F^2MC tube and generates fluid flow through an energy dissipating

orifice. An optimally sized orifice maximizes energy dissipation, greatly reducing the resonant peaks and increasing modal damping. An analytical model is developed based on Euler-Bernoulli beam theory and Lekhnitskii's solution for anisotropic layered tubes. Using miniature tubes, a laboratory-scale F^2MC-integrated beam prototype is constructed and experimentally tested. The experimental results agree well with the theoretical predictions, provided the fluid bulk modulus is reduced to reflect the entrained air in the fluidic circuit. A design space study shows that damping ratios of 32% and 16% are achievable in the first and second modes of a cantilever beam, respectively, using an F^2MC damping treatment.

Finally, this research shows that F^2MC tubes with resonant fluidic circuits can absorb and isolate vibration at a specific frequency when bonded to flexible structures. The transverse structural vibration applies cyclic axial strain to the F^2MC tubes. The anisotropic elastic properties of the composite tube amplify the axial strain to produce fluid flow through a flow port and into an accumulator. The fluid inertance in the flow port (inertia track) and the stiffness of the accumulator are analogous to the vibration absorbing mass and stiffness in a conventional tuned vibration absorber or isolator. The collocated tip force to tip displacement analytical transfer function of the coupled system is derived for the vibration absorber analysis. For vibration isolation analysis, the tip force to base shear and moment transfer functions are derived. Experimental testing is conducted on a laboratory-scale F^2MC beam structure. The resonant peak becomes an absorber notch in the frequency response function if the inertia track length is properly tuned. Tuning the fluid bulk modulus and total flow resistance in the theoretical model produces results that match the experiment well, predicting a magnitude reduction of 35 dB at the first resonance using an F^2MC absorber. Based on the experimentally validated model, analysis results show that the cantilever beam vibration can be reduced by more than 99% with optimally designed tube attachment points and flow port geometry. The model also predicts 99.3% reduction of transmitted forces and moments from the tip force. For a given fluidic circuit design, however, the absorber, shear isolation, and moment isolation frequencies are different.

TABLE OF CONTENTS

LIST OF FIGURES

LIST OF TABLES

ACKNOWLEDGEMENTS

I am indebted to the following people. Without their help, the completion of this dissertation cannot be possible. So I would like to express the deepest appreciations to them.

I would like to first thank my advisor Dr. Christopher Rahn and co-advisor Dr. Charles Bakis for their guidance and mentoring during these years. Dr. Rahn, thank you for being patient and supportive, and enlightening my research with absorbing ideas and incisive remarks. I especially appreciate all the discussions during the one-on-one meeting, which are the foundation stones for this research. Dr. Bakis, thank you for offering valuable discussions and insightful comments along the way. Together with the mechanics classes I took with you, they are a great help in every aspect of my work. I also thank Dr. Martin Trethewey, Dr. Alok Sinha, and Dr. George Lesieutre for serving on my PhD committee.

Working in a big lab with extensive collaborations, I have met a lot of smart and helpful people. Suyi Li, thank you for your help in mathematical modeling and the comments in the EFRI meetings. Lloyd Scarborough, thanks for showing me the instruments in the lab and your help in the modal analysis experiments. Kentaro Miura, it was a pleasure to meet you and I enjoyed working with you on the final project, and the discussions as well as jokes about F^2MC. Thank you to all of my lab-mates and colleagues: Deepak Trivedi, Hareesh Kommepalli, Zheqian Zhang, Kiron Mateti, Thomas Levard, Paul Diglio, Ying Shi, Githin Parsad, Zheng Shen, Varma Gottimukkala, Chinmay Rao, Nick Kurczewski, Chris Ferone, Michael Robinson, Rory Byrne-Dugan, Chris Melville, Xiaokun Ma, Tanvir Tanim, Dan Aglione, Matt Krott, Shawn Treacy, Aniruddh Vashisth, Ben Wimmer, Pat Mangiagli.

Finally, I want to thank my parents, Zhu Jinquan and Wang Mingying, for believing in me, trusting me unconditionally, and supporting me as best they can. I thank my dear wife, Zhiyao Ye, for accompanying me in US, offering me comfort and endless encouragement, sharing important moments with me throughout my PhD life. Finally, I thank my dear son, Nolan J. Zhu, for inspiring me to finish up the writing of this dissertation in the joy of being a new dad.

Chapter 1

Introduction

Fluidic Flexible Matrix Composites (F^2MCs) consist of a highly anisotropic FMC laminate enclosing a working fluid. The FMC laminate is basically a composite shell that has reinforcements oriented at +/- $\alpha°$ with respect to the longitudinal axis. It can be manufactured in several ways such as filament winding, extrusion/braiding process, and bonding a braided sleeve over a rubber tube. F^2MC tubes have been shown to provide actuation, stiffness change, and vibration reduction in applications that require isolated tubes or multiple tubes embedded in a soft matrix. However, structural applications often require stiff and strong materials. So the motivation of this research is to integrate relatively soft F^2MC tubes into rigid host structures, by either embedding or bonding, such that the F^2MC integrated structures can have tunable and multi-functional properties such as shape change, variable stiffness, fluid pumping, vibration damping, and vibration absorption. This investigation is the first to explore the potential of F^2MC composites as structural materials that can provide the stiffness and strength required of many engineering applications. This part is a background introduction of F^2MC technology as well as the areas it can be applied to. It covers topics such as the development of F^2MC concept, smart/active actuators, vibration control devices, tuned vibration absorber (TVA), vibration damping treatments, harmonic resonance control, experimental modal analysis, and so on.

1.1 Background of Fluidic Flexible Matrix Composite

Actuators for smart structures are often electrically driven, such as shape memory alloy, shape memory polymer, piezoelectric ceramic, magnetostrictive material with Terfenol-D, and

electroactive polymers (Gandhi and Thompson, 1992). Fluid powered actuators, however, can have much higher power and energy density (Zupan, 2002) but suffer from the well-known disadvantages of fluid pressurization, plumbing, pistons, and valves. Recently, researchers have developed "Fluidic Flexible Matrix Composite" (F^2MC) tubes that have the advantages of traditional fluid actuators without the wear, friction, and leakage of pistons. In addition, F^2MC tubes are compatible with structural composites, providing a pathway to the practical realization of hydraulic smart structures.

Philen *et al.* (2007) show that an F^2MC tube can elongate or contract in response to internal pressure depending on whether the fiber winding angle is greater or less than 55 °, respectively (see Figure 1-1). Large strokes and forces are attainable in the free contraction/elongation and blocked configurations, respectively, for relatively small applied pressure. The nonlinear, elastic model developed by Liu and Rahn (2003) for McKibben actuators (Chou and Hannaford, 1994, 1996; Tondu and Lopez, 2000; Tsagarakis and Caldwell, 2000; Kothera *et al.*, 2009; Zhang and Philen, 2012) also applies to F^2MC tubes and can predict the contraction/elongation strain and blocked force.

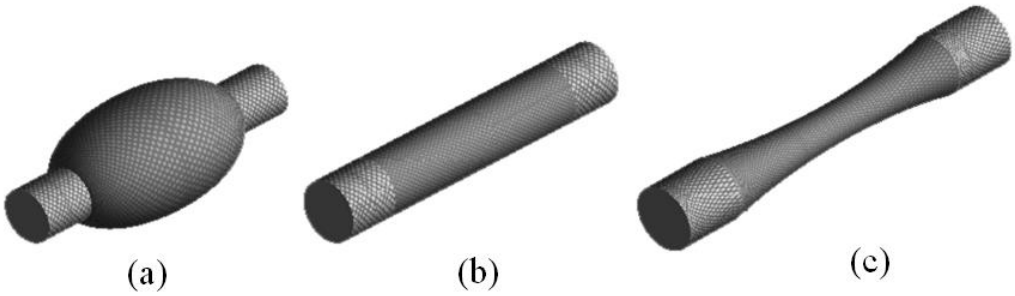

Figure 1-1. Actuation of an F^2MC tube: (a) Pressurized contractor tube with a fiber winding angle less than 55 °, (b) Unpressurized tube, and (c) pressurized tube with a fiber winding angle greater than 55 °. [The figure is originally from the article by *Philen et al.* (2007)]

F^2MC tubes have the same advantages associated with McKibben actuators, including high power-to-weight ratio and low cost (Caldwell *et al.*, 1995; Daerden and Lefeber, 2002; Woods *et al.*, 2011; Davis *et al.*, 2003). In addition, the fiber angle, shape, and dimensions of F^2MC tubes

can be more precisely controlled and fabricated using a filament winding process than the braided sleeve over rubber tube design of McKibben actuators. Filament winding can also make F^{2}MC tubes with multiple layers wound at different angles or extremely small fiber angles, which are difficult to accomplish with McKibben actuators.

1.2 Variable Properties of F^{2}MCs

An F^{2}MC tube can elongate or contract as a result of internal pressure depending on the wind angle α. Conversely, stretching an F^{2}MC contractor causes the interior volume to decrease and, if flow is not constricted, fluid is pumped out of the tube. An extender, on the other hand, increases in volume when stretched. Shan *et al.* (2006) studied the nonlinear-elastic axisymmetric deformation of F^{2}MC tubes using large deformation theory. Figure 1-2 shows how a variable stiffness adaptive structure can be achieved using an F^{2}MC tube with a flow restricting valve.

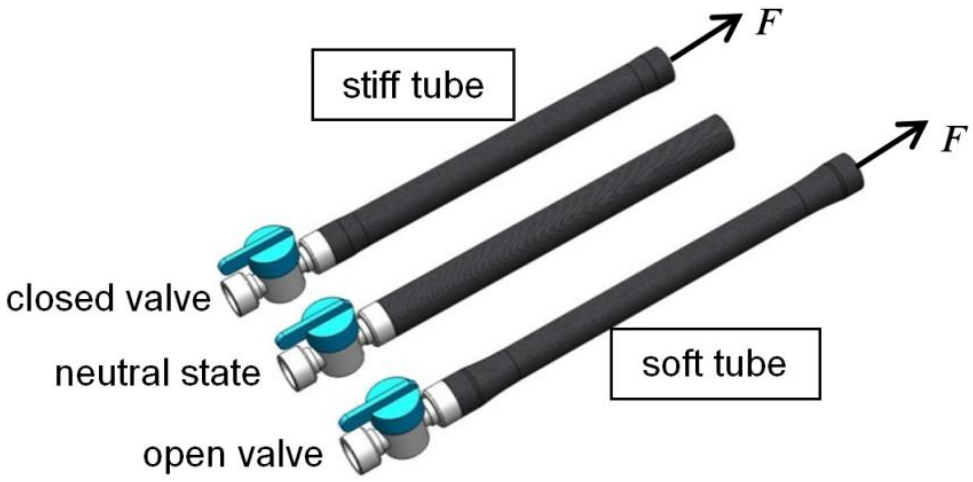

Figure 1-2. Variable stiffness F^{2}MC tubes via valve control

F^{2}MC tubes can also be integrated into structures. Philen *et al.* (2006) embed F^{2}MC tubes in a soft matrix to develop a variable stiffness beam structure with valve control. Shell theory is used to derive the effective elastic modulus of the tube for open and closed valves. Shan *et al.*

(2009) add wall and fluid compliance with a 3-D elasticity model of the F^2MC tube. They show that by tailoring material properties such as the Young's modulus of the fibers and resin and the fiber angle, one can generate F^2MC structures with wide-ranging stiffness and stiffness variability by controlling fluid flow into and out of the tube. Zhang *et al.* (2010) designed and built an artificial fish with pneumatically driven FMC actuators, demonstrating the promising use of F^2MC tubes for distributed actuation.

1.3 Damping Treatment for Beam Structures

Vibration damping can suppress excessive vibration, minimize discomfort to humans, position control errors, fatigue and failure, which are especially prevalent under resonant forcing. Vibration damping mechanisms include tuned mass dampers (TMD), viscoelastic layers, magnetic (eddy current) dampers, and piezoelectrics with shunt circuits (Johnson, 1995; Viana and Steffen, 2006). These techniques enable the system to convert mechanical energy to thermal or electrical energy and greatly reduce the resonant amplitudes.

Vibration control devices are mainly divided into three categories: passive, active, and semi-active. Preconfigured passive devices have been proven to very effectively attenuate the vibrations of machinery, buildings, and other mechanical structures. They do not require external power, low cost and relatively simple to implement (Soong and Constantinou, 1994). Active vibration control devices require power and feedback sensors but can provide high performance and accuracy. Semi-active devices utilize a combination of passive and active techniques. The system properties of semi-active devices, such as stiffness and damping, can be varied to reduce vibration using low power input.

Cantilever beams are very commonly utilized in mechanical and civil structures, including bridges, buildings, and aircraft wings. Bailey and Hubbard (1985) pioneered active vibration

damping using piezoelectric polymers to attenuate the vibration of a thin cantilever. Piezoelectric materials (Hollkamp, 1994; Tsai and Wang, 1999; Lin and Nien, 2005) have been embedded in and bonded to beam structures for vibration suppression using a variety of control techniques. Bae *et al.* (2005) showed that an eddy current damper, consisting of a permanent magnet and a conducting sheet, creates damping forces from the relative motion of these two components. Researchers (Baz and Ro, 1994; Lam *et al.*, 1997; Nakra, 1998) have also used constrained layer damping (CLD) treatments to reduce the vibration of cantilever beams. Mechanical energy is dissipated by shearing a viscoelastic layer. CLD treatments, however, can be heavy and bulky and sensitive to changes in temperature, excitation frequency, and strain amplitude.

1.4 Vibration Absorber for Beam Structures

Tuned Vibration Absorbers (TVAs) are important vibration control devices with many applications in vehicles, consumer products, and HVAC devices. They have been proven to effectively reduce or eliminate the vibration of harmonically excited machines and structures at low cost and with a simple, typically passive design (Harris and Piersol, 2002). The concept of TVA was first invented by Frahm (1911) and later developed by a number of researchers (Ormondroyd and Hartog, 1928; Roberson, 1952; Hunt and Nissen, 1982, Hartog, 1985). Vibration absorbers consist of spring and mass elements that are attached to vibrating master structures and tuned to counteract an applied sinusoidal excitation at a specific absorption frequency (Rusovici et al., 2002). For undamped TVAs, the frequency response of the combined system has a notch with small vibration amplitude at the absorption frequency. Damped TVAs, also known as tuned mass dampers (TMDs), can smooth out the sharp harmonic peaks in the frequency response and increase the working range of the vibration absorber (Igusa and Xu, 1994; Rana and Soong, 1998).

TVAs can be passive, semi-active, or active (Sun *et al.*, 1995). Passive vibration absorbers do not require external power (Soong and Dargush, 1997) and work most effectively in steady state operating conditions. They may become mistuned and lose effectiveness if the operating environment changes over time, however. Active vibration absorbers require power and feedback sensors to dynamically tune the TVA properties and provide high performance and accuracy (Lee and Sinha, 1986). Semi-active vibration control techniques combine passive and active techniques to adapt the TVA response to changing conditions (Walsh and Lamancusa, 1992; Koo *et al.*, 2004).

Active and semi-active TVAs can involve smart materials such as shape memory alloys (SMAs), piezoelectric materials, magnetorheological elastomers (MREs) and electrorheological fluids (Housner *et al.*, 1997; Preumont, 2002). For example, Williams *et al.* (2002) present the design and testing of an adaptive TVA with shape memory alloys. Hagood and von Flotow (1991) demonstrate the use of piezoelectric materials for energy dissipation with passive electrical circuits. Resonant circuit shunting exhibited behavior that was very similar to a mechanical TVA. Hollkamp and Starchville (1994) present a piezoelectric vibration absorber that is capable of self-tuning to a targeted structural mode. Davis *et al.* (1997) show the development of capacitive and resistive shunting to alter the natural frequency and damping characteristic of a piezoceramic vibration absorber. Deng *et al.* (2006) develop an adaptive TVA with magnetorheological elastomers by taking advantage of their variable modulus property under different magnetic fields.

TVAs have been applied to beam structures for vibration suppression. Cantilever beam structures are widely used in various mechanical and civil applications including bridges, buildings, and aircraft wings. Early works on the integration of TVAs into beam systems for vibration reduction can be found in (Young, 1952; Snowdon, 1966; Jacquot, 1978; Kitis et al., 1983; özgüven and çandir, 1986). Afterwards, Esmailzadeh and Jalili (1998) modeled a structurally damped beam with arbitrary number of absorbers under distributed harmonic loading.

The Timoshenko beam theory was used to take into account the rotary inertia and shear deformation effects. Lin and Liu (2006) designed a piezoelectric vibration absorber and reduced the vibration of a cantilever beam using a fuzzy logic controller.

Fluid motion can also be used to reduce the vibration of structures. For instance, tuned liquid column dampers (TLCDs) absorb and dissipate mechanical energy through sloshing water in tall buildings (Sakai et al., 1989; Yalla and Kareem, 2000, 2003). TLCDs are low cost and have few maintenance requirements (Gao and Kwok, 1997; Sadek et al., 1998). The Liquid Inertia Vibration Eliminator (LIVE) system (Halwes, 1980) suppresses vibration by using the inertia forces from the acceleration of fluid through flow ports.

1.5 Vibration Isolation for Beam Structures

Vibration isolators are another kind of vibration control devices that can reduce vibration effectively (Sciulli, 1997; Rivin, 2003). This is especially true when the forces due to vibration are of concern. There are two working modes (Rao and Yap, 1995) for vibration isolation. Firstly, vibration isolators are used to protect delicate instruments from the unwanted vibrations transmitted from the environment. Secondly, vibration isolators can stop the forces from being passed on from vibrating machines to the ground or the base. During the vibration isolation process, resilient members (*e.g.* spring and elastomer) are usually inserted between the isolated system and the source of vibration. Under certain vibration conditions of the external excitation, the dynamic response of the protected structure can be greatly reduced because of the low force transmissibility of the resilient members. Energy dissipation mechanisms (*e.g.* viscous damper) can be integrated into the vibration isolator to introduce damping. The existence of damping generally reduces the vibration amplitude of amplification region and increases the vibration amplitude of isolation region in the transmissibility plot (Crede and Ruzicka, 1996).

A variety of vibration isolation systems, either passive or active, have been developed for vibration suppression in applications such as aerospace structures (Rita *et al.*, 1978; Ibrahim, 2008; Hiemenz *et al.*, 2008), machinery (Rivin, 1995), automotive systems (Miller, 1988), and buildings and seismic structures (Makris and Constantinou, 1992; Beard *et al.*, 1994). Like other vibration control devices, vibration isolation systems can be passive, semi-active, and passive. For example, Karnopp *et al.* (1974) developed the concept of semi-active isolation for vibration control. With numerical simulations, comprehensive comparisons were conducted among the three vibration control techniques. After two decades, Karnopp (1995) reviewed the development of active and semi-active vibration isolation and illustrated their unique characteristics with the practical application in seismic platforms and automotive suspension systems. Sciulli and Inman (1998) explored the design of isolation systems with a flexible foundation, emphasizing the effect of mount frequency on the isolation design. Kim *et al.* (2001) investigated a four-mount vibration isolation system with electromagnetic actuators and decentralized control method.

Fluidlastic devices have long been used in rotorcraft and vehicles to isolate excessive vibration. These devices usually include an elastomeric diaphragm that pumps fluid through a long, thin port. The area ratio between the diaphragm and the port amplifies the fluid motion to produce large acceleration. The inertia forces that are developed can be large enough to cancel the vibration loads despite the relatively low fluid mass. The Liquid Inertia Vibration Eliminator (LIVE) system was introduced by Halwes (1980) to reduce vibration at a specific frequency by utilizing fluid inertia forces from the internal fluid pumping. Smith and Redinger (1999) demonstrated the application of the LIVE isolator onto the Bell model 427 helicopter for rotor vibration suppression. Du Plooy *et al.* (2005) employed tunable pneumatic springs to develop an adaptive vibration isolator based on the LIVE system. More research on fluidlastic isolation devices can be found in (Hodgson and Duclos, 1990; Jones and Downing, 1993; Smith and Stamps, 1995; McGuire, 2003).

1.6 Potential of F^{2}MC for Vibration Applications

The F^{2}MCs have recently been developed with great potential for vibration damping. The basic building block of F^{2}MC is the F^{2}MC tube, which consists of a highly anisotropic FMC laminated tube filled with a working fluid. Zhu *et al.* (2011) embedded F^{2}MC tubes in a rigid matrix and investigated properties such as fluid pumping and variable stiffness. With a thick shell wall and a near-axial fiber angle, the pumping ability of over 100 times that of a piston with the same diameter is achievable for isolated F^{2}MC tubes. Later, Zhu *et al.* (2012) also studied the actuation performance of F^{2}MC tubes incorporated into structural media. The F^{2}MC tube can be tailored to minimize the constraining effect of the rigid matrix. Wimmer *et al.* (2012) experimentally investigate the actuation performance of multi-layer composites, revealing the necessity of considering shear lag and end effects when using thick F^{2}MC tubes of a limited length.

A key advantage of F^{2}MC tubes is their excellent fluid pumping ability compared with a piston pump, which can provide energy dissipation and fluid inertia (inertance) when coupled with external fluidic circuits, and therefore can be used for vibration reduction applications. For example, Lotfi-Gaskarimahalle *et al.* (2009) demonstrated analytically and experimentally that an F^{2}MC tube and an inertia track reduce vibration at a specific frequency. Scarborough *et al.* (2012) showed that F^{2}MC tubes can be used as vibration isolators, limiting the forces transmitted through a load carrying member. Li and Wang (2012) explored the use of a dual F^{2}MC cellular structure for vibration absorption and improved actuation performance relative to a single tube in a certain frequency range. Philen (2011) designed an F^{2}MC-based semi-active isolation mount for reducing transmissibility and tuning the resonant frequency and damping with a proportional valve.

1.7 Experimental Modal Analysis

Experimental modal analysis, or modal testing, is an experimental technique to acquire the dynamic characteristics of machines and structures (Schwarz and Richardson, 1999; Allemang, 1999; Avitabile, 2001). Structural properties like natural frequency, damping and mode shapes can be determined by measuring the frequency response function of the structures under vibrational excitation. A typical modal testing system consists of transducers (*e.g.* load cells, accelerometers), A/D converters, a data acquisition system, computers with FFT analyzer, an impact hammer or an electromagnetic shaker, and an amplifier and D/A converters if a shaker is used (Ewins, 1995; He and Fu, 2001). The experimental modal analysis of a cantilever beam can be found in the article by Cafeo *et al.* (1992).

1.8 Overview of Present Work

The objective of this research is to incorporate multi-functional Fluidic Flexible Matrix Composite tubes into structural media, and mechanical and civil structures for tunable properties such as shape and stiffness change, vibration damping, and vibration absorption. In particular, Chapter 2 studies a composite structure consisting of an F^2MC tube embedded in epoxy to investigate the impact of confining structural media on the capacity of F^2MC tubes to pump fluid and change stiffness. The F^2MC tubes are highly tailorable elements and therefore the research focuses on the design of the tubes to achieve maximal fluid pumping and variable stiffness.

Chapter 3 addresses the actuation behavior of F^2MC tubes embedded in structural media. The unit cell investigated is cylindrical and bi-layer with the inner layer being a thick walled F^2MC tube and the outer layer representing the surrounding rigid composite and composed of either homogeneous epoxy or a second FMC layer made with stiffer matrix material. Two

analytical models, for free strain and blocked force respectively, are developed based on Lekhnitskii's solutions for a homogeneous orthotropic cylinder with axial force and pressure loading. Parametric studies are carried out to maximize the actuation performance of F^2MC integrated composite structures. The models are also validated with finite element analysis results in ABAQUS.

In Chapters 4 and 5, the integration of F^2MC tubes into cantilever beam structures for vibration suppression is examined. Such an investigation is valuable for exploring the potential utilization of F^2MC tubes integrated into beam/plate structures for extensive vibration reduction, which has never been investigated before. Cantilever beams are very commonly utilized in mechanical and civil structures such as bridges, buildings, and aircraft wings. The vibration reduction of these structures is critical because it can minimize or eliminate the discomfort to humans, possibility of crack formation, unpleasant noise, fatigue and failure.

Chapter 4 proposes a novel approach for damping the resonances of a cantilever beam by bonding an F^2MC tube onto the beam and taking advantage of the tube's substantial fluid pumping ability. This is achieved by coupling the transverse vibration of the cantilever beam with the stretching/ or compression action of the F^2MC tube. The induced fluid volume is then pumped into an external accumulator via an orifice, which resists the flowing motion and dissipates energy. The energy dissipation is especially significant at the resonances of the cantilever beam, where the beam vibrates with greatest amplitude. Consequently, the magnitude of the resonances can be greatly reduced due to the damping introduced by the F^2MC tube. An analytical model is developed based on Euler-Bernoulli beam theory and Lekhnitskii's solution for anisotropic layered tubes. In order to maximize the vibration reduction, a parametric study and design space investigation are performed.

Inspired by the damping treatment investigation in Chapter 4, Chapter 5 further explores the potential of an F^2MC absorber and/or isolator for a cantilever beam by introducing a tunable

flow port/or inertia track and an external accumulator. The strain induced volume change in the F^2MC tubes forces fluid through the flow port and into the accumulator. The fluid inertance in the flow port (inertia track) and the stiffness of the accumulator are analogous to the vibration absorbing mass and stiffness in a conventional tuned vibration absorber/isolator. The large pressure that is built up inside the F^2MC tube pumps the fluid volume through the flow port with large acceleration. The D'Alembert forces that are developed, which equal to mass times acceleration, can be large enough to cancel the vibration loads and therefore greatly attenuate the vibrations. A mathematical model is developed to derive the collocated tip force to tip displacement, and also tip force to shear force and moment at base, transfer functions of the coupled system. In order to validate the models in Chapters 4 and 5, lab-scale F^2MC beam structures with different fluidic circuits were constructed using custom made miniature tubes. Modal testing was performed on those F^2MC beam prototypes and the experimental results were compared with the theoretical predictions. After the model validation, design space investigation was further performed to maximize the absorption and isolation effects of the F^2MC beam structures.

Chapter 2

Tailored Fluidic Composites for Stiffness or Volume Change

Stiffness change is a measure of the control authority of the F^2MC tube and volume change or fluid pumping measures the potential for inertance generation by the F^2MC tube for vibration isolation and absorption. The previous research on F^2MC composites, however, is limited to individual tubes or tubes embedded in a rubbery matrix. The current investigation focuses on tailoring the design of a composite consisting of F^2MC tubes embedded in a rigid matrix to maximize stiffness and/or volume change. This work is the first to explore the potential of F^2MC composites as structural materials that can provide the stiffness and strength required of many engineering applications. It focuses on the constraining effect of a surrounding rigid matrix on the fluid pumping and variable stiffness performance of an F^2MC tube. A unit cell, composed of an inner F^2MC tube and an outer epoxy layer, is designed and analyzed. A parametric study explores the potential for fluid pumping and variable stiffness functionality in a rigid composite structure.

2.1 Analytical Model and Solutions

2.1.1 Bi-layer F^2MC Cell Model

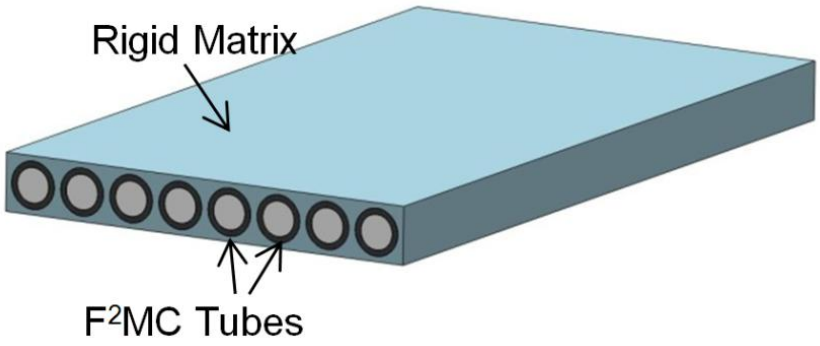

Figure 2-1. F^{2}MC tubes in a composite plate

To investigate the fluid pumping and variable stiffness of F^{2}MC tubes incorporated into structural media, a composite plate is considered as shown in Figure 2-1. The matrix material, assumed to be epoxy, represents a typical structural medium that is stiff in comparison to the flexible matrix used in the F^{2}MC tubes. It is reasonable to expect that the pumping and stiffness change performance will decrease with increasing matrix volume fraction. Thus, we assume that the F^{2}MC tubes are arranged side by side in a square array and then cast in epoxy resin, resulting in a unit cell as shown in Figure 2-2, similar to the layout of fibers in traditional composites. The unit cell is approximated by two concentric homogeneous cylinders, following a Concentric Cylinder Model (CCM) approach (Hashin and Rosen, 1964). The outer radius of the matrix layer of the CCM is calculated by maintaining the same area fraction as the square unit cell,

$$\frac{a_3}{a_2} = \sqrt{\frac{4}{\pi}} = 1.13\,, \tag{2.1}$$

where a_1 and a_2 are the inner and outer radii of the F^{2}MC tube and a_3 is the radius of the outer, epoxy layer with Young's modulus E and Poisson's ratio v (Figure 2-2). An axial force F_{ext} applied at the ends of the unit cell produces a uniform axial strain ε_{z0}.

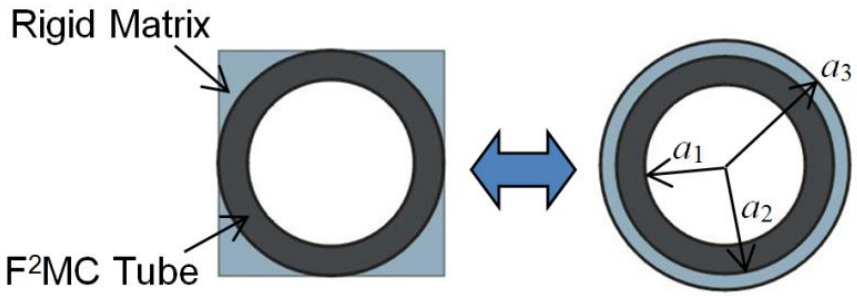

Figure 2-2. Cross section of a unit cell and concentric cylinder approximation

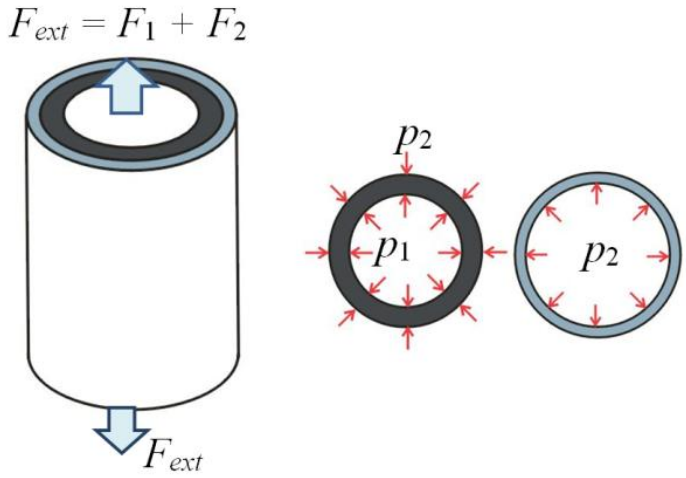

Figure 2-3. External loadings on whole structure and individual layers

Fiber reinforcement of the F^{2}MC tube causes internal fluid volume change with axial strain. The magnitude of this effect depends on the lamina property, lay-up sequence, tube geometry, and external loading. If the volume inside the tube is not constrained, fluid flows into or out of the F^{2}MC tube under axial strain. If the volume is fixed in a closed valve case then the internal volume becomes pressurized at p_1 relative to the external, atmospheric pressure. As a result, the F^{2}MC tube becomes stiffer and requires much higher axial force to achieve same amount of axial strain ε_{z0}. Figure 2-3 shows that the axial force F_{ext} equals the sum of the forces from the inner

FMC tube, F_1, and the outer epoxy layer, F_2. The FMC tube is assumed to be perfectly bonded to surrounding epoxy, generating contact pressure p_2 between the two layers under axial forcing.

The FMC tube is acted on by the axial force F_1, internal pressure p_1, and external pressure p_2. Lekhnitskii's solution for a homogenous orthotropic cylinder with this loading (Lekhnitskii, 1963) is used to obtain the axisymmetric stress and strain distributions

$$\sigma_r^{(i)} = \frac{p_1 c^{k+1} - p_2}{1 - c^{2k}} \rho^{k-1} + \frac{p_2 c^{k-1} - p_1}{1 - c^{2k}} c^{k+1} \rho^{-k-1} + CK\left(1 - \frac{1-c^{k+1}}{1-c^{2k}} \rho^{k-1} - \frac{1-c^{k-1}}{1-c^{2k}} c^{k+1} \rho^{-k-1}\right), \quad (2.2)$$

$$\sigma_\theta^{(i)} = \frac{p_1 c^{k+1} - p_2}{1 - c^{2k}} k\rho^{k-1} - \frac{p_2 c^{k-1} - p_1}{1 - c^{2k}} k c^{k+1} \rho^{-k-1} + CK\left(1 - \frac{1-c^{k+1}}{1-c^{2k}} k\rho^{k-1} + \frac{1-c^{k-1}}{1-c^{2k}} k c^{k+1} \rho^{-k-1}\right), \quad (2.3)$$

$$\sigma_z^{(i)} = C - \frac{1}{a_{33}}\left(a_{13}\sigma_r^{(i)} + a_{23}\sigma_\theta^{(i)}\right), \quad (2.4)$$

where

$$c = \frac{a_1}{a_2}, \rho = \frac{r}{a_2}, \quad (2.5)$$

$$k = \sqrt{\frac{\beta_{11}}{\beta_{22}}}, \quad (2.6)$$

$$K = \frac{a_{23} - a_{13}}{\beta_{11} - \beta_{22}}, \quad (2.7)$$

and

$$\beta_{11} = a_{11} - \frac{a_{13}^2}{a_{33}} \text{ and } \beta_{22} = a_{22} - \frac{a_{23}^2}{a_{33}}. \quad (2.8)$$

The a_{ij} are the 3-dimensional effective compliance terms for the FMC tube wall obtained in the cylindrical coordinate system (Sun and Li, 1988). The FMC lamina is assumed to be transversely isotropic, so there are five independent elastic constants: Longitudinal Young's modulus E_1, transverse Young's modulus E_2, Poisson's ratios ν_{12} and ν_{23}, and shear modulus G_{12}.

The variable C is obtained from equilibrium in the axial direction,

$$F_1 = 2\pi \int_{a_1}^{a_2} \sigma_z^{(i)} r dr. \tag{2.9}$$

The strain distributions are calculated,

$$\varepsilon_r^{(i)} = a_{11}\sigma_r^{(i)} + a_{12}\sigma_\theta^{(i)} + a_{13}\sigma_z^{(i)}, \tag{2.10}$$

$$\varepsilon_\theta^{(i)} = a_{12}\sigma_r^{(i)} + a_{22}\sigma_\theta^{(i)} + a_{23}\sigma_z^{(i)}, \tag{2.11}$$

$$\varepsilon_z^{(i)} = a_{13}\sigma_r^{(i)} + a_{23}\sigma_\theta^{(i)} + a_{33}\sigma_z^{(i)}. \tag{2.12}$$

Axial force resultant F_2 and contact pressure p_2 act on the outer epoxy layer modeled as a hollow, isotropic cylinder. The stress distribution is

$$\sigma_r^{(o)} = \frac{p_2 a_2^2}{a_3^2 - a_2^2} - \frac{a_3^2 a_2^2}{r^2(a_3^2 - a_2^2)} p_2, \tag{2.13}$$

$$\sigma_\theta^{(o)} = \frac{p_2 a_2^2}{a_3^2 - a_2^2} + \frac{a_3^2 a_2^2}{r^2(a_3^2 - a_2^2)} p_2, \tag{2.14}$$

$$\sigma_z^{(o)} = \frac{F_2}{\pi(a_3^2 - a_2^2)}. \tag{2.15}$$

The strains follow from Hooke's law

$$\varepsilon_r^{(o)} = \frac{1}{E}[\sigma_r^{(o)} - \nu(\sigma_\theta^{(o)} + \sigma_z^{(o)})], \tag{2.16}$$

$$\varepsilon_\theta^{(o)} = \frac{1}{E}\left[\sigma_\theta^{(o)} - \nu\left(\sigma_r^{(o)} + \sigma_z^{(o)}\right)\right], \tag{2.17}$$

$$\varepsilon_z^{(o)} = \frac{1}{E}\left[\sigma_z^{(o)} - \nu\left(\sigma_r^{(o)} + \sigma_\theta^{(o)}\right)\right]. \tag{2.18}$$

2.1.2 Boundary Conditions

The axial boundary conditions are that the axial strains in both the FMC laminate and epoxy layer equal ε_{z0}, or

$$\varepsilon_z^{(i)} = \varepsilon_{z0}, \tag{2.19}$$

and

$$\varepsilon_z^{(o)} = \varepsilon_{z0}. \tag{2.20}$$

In the radial direction, the assumption of perfect bonding between layers means that the hoop strains at the interface are equal,

$$\varepsilon_\theta^{(i)}|_{r=a_2} = \varepsilon_\theta^{(o)}|_{r=a_2}. \tag{2.21}$$

2.1.3 Open Valve Solution

When the valves are open to allow fluid flow with longitudinal loading, the volume change can be calculated. The internal pressure of F^{2}MC tube in this case is

$$p_1 = 0. \tag{2.22}$$

The preceding equations and boundary conditions are solved for F_1 and p_2. Substitution of these solutions into Equations (2.11) and (2.12) produces the hoop and axial strain distributions of the F^{2}MC structure. The volume change ratio, defined as fluid volume change divided by the original fluid volume, is

$$\frac{\Delta V}{V} = \varepsilon_z^{(i)}|_{r=a_1} + 2\varepsilon_\theta^{(i)}|_{r=a_1}, \tag{2.23}$$

where higher order strain terms have been neglected. For comparison, the volume change of an F^{2}MC tube is compared with that of a piston-cylinder which has $\Delta V/V = \varepsilon_{z0}$ by introducing the pumping factor

$$P = \frac{\Delta V/V}{\varepsilon_{z0}}. \tag{2.24}$$

Pumping factor P illustrates the pumping ability of an F^{2}MC tube compared with the piston-cylinder pumping system. The larger pumping factor an F^{2}MC tube has, it is more capable of pumping fluid.

2.1.4 Closed Valve Solution

In the closed-valve scenario, internal pressure p_1 develops as the volume changes due to axial loading as follows:

$$B\left(\frac{\Delta V}{V}\right) = B\left(\varepsilon_z^{(i)}|_{r=a_1} + 2\varepsilon_\theta^{(i)}|_{r=a_1}\right) = -p_1, \tag{2.25}$$

where B is the bulk modulus of the working fluid. Equation (2.25), combined with the three boundary conditions, can be solved for the four unknowns: force resultants F_1 and F_2, internal pressure p_1, and contact pressure p_2. The external axial force is then found using

$$F_{ext} = F_1 + F_2 - p_1\pi a_1^2. \tag{2.26}$$

In the open-valve scenario, the external axial force equals the sum of force resultants F_1 and F_2.

Defining the effective axial modulus of elasticity of the F^{2}MC cell in either scenario as

$$E_z = \frac{F_{ext}/\pi a_3^2}{\varepsilon_{z0}}, \tag{2.27}$$

the closed-to-open valve modulus ratio is then

$$R = \frac{E_z^{closed}}{E_z^{open}} = \frac{F_{ext}^{closed}}{F_{ext}^{open}}. \tag{2.28}$$

2.2 Results and Discussion

This study focuses on the ability of an F^{2}MC composite to pump fluid and change stiffness using the non-dimensional pumping factor P and modulus ratio R, respectively. The non-dimensional variables of interest include the F^{2}MC thickness ratio c, outer layer modulus E, and fiber angle α. The epoxy layer thickness is assumed to be the minimum value in Equation (2.1). The baseline parameters are listed in Table 2-1. The inner FMC lamina properties are referred to this experimental investigation (Shan, 2006).

Table 2-1. Baseline parameters for F^{2}MC structure

Lamina Property (Inner FMC)		**Epoxy Property (Outer Layer)**		**Geometry**	
E_1 (GPa)	115	E (GPa)	4.3	a_1 (mm)	0.7 a_2
E_2 (MPa)	18	ν	0.35	a_2 (mm)	(0→∞)
ν_{12}	0.33			a_3 (mm)	1.13 a_2
ν_{23}	0.93	**Fluid Property**		α (°)	(0→90)
G_{12} (MPa)	14.4	B (GPa)	2	ε_{z0}	0.001

2.2.1 Volume Change

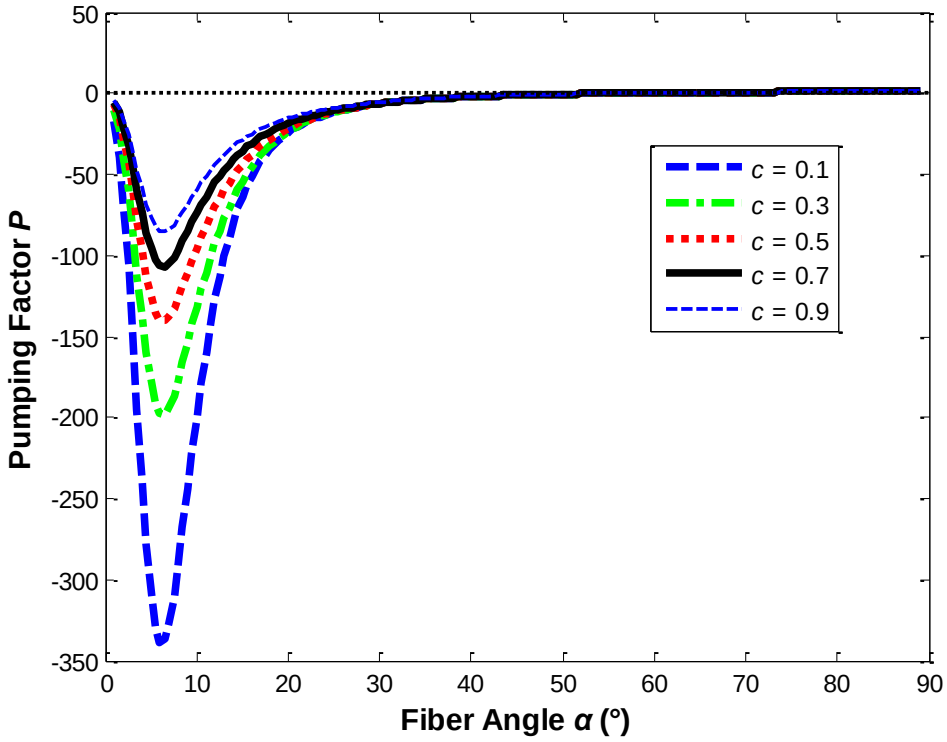

Figure 2-4. Fluid pumping factor of an F^{2}MC tube versus fiber angle for several wall thicknesses: c = 0.1 (dashed), c = 0.3 (dash-dotted), c = 0.5 (dotted), c = 0.7 (solid), and c = 0.9 (small dashed).

Figures 2-4 and 2-5 illustrate the fluid pumping capability of F^2MC tubes and F^2MC tubes in epoxy, respectively. The fiber angle varies from 0 to 90 degrees and the parameter c varies from 0.1 (thick wall) to 0.9 (thin wall), as the F^2MC wall thickness decreases. Figure 2-4 shows that the pumping factor for an F^2MC tube increases with wall thickness and peaks at a nearly-axial fiber orientation. The maximum pumping factor of -338 is achieved with $c = 0.9$ and $\alpha = 6°$, indicating that the tube volume shrinks 338 times faster than a piston of the same diameter. This huge amplification comes from the combination of the large radial contraction associated with the small fiber angle and the small initial volume.

The fluid pumping factor plotted in Figure 2-5 is for an F^2MC tube with an outer epoxy layer that constrains the pumping effectiveness. The pumping factor again decreases with decreasing wall thickness. The thick walled case ($c = 0.1$) has the largest pumping factor. The maximizing fiber angles are small but larger than for the tube without epoxy reinforcement. Thin-walled structures ($c = 0.9$) have a maximum pumping factor of -4.4 with fiber angles around 22.5^o. The thick walled structure ($c = 0.1$) has a maximum pumping factor of -270 at $\alpha = 6.5^o$. The maximum thin-walled and thick-walled pumping factors in Figure 2-5 are 5% and 80%, respectively, of the corresponding F^2MC tube pumping factors in Figure 2-4. This indicates that a thick-walled F^2MC tube reduces the constraining effect of the epoxy layer.

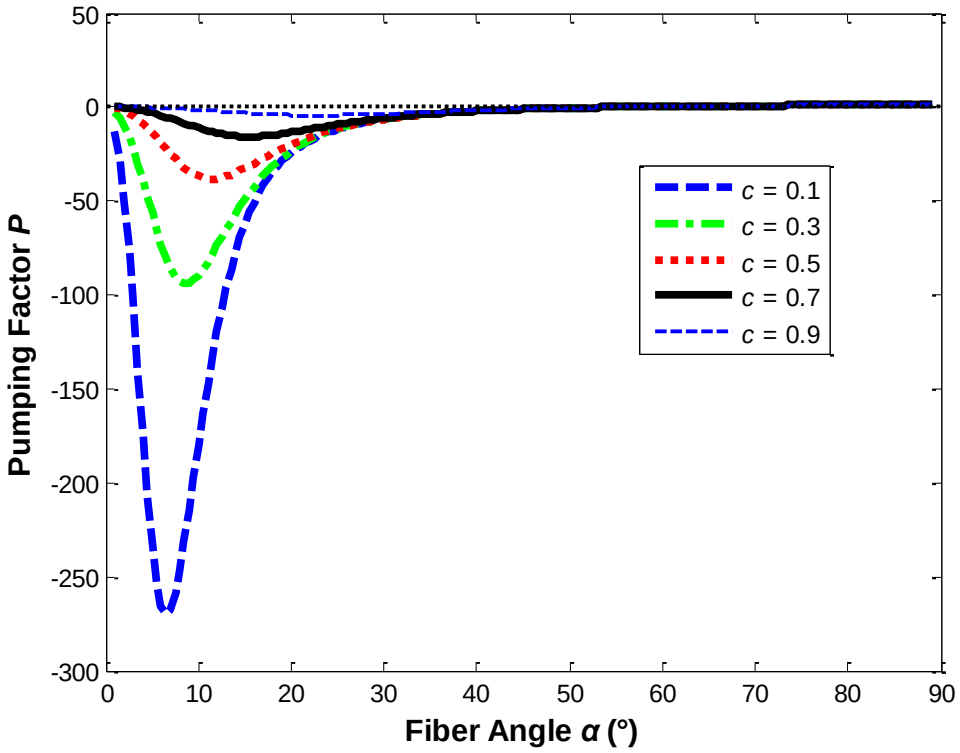

Figure 2-5. Fluid pumping factor of an F^{2}MC tube in epoxy versus fiber angle for several wall thicknesses: c = 0.1 (dashed), c = 0.3 (dash-dotted), c = 0.5 (dotted), c = 0.7 (solid), and c = 0.9 (small dashed).

As expected, increasing the thickness and/or Young's modulus of the epoxy in the F^{2}MC structure constrains the pumping factor. Figure 2-6 shows, for example, that varying the Young's modulus of the epoxy from 1 GPa to 10 GPa reduces the maximum pumping factor from -28 to -12.

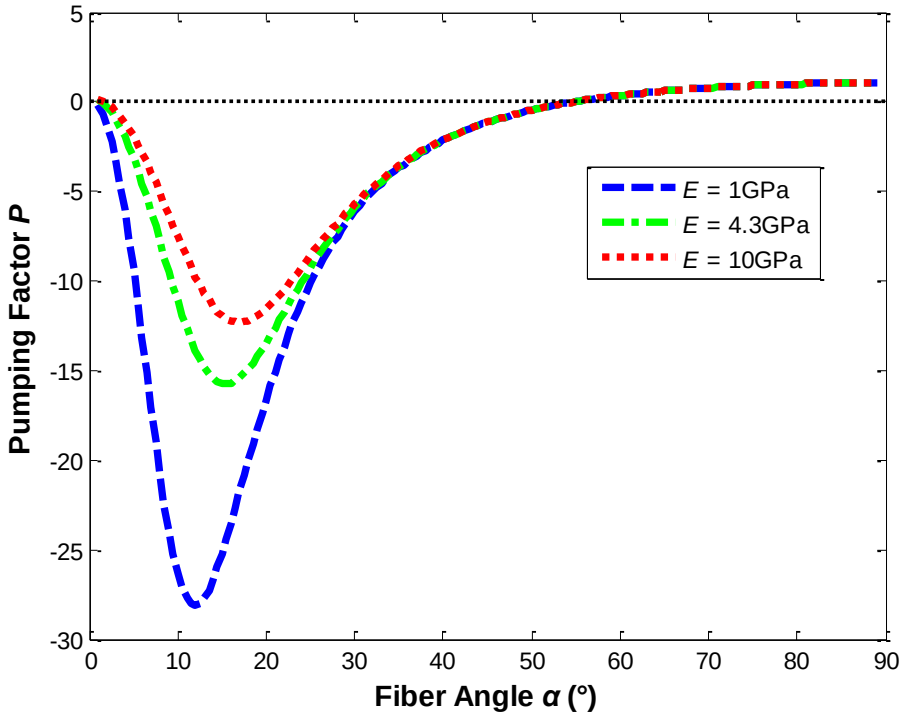

Figure 2-6. Fluid pumping factor of an F^{2}MC tube in epoxy versus fiber angle for several epoxy Young's moduli: E = 1 GPa (dashed), E = 4.3 GPa (dash-dotted), and E = 10 GPa (dotted).

2.2.2 Variable Stiffness

Figure 2-7 shows the closed-open modulus ratio versus fiber angle for F^{2}MC tubes with thicknesses varying from c = 0.1 (thick-walled) to 0.9 (thin-walled). Thin-walled F^{2}MC tubes with small fiber angles have larger modulus ratios. The maximum modulus ratio of 85 in Figure 2-7 is for a thin-walled (c = 0.9) F^{2}MC tube and fiber angle of 30 °.

The fluid pumping factor plotted in Figure 2-8 is for an F^{2}MC tube with an outer epoxy layer that reduces the modulus ratio. The epoxy layer confines the ability of the F^{2}MC tube to change volume and compress the contained fluid. In addition, the epoxy in the F^{2}MC structure is very stiff, increasing the denominator in the modulus ratio. For each F^{2}MC thickness there is an

optimal fiber angle that maximizes the modulus ratio. Unlike the pumping factor, there is a wall thickness that maximizes modulus ratio. In Figure 2-8, $c = 0.7$ shows the maximum modulus ratio.

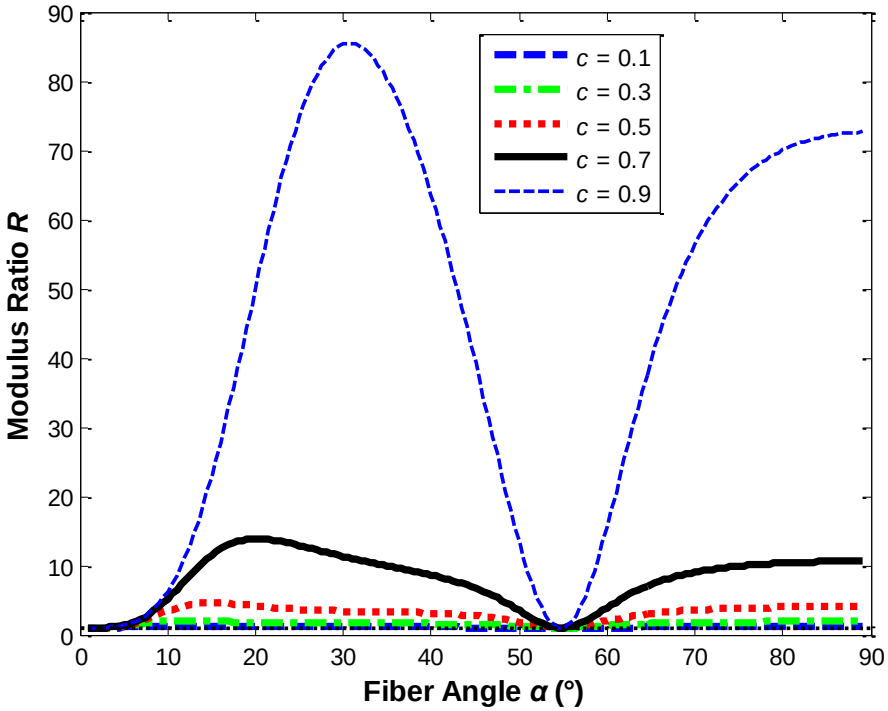

Figure 2-7. Modulus ratio of an F^2MC tube versus fiber angle for several wall thicknesses: c = 0.1 (dashed), c = 0.3 (dash-dotted), c = 0.5 (dotted), c = 0.7 (solid), and c = 0.9 (small dashed).

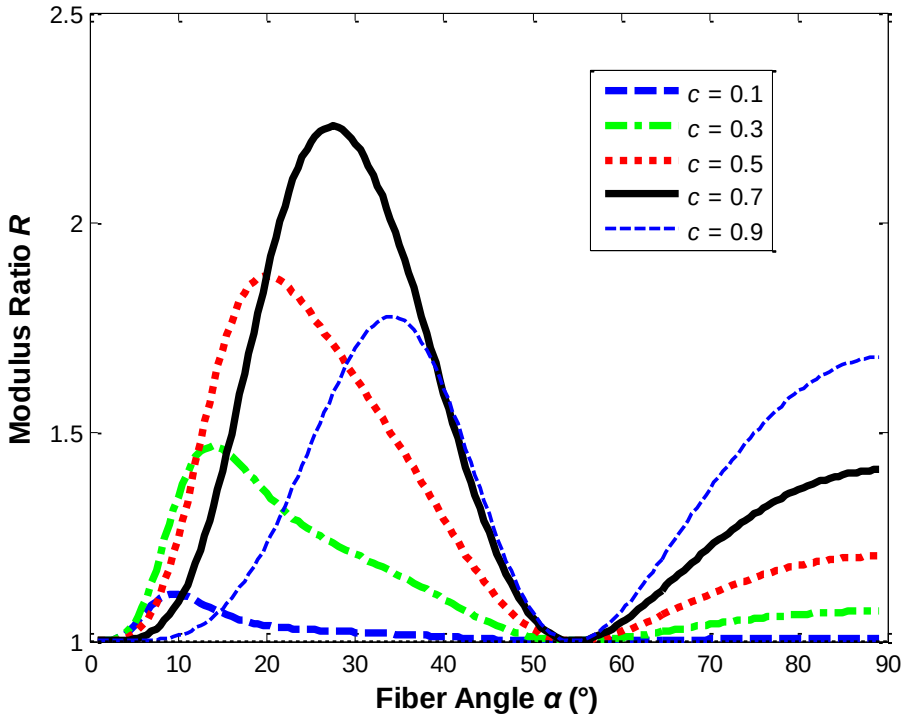

Figure 2-8. Modulus ratio of an F^{2}MC tube in epoxy versus fiber angle for several wall thicknesses: c = 0.1 (dashed), c = 0.3 (dash-dotted), c = 0.5 (dotted), c = 0.7 (solid), and c = 0.9 (small dashed).

Maximizing the modulus ratio of an F^{2}MC structure involves balancing the volume fraction and modulus ratio of the F^{2}MC tube. Large modulus ratio of the F^{2}MC tube requires a thin wall as seen in Figure 2-7. Large volume fraction of the F^{2}MC tube requires a thick wall so that the epoxy does not dominate the structural behavior. In Figure 2-8, a maximal modulus ratio of 2.2 is achieved for the F^{2}MC structure with a relatively thick F^{2}MC wall (c = 0.7) and fiber angle of 27.5 °. Although the modulus ratio of the F^{2}MC structure is only 2.6% of the F^{2}MC tube alone, the open valve stiffness of the F^{2}MC structure is much higher than the open valve stiffness of the F^{2}MC tube.

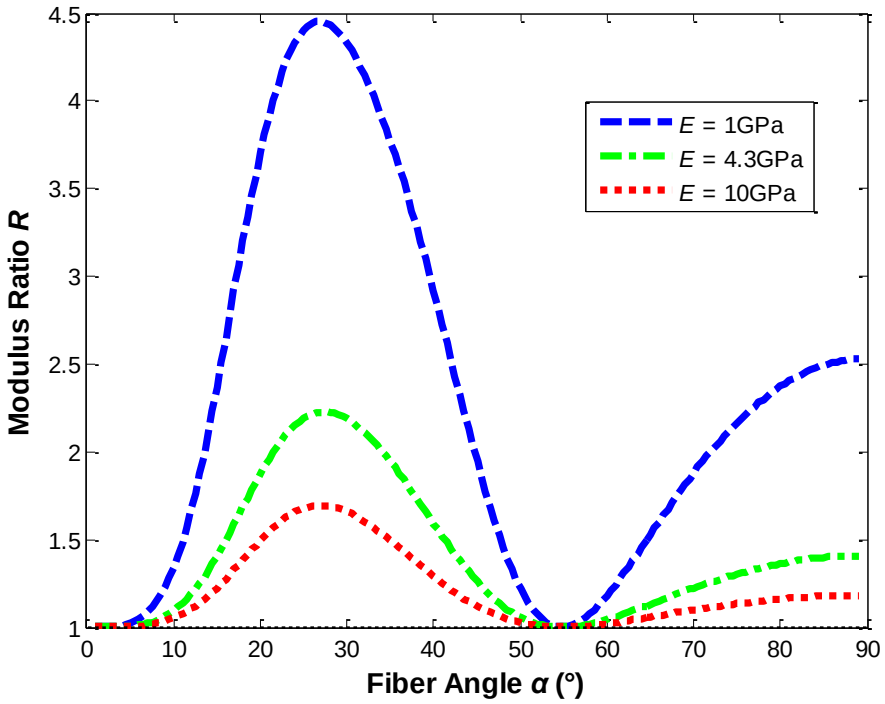

Figure 2-9. Modulus ratio of an F^{2}MC tube in epoxy versus fiber angle for several epoxy Young's moduli: E = 1 GPa (dashed), E = 4.3 GPa (dash-dotted), and E = 10 GPa (dotted).

As with the pumping ratio, thicker and stiffer epoxies produce F^{2}MC structures with smaller modulus ratios. In Figure 2-9, for example, higher stiffness epoxy has smaller modulus ratio. The shape of the curve does not change significantly, however, with changing E.

Chapter 3

Actuation of Fluidic Flexible Matrix Composites in Structural Media

The behavior of isolated F^2MC tubes or tubes incorporated in a rubbery matrix was studied in the previous research. Structural applications often require stiff and strong composites. Therefore, this investigation addresses the actuation performance of F^2MC tubes embedded in structural media. This research is an evaluation of the effectiveness of embedding F^2MC tubes in panel structures. The goal of the work is to tailor the F^2MC tubes to achieve maximal actuation capability in structural media (*e.g.* neat epoxy or fiber reinforced composites).

First, a 3D unit cell model composed of a fluid-filled inner FMC laminate and an outer rigid layer (epoxy or fiber reinforced composite) is developed. A cylindrical geometry is assumed for the unit cell so Lekhnitskii's solution for a multilayered anisotropic tube under axial and pressure loading can be used. Second, numerical methods calculate the free strain and blocked force using free and fixed boundary conditions, respectively. Finally, parametric studies are performed to explore the actuation functionality of F^2MC tubes embedded in rigid structures.

3.1 Analytical Model Development

3.1.1 Bi-layer F^2MC Tube Modeling

Figure 3-1(a) shows a composite plate consisting of F^2MC tubes embedded in a relatively rigid structural medium. This F^2MC plate could be used as a stand-alone structural skin or bonded with other layers to make a sandwich panel. Under pressurization, the F^2MC tubes will shrink or expand in the axial and radial directions depending on the fiber angle. The rigid composite constrains the deformation of the F^2MC tubes, potentially reducing the actuation effectiveness.

This study aims to quantify the actuation performance reduction and develop F^{2}MC tube designs that maximize their actuation performance in relatively rigid media.

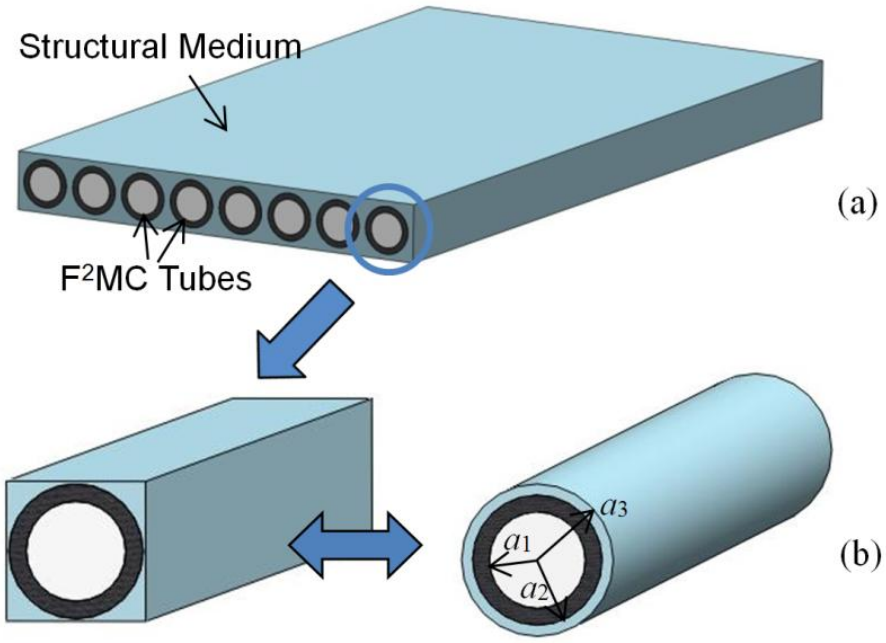

Figure 3-1. (a) F^{2}MC tubes in a composite plate and (b) Unit 3D cell and its equivalent structure

The structural medium is assumed to be either epoxy resin or a relatively rigid FMC, material—both of which utilize a stiff polymer in comparison to the flexible matrix used in the F^{2}MC tubes. It is reasonable to expect that free strain and blocked force performance will decrease with decreasing volume fraction of F^{2}MC tubes in the structural medium. Thus, we assume that the F^{2}MC tubes are arranged side by side in a square array and then embedded in structural media. Therefore, the unit F^{2}MC tube cell of interest with surrounding rigid media has a square cross section as shown in Figure 3-1(b), similar to the way single continuous fibers are modeled in traditional composites. This unit cell is approximated by two concentric homogeneous cylinders, following the Concentric Cylinder Model (CCM) approach (Hashin and Rosen, 1964). The outer radius is calculated to maintain the same area fraction as the square unit cell,

$$\frac{a_3}{a_2} = \sqrt{\frac{4}{\pi}} = 1.13, \tag{3.1}$$

where a_2 is the outer radius of the F^{2}MC tube and a_3 is the outer radius of the structural media layer (see Figure 3-1(b)). Figure 3-1(b) also defines the inner radius a_1 of the F^{2}MC tube.

Internal pressurization of the F^{2}MC tube at pressure p_1 tends to increase the internal volume of the tube. Depending on the fiber angle, the F^{2}MC tube either contracts or elongates if unconstrained. The magnitude of contraction/elongation depends on the lamina properties, lay-up sequence, tube geometry, and actuation pressure. If an internally-pressurized F^{2}MC tube is blocked at the ends, it produces blocked force upon actuation.

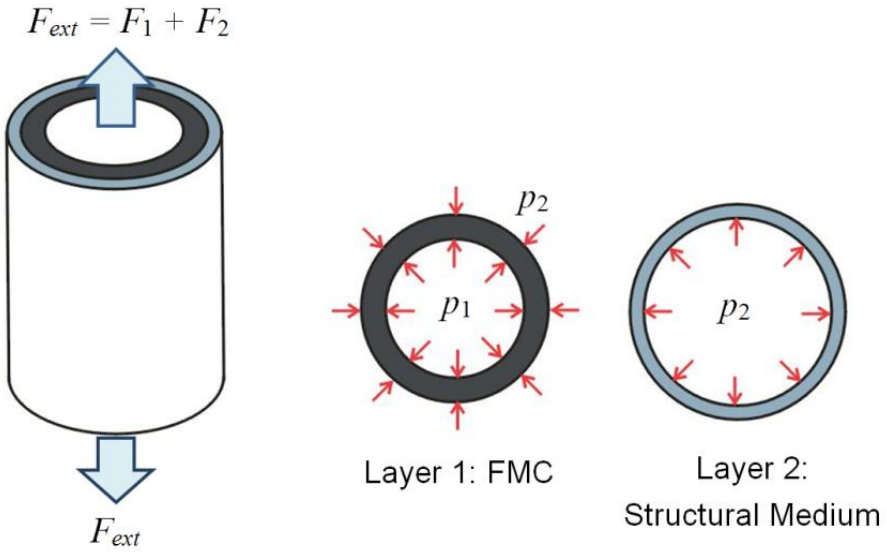

Figure 3-2. External loading on the F^{2}MC structure and individual layers.

Figure 3-2 shows that the axial loading on the unit cell includes forces F_1 and F_2 acting on the inner FMC laminate and outer structural medium, respectively. Axial forces F_1 and F_2 add up to the nominal external axial loading force F_{ext}. In the free strain configuration, F_{ext} simply results from the actuation pressure acting over the area internal to the FMC laminate. In the blocked force case, the difference between F_{ext} and the end force due to internal pressure equals the blocked force. The FMC laminate is assumed to be perfectly bonded to outer rigid matrix, generating contact pressure p_2 when the F^{2}MC tube is pressurized.

3.1.1.1 Inner FMC Laminate

The inner FMC laminate has been modeled by Equations (2.2)-(2.12) in Chapter 2. For simplicity reason, the modeling equations are neglected here.

3.1.1.2 Rigid Outer Layer

The axial force resultant F_2 and contact pressure p_2 act on the layer representing the outer structural medium. If the outer layer is neat epoxy with Young's modulus E and Poisson's ratio v, then the stress distribution is (Boresi and Schmidt, 2003)

$$\sigma_r^{(o)} = \frac{p_2 a_2^2}{a_3^2 - a_2^2} - \frac{a_3^2 a_2^2}{r^2(a_3^2 - a_2^2)} p_2, \tag{3.2}$$

$$\sigma_\theta^{(o)} = \frac{p_2 a_2^2}{a_3^2 - a_2^2} + \frac{a_3^2 a_2^2}{r^2(a_3^2 - a_2^2)} p_2, \tag{3.3}$$

$$\sigma_z^{(o)} = \frac{F_2}{\pi(a_3^2 - a_2^2)}, \tag{3.4}$$

and the strains can be calculated using Hooke's law

$$\varepsilon_r^{(o)} = \frac{1}{E}[\sigma_r^{(o)} - \nu(\sigma_\theta^{(o)} + \sigma_z^{(o)})], \tag{3.5}$$

$$\varepsilon_\theta^{(o)} = \frac{1}{E}[\sigma_\theta^{(o)} - \nu(\sigma_r^{(o)} + \sigma_z^{(o)})], \tag{3.6}$$

$$\varepsilon_z^{(o)} = \frac{1}{E}[\sigma_z^{(o)} - \nu(\sigma_r^{(o)} + \sigma_\theta^{(o)})]. \tag{3.7}$$

If outer layer is fiber reinforced composite, then the stress and strain distributions are calculated using the same equations as for the inner FMC laminate with different material properties. In addition, the loadings F_1 and p_1 are substituted with F_2 and p_2, respectively and p_2 is assigned to be zero in Equations (2.2)-(2.12).

3.1.2 Free Strain Analysis

The boundary conditions for the free strain case are the following:

(1) It is assumed that the bi-layer F^{2}MC structure follows a generalized plane strain solution. Therefore, the axial strain of the inner layer equals that of the outer layer,

$$\varepsilon_z^{(i)} = \varepsilon_z^{(o)}. \tag{3.8}$$

(2) In the radial direction, the assumption of perfect bonding between layers means that the hoop strains at the interface are equal,

$$\varepsilon_\theta^{(i)}|_{r=a_2} = \varepsilon_\theta^{(o)}|_{r=a_2}. \tag{3.9}$$

(3) The actuation force acting on the end area due to internal pressurization equals the sum of the two force resultants for each layer,

$$F_1 + F_2 = p_1 \pi a_1^2. \tag{3.10}$$

The tube is assumed to be long enough that end restraints have a negligible effect on overall deformation (or blocked force) during pressurization. Given the geometry and material properties of the FMC laminate and epoxy layer, the solutions for F_1, F_2 and p_2 can be found using boundary condition Equations (3.8)-(3.10). Then, substitution of F_1 and p_2 back into Equations (2.2)-(2.12) produces the axial strain ε_z of the bi-layer F^{2}MC structure.

3.1.3 Blocked Force Analysis

The boundary conditions for blocked force case are the following:

(1) Both layers of the bi-layer F^{2}MC tube are blocked, so the axial strains in the inner and outer layers are, respectively

$$\varepsilon_z^{(i)} = 0, \tag{3.11}$$

and,

$$\varepsilon_z^{(o)} = 0. \tag{3.12}$$

(2) The perfect bonding assumption yields

$$\varepsilon_\theta^{(i)}|_{r=a_2} = \varepsilon_\theta^{(o)}|_{r=a_2}. \tag{3.13}$$

These three equations, combined with the solution for strain distribution, allow solution for the three unknowns: force resultants F_1 and F_2 and contact pressure p_2. The blocked force is

$$F_b = F_1 + F_2 - p_1 \pi a_1^2. \tag{3.14}$$

The non-dimensional ratio of the block pressure divided by the applied pressure is defined as the block factor, *B*,

$$B = \frac{F_b}{\pi a_3^2 p_1}. \tag{3.15}$$

The block factor measures the pressure amplification of the unit cell.

3.2 Analysis Results

The analysis focuses on the free strain ε_z and block factor *B* of F^{2}MC tubes embedded in rigid epoxy or FMC. The variables of interest include the F^{2}MC wall thickness ratio *c*, outer epoxy layer modulus *E*, fiber angle of outer structural FMC $\alpha^{(o)}$, and fiber angle of inner FMC $\alpha^{(i)}$. The outer layer thickness is assumed to be the minimum value in Equation (3.1). The baseline parameters, representative of typical composite materials are listed in Table 3-1. The FMC lamina properties are referred to this experimental investigation (Shan, 2006).

Table 3-1. Lamina Properties and Geometry for Bi-layer F^{2}MC Tube

FMC Lamina Property	**(Inner)**	**(Outer)**	**Epoxy Property (Outer Layer)**		**Geometry**	
E_1 (GPa)	115	115	E (GPa)	4.3	a_1(mm)	0.7 a_2
E_2 (MPa)	18	171	ν	0.35	a_2(mm)	(0→∞)
ν_{12}	0.33	0.33	**Others**		a_3(mm)	1.13 a_2
ν_{23}	0.93	0.93	$\alpha^{(o)}$ (°)	55	$\alpha^{(i)}$ (°)	(0→90)
G_{12} (MPa)	14.4	136.8	p_1 (MPa)	1		

3.2.1 Free Strain

3.2.1.1 Single F²MC Tube

Figure 3-3 shows the free strains for a single F²MC tube. The fiber angle varies from 0 ° to 90 ° and curves for different F²MC thickness ratios *c* are shown ranging from 0.5 (thick wall) to 0.95 (thin wall). Internal pressurization of 1 MPa is applied. The curves show the well-known contraction (negative strain) for fiber angles less than 55 ° and extension (positive strain) for fiber angles greater than 55 °.

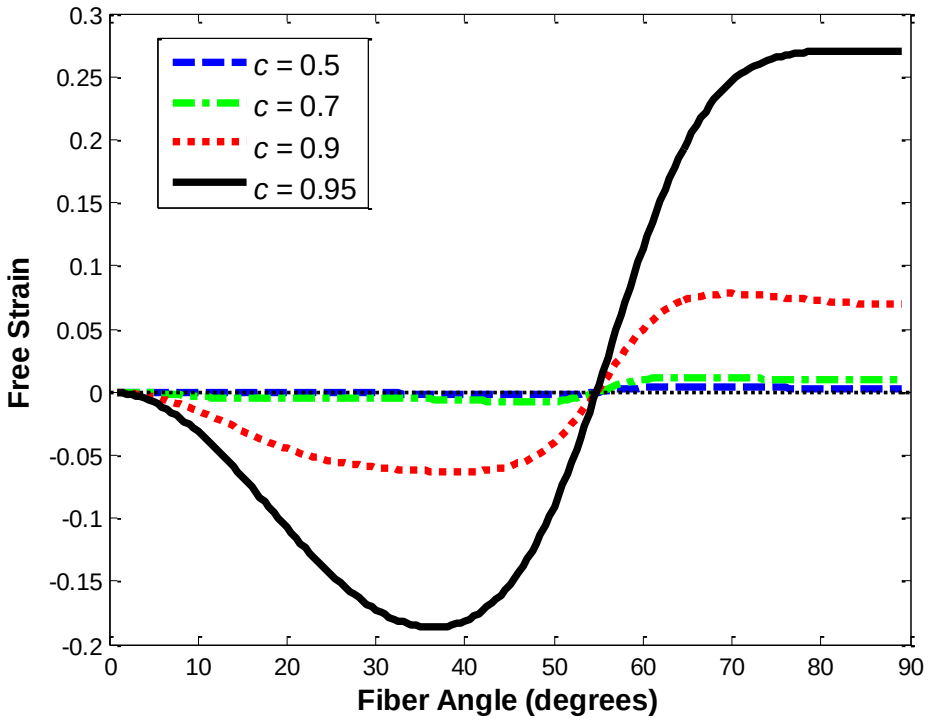

Figure 3-3. Free strain ε_z versus fiber angle $\alpha^{(i)}$ for a single F²MC tube with varied thickness ratios: c = 0.5 (dashed), c = 0.7 (dash-dotted), c = 0.9 (dotted), and c = 0.95 (solid).

Figure 3-3 shows that free strain increases with increasing *c* (or decreasing wall thickness). An F²MC tube with a thinner wall generates larger contraction strain for fiber angles less than 55 °

and larger extension strain for fiber angles greater than 55°. The stiff fibers kinematically link radius change with extension and it is easier to radially and longitudinally strain thin-walled FMC laminates versus thick-walled for the same (1 MPa) applied pressure. The highest free contraction strain of 18.6% is achieved at fiber angle of 36° for a thin-walled (c = 0.95) F^{2}MC tube. The highest free extension strain of 27% is achieved at 82° for a thin walled (c = 0.95) F^{2}MC tube.

3.2.1.2 F^{2}MC Tube in Epoxy

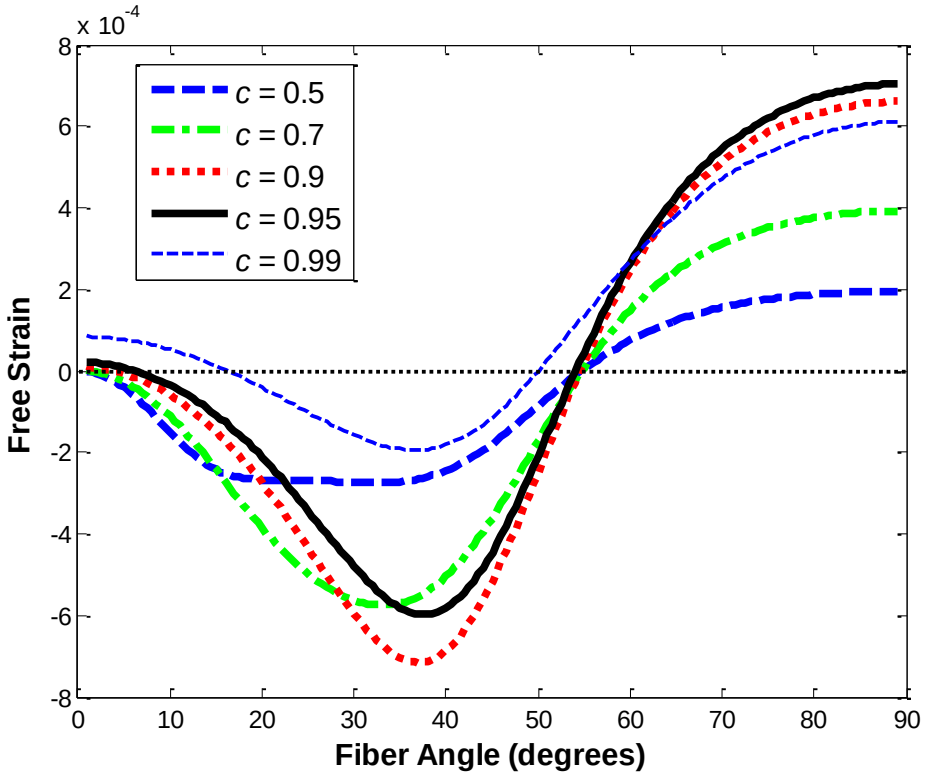

Figure 3-4. Free strain ε_z versus fiber angle $\alpha^{(i)}$ for an F^{2}MC tube in epoxy with varied thickness ratios: c = 0.5 (dashed), c = 0.7 (dash-dotted), c = 0.9 (dotted), c = 0.95 (solid), and c = 0.99 (small dashed).

Figure 3-4 shows the free strain for an F^{2}MC tube embedded in an outer epoxy layer. Fiber angle and wall thickness are again varied. Unlike an isolated F^{2}MC that produces maximum

actuation with a thin wall, an F^2MC tube in epoxy produces maximum actuation at an optimal thickness. With a fiber angle of $37°$ and thickness ratio of 0.9 for the inner FMC laminate, a maximum contraction strain of 0.072% is achieved for the bi-layer F^2MC structure. This is a huge reduction compared to the single F^2MC tube. The stiff epoxy layer radially confines and longitudinally constrains the overall contraction strain of the bi-layer structure. A relatively thick-walled F^2MC tube is optimal in this case for two reasons. First, the thick wall provides radial compliance that assists the contraction performance. Second, a thick wall increases the "active" volume fraction relative to the passive epoxy and thereby increases actuation. If the wall becomes too thick, however, the performance of the inner F^2MC tube begins to decrease and the overall bi-layer performance as well. A fiber angle of $89.5°$ with a thickness ratio of 0.95 yields the maximum extension strain of 0.07% for bi-layer F^2MC structures.

3.2.1.3 FEA Validation for F²MC in Epoxy

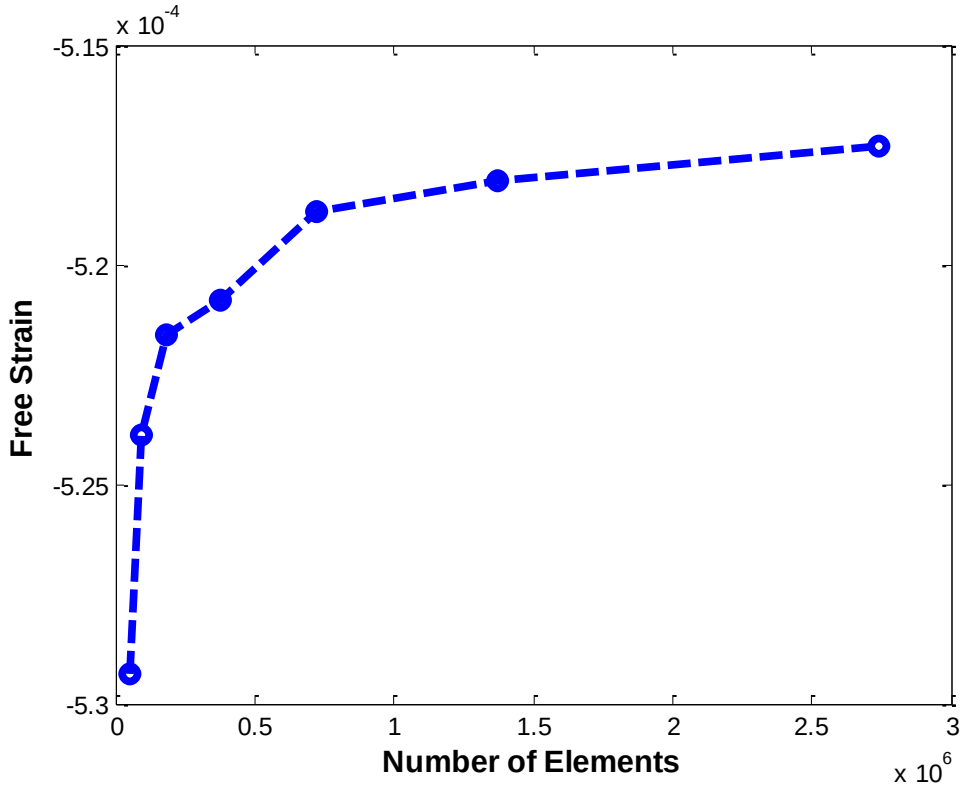

Figure 3-5. Free strain convergence for the ABAQUS prototype

In order to validate the model, the analytical results are compared with those acquired through finite element analysis (FEA) in ABAQUS. A prototype with the baseline parameters (a_1 = 10 mm, a_2 = 15 mm, a_3 = 17 mm, and L = 1000 mm) and loading is built in ABAQUS to simulate an F²MC tube embedded in neat epoxy. The length is much greater than the radius so that the prototype satisfies the "infinitely long" assumption in the analytical model. The direct linear equation solver and hexahedron elements are used. Axial strain and radial, hoop, and axial stress distributions are examined at the mid-length of the prototype, far from the non-uniform regions at the ends. Figure 3-5 shows the ABAQUS free strain converging with increasing

number of elements, motivating the selection of 2740749 elements for the prototype. Figure 3-6 shows the analytical and ABAQUS free strain matching to within 0.5%.

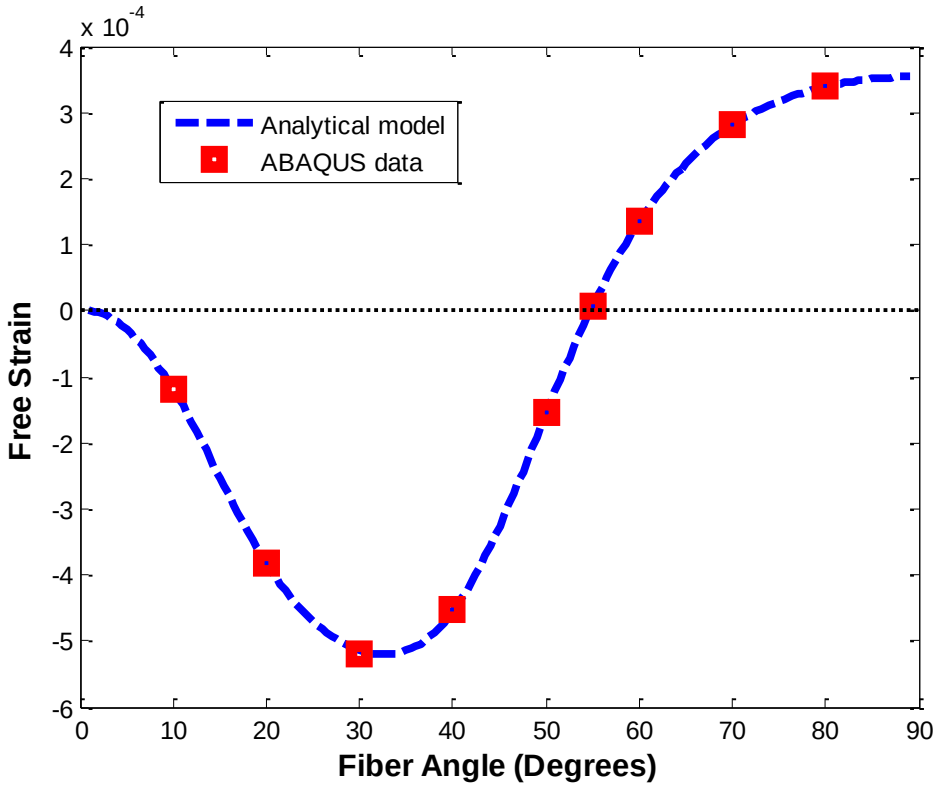

Figure 3-6. Free strain ε_z versus fiber angle $\alpha^{(i)}$ for an F^{2}MC tube in epoxy with c = 0.7 in the analytical model and the ABAQUS simulation.

Figure 3-7 compares the analytical and ABAQUS stress distributions for $\alpha^{(i)} = 30\,°$ from the inner radius of 10 mm to the outer radius of 17 mm. The interface between the F^{2}MC tube and epoxy is at 15 mm. All three stresses match well with departures only occurring on the inner surface and at the interface where FEA has a notoriously difficult time converging.

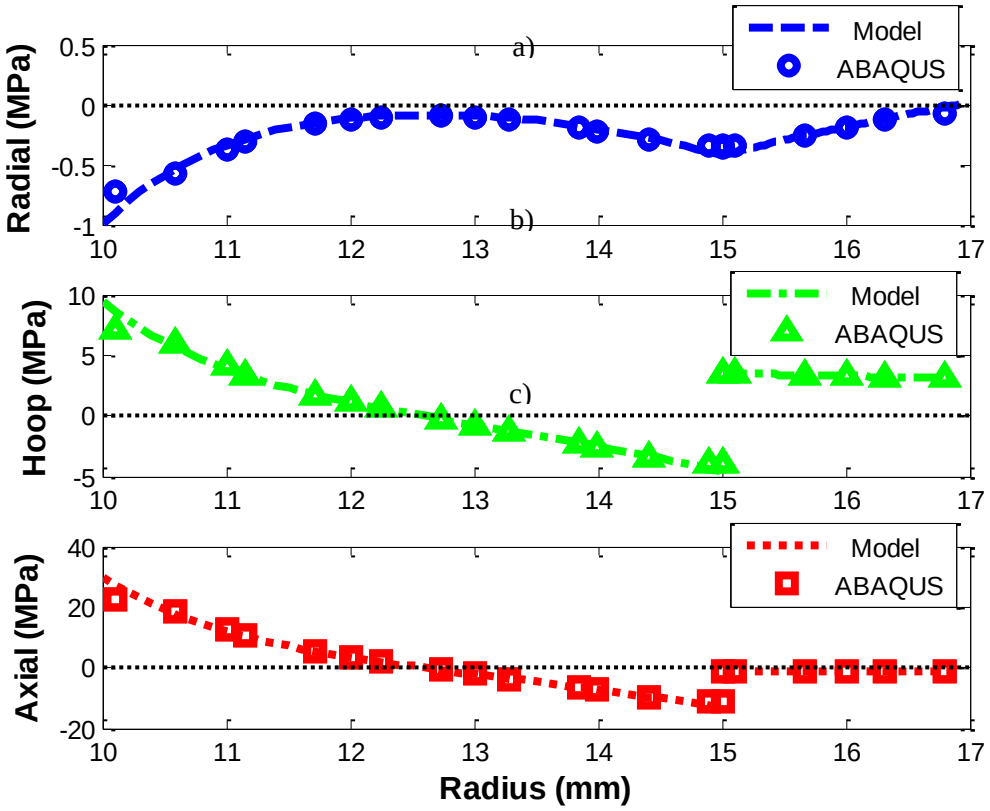

Figure 3-7. Stress distributions through thickness of an F[2]MC tube embedded in epoxy: (a) Radial stress σ_r, (b) Hoop stress σ_θ, and (c) Axial stress σ_z.

3.2.1.4 Effect of Epoxy Modulus

Figure 3-8 shows the maximum contraction and extension strain achievable with an F[2]MC tube embedded in epoxy. The epoxy modulus varies from 0.1 to 10 GPa and the fiber angle and thickness are optimized to provide maximum contraction and extension. As expected, the strain greatly reduces with increasing epoxy modulus. In Figure 3-9, the optimal thickness ratio is plotted over the same range of epoxy modulus. As the epoxy modulus increases, the tube wall thickness also increases, leading to a reduction in the thickness ratio. The contractor tubes need a thicker wall because their diameters change greatly under pressurization and the thick wall helps accommodate this radial strain. For extender tubes, the hoop strain is smaller and thicker walls

reduce the pressurized area at the end of the tube that aids extension. Thus, the optimal wall thickness for extender tubes does not change much with epoxy stiffness.

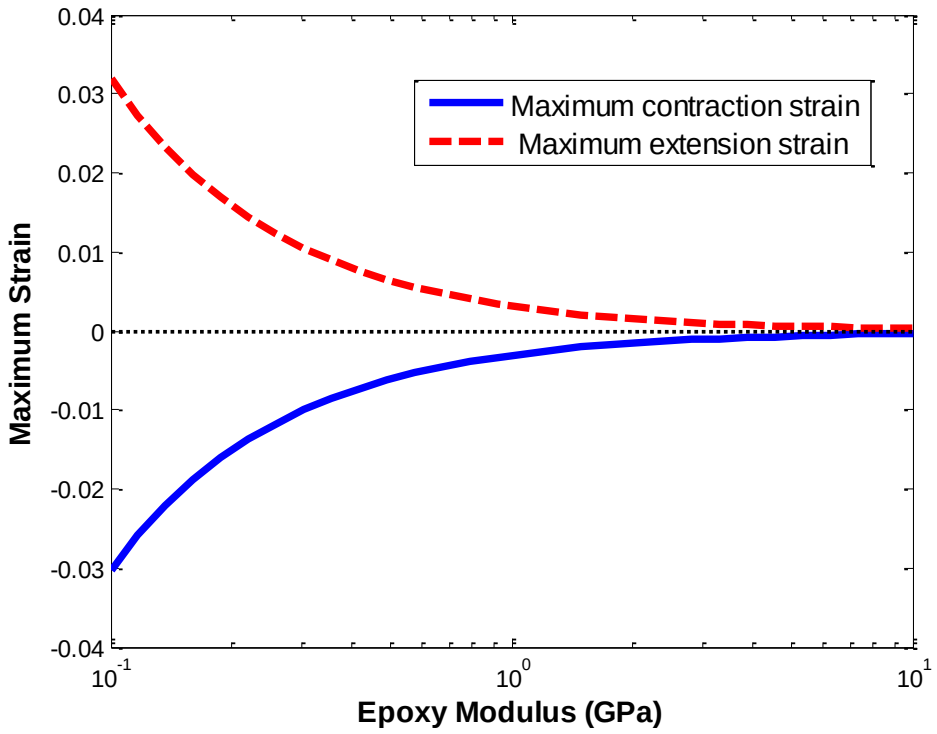

Figure 3-8. Maximum contraction/extension strain versus epoxy modulus E for an F^{2}MC tube in epoxy with optimized thickness ratio c (shown in Figure 3-9)

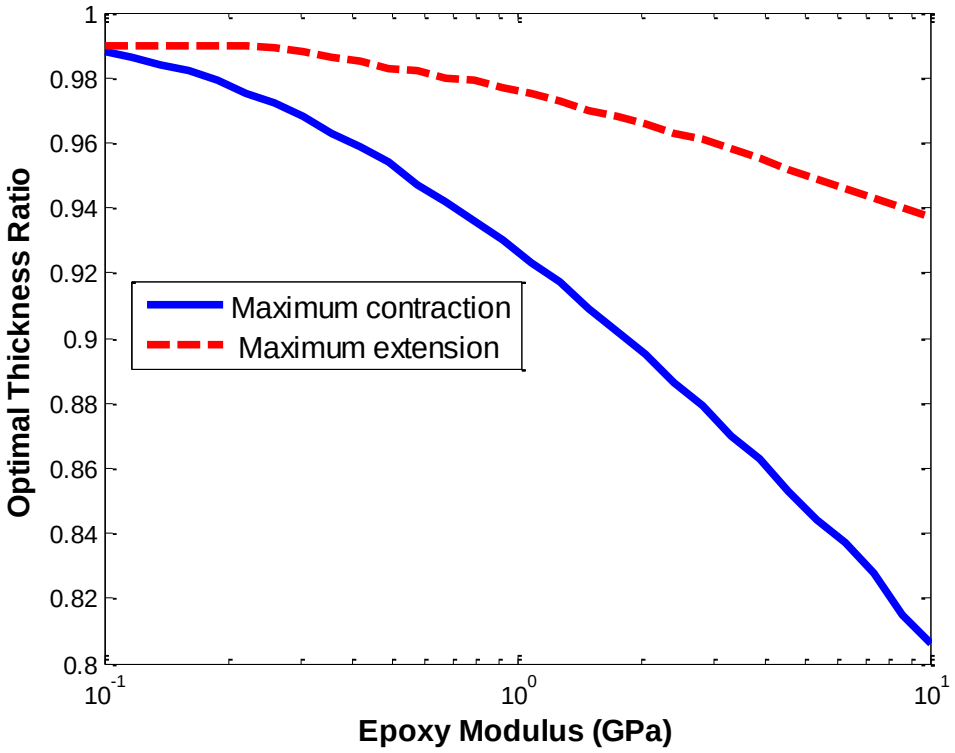

Figure 3-9. Optimal thickness ratio for maximal contraction/extension performance versus epoxy modulus E for an F^{2}MC tube in epoxy.

3.2.1.5 F^{2}MC Tube in FMC

For the F^{2}MC tube embedded in FMC, Table 3-1 shows that the matrix used for the outer FMC composite is ten times stiffer than that of the inner F^{2}MC tube. Thus, the outer FMC can be considered a "rigid" composite. The fiber angle of the outer composite $\alpha^{(o)}$ is also assumed to be a structurally strong 55 °, a fiber angle that should result in an outer FMC that neither contracts nor extends under pressurization. The effective elastic constants of this 55 ° outer FMC in a cylindrical coordinate system are listed in Table 3-2.

Table 3-2. Effective Elastic Constants of Outer 55 °FMC Composite

Elastic Constants			
E_r (GPa)	0.66	$\nu_{z\theta}$	0.49
E_θ (GPa)	1.28	$G_{\theta r}$ (MPa)	81.1
E_z (GPa)	0.31	G_{zr} (MPa)	57.0
$\nu_{\theta r}$	-0.93	$G_{z\theta}$ (GPa)	25.4
ν_{zr}	0.48		

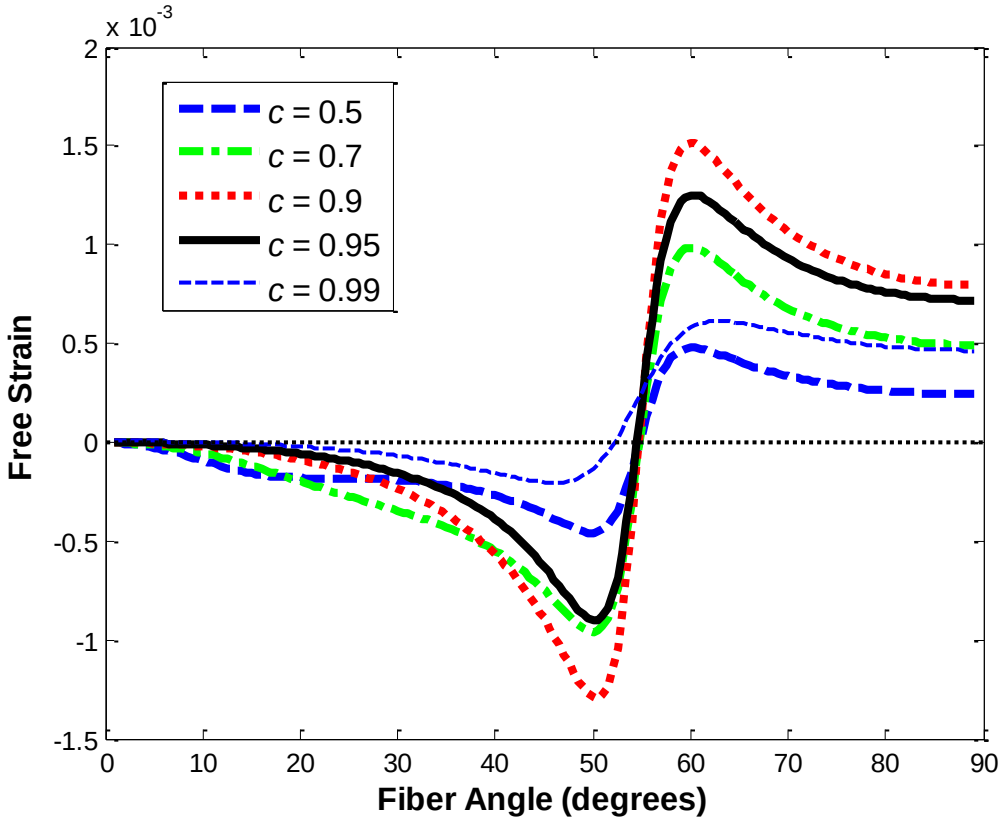

Figure 3-10. Free strain ε_z versus fiber angle $\alpha^{(i)}$ for an F^{2}MC tube in FMC with varied thickness ratio: c = 0.5 (dashed), c = 0.7 (dash-dotted), c = 0.9 (dotted), c = 0.95 (solid), and c = 0.99 (small dashed).

Figure 3-10 shows the free strain of the F^{2}MC tube in FMC, where the fiber angle of inner FMC $\alpha^{(i)}$ varies from 0 ° to 90 ° and thickness ratio c varies from 0.5 to 0.99. Similar to F^{2}MC in epoxy, the maximum contraction and extension performance occur at optimized thickness ratios. The maximal contraction strain of 0.13% and maximal extension strain of 0.15% are achieved

with a thickness ratio of 0.9 at fiber angles of 50 ° and 60 °, respectively. The magnitudes of contraction and extension strain are larger in comparison to those for F^{2}MC in epoxy because the outer 55 ° FMC layer has a lower modulus than epoxy layer in the radial, hoop and axial directions (see Tables 3-1 and 3-2). Thus, the outer FMC layer is more compliant and less constraining on the inner F^{2}MC tube, leading to higher actuation for the bi-layer structure. The optimal fiber angles at which maximal performance is attained have shifted towards the outer composite fiber angle ($\alpha^{(o)}$ = 55 °). In addition, the peaks are much sharper and narrower, indicating an increased constraint as the fiber angle deviates from that of the outer FMC. This demonstrates the higher performance and tunability of F^{2}MC-FMC bi-layers.

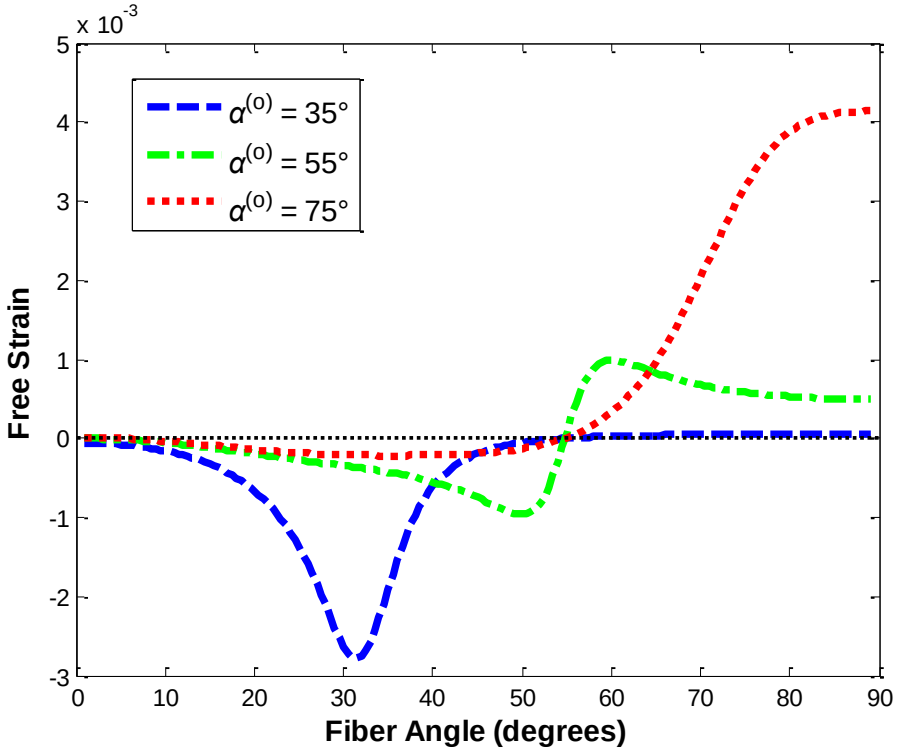

Figure 3-11. Free strain ε_z versus fiber angle $\alpha^{(i)}$ for an F^{2}MC tube in FMC with varied fiber angles: $\alpha^{(o)}$ = 35 °(dashed), $\alpha^{(o)}$ = 55 °(dash-dotted), and$\alpha^{(o)}$ = 75 °(dotted).

In order to further demonstrate the tunability of F^{2}MC-FMC bi-layers, the effects of outer fiber angle on performance are investigated. Figure 3-11 plots the free strain versus fiber angle

for outer composite fiber angles $\alpha^{(o)}$ equal to 35°, 55°, and 75°. The figure shows that a small outer composite fiber angle of 35° results in enhanced contraction performance for the F^{2}MC structure - the maximal contraction strain increases by 192%. The fiber angle of the outer FMC laminate is smaller than 55° so it tends to contract upon pressurization, contributing to the high contraction performance of the bi-layer structure. F^{2}MC tubes with properties that match the surrounding materials are more likely to achieve maximal performance. In this case, for example, an F^{2}MC tube with fiber angle of 32° ($v_{\theta r}$ = 0.57, v_{zr} = -1.45, $v_{z\theta}$ = 2.55) has Poisson's ratios closer to those of the outer 35° FMC layer ($v_{\theta r}$ = 0.48, v_{zr} = -0.93, $v_{z\theta}$ = 2.0) than the 50° F^{2}MC tube ($v_{\theta r}$ = -0.39, v_{zr} = 0.28, $v_{z\theta}$ = 0.70). As a result, the former bi-layer F^{2}MC tube outperforms the latter in terms of actuation capability (see Figure 3-11). Extender F^{2}MC-FMC bi-layer structures can also be tuned. If, for example, the outer composite fiber angle is 75°, the maximum extension strain increases significantly.

3.2.1.6 Experimental Validation for F^{2}MC Tube in FMC

Experimental tests are performed to verify the analytical models for F^{2}MC tube embedded in FMC. There are totally five bi-layer F^{2}MC test cells made for the experiment. The inner layer is made of AS4D carbon fiber and ReoFlex 20 polyurethane resin. The out layer, however, uses AS4D carbon fiber and ReoFlex 60 polyurethane resin, which is a stiffer class of matrix than ReoFlex 20. The outer layer is structurally stronger than the inner and therefore it imposes a constraint on the performance of the inner F^{2}MC tube. The specimens have an inner radius a_1, 10 mm, an intermediate radius a_2, 15 mm, an outer radius a_3, 17.5 mm, and a length L, 270 mm. The stiff FMC layer has a fiber angle of 57°, while the inner fiber angles are 12.5°, 22.5°, 38.3°, 52.5°, and 62.5°, respectively. Table 3-3 shows the elastic properties that are used for the analysis. The

values of E_2 and G_{12} are slightly different from those in Table 3-1 because this part is a follow up research work and the properties have been updated based on experiments (Wimmer *et al.*, 2012).

Table 3-3. Lamina Properties of Bi-layer F^{2}MC Tube in Experiments

Lamina Property	Inner FMC Layer	Outer FMC Layer
E_{11} (GPa)	115	115
E_{22} (MPa)	30	285
v_{12}	0.33	0.33
v_{23}	0.93	0.93
G_{12} (MPa)	25.8	245

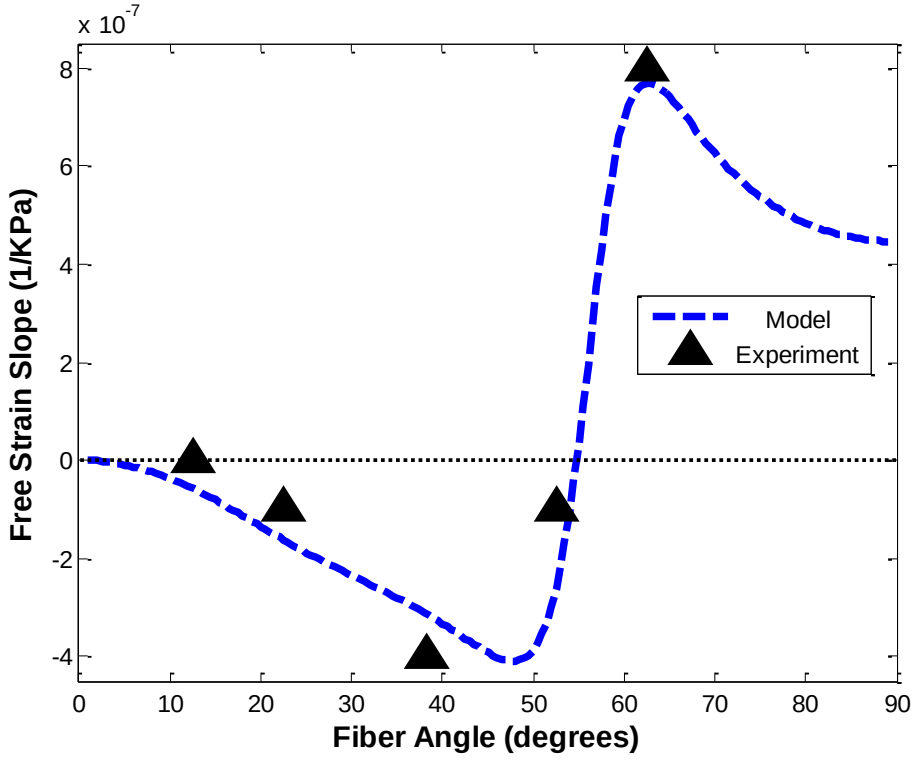

Figure 3-12. A free strain slope comparison of theoretical and experimental results for F^{2}MC tube in FMC

Figure 3-12 shows a free strain slope comparison of analytical and experimental results for F^2MC tube in stiff FMC. The results basically achieve a reasonably good match. The biggest discrepancies occur for F^2MC tubes with relatively small fiber angles (smaller than 25 °). In those cases, the properties of inner and outer layers are very different due to the diverse matrices used as well as the difference in fiber orientation. Therefore, the shear lag and end effects can be significant. However, these phenomena are not taken into account in the analytical models.

In order to justify this explanation, finite element models of the bi-layer specimens are built as shown in Figure 3-13. The FEA model has exactly the same geometry as the specimens. It has a steel plug at the end like the experiments. Due to symmetry only half of the length is modeled. Perfect bonding is applied between the composite layers and between the inner layer and the plug. The loading in the model is the actuation pressure acting on internal surfaces of both the inner layer and the plug. The direct linear equation solver and 143,880 hexahedron elements are used.

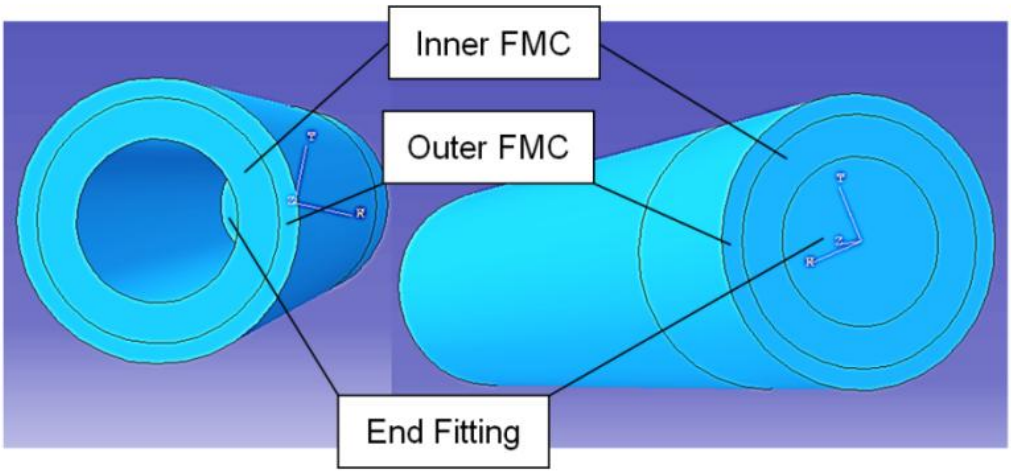

Figure 3-13. Finite element model of a bi-layer specimen

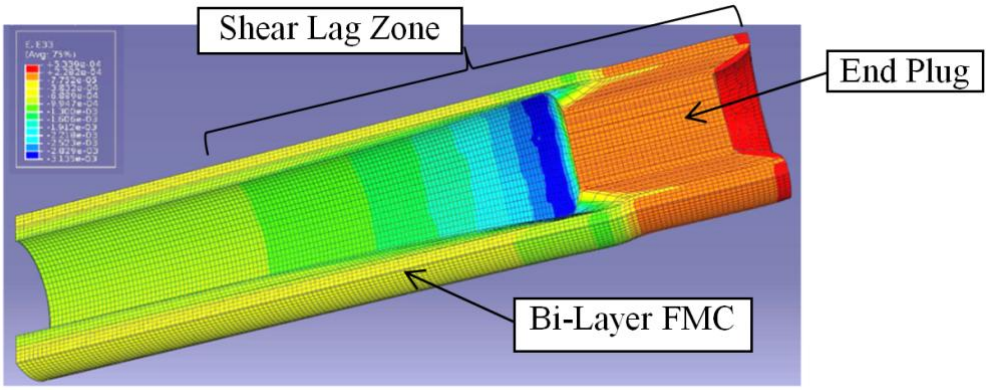

Figure 3-14. Example axial strain distribution from FEA for 38.3 °bi-layer specimen

Figure 3-14 shows an example of the axial strain distribution through the thickness of the bi-layer F^2MC model. At the end of the tube, the strains are non-uniform and a substantial amount of shear lag happens, especially near the end of the F^2MC prototype. Besides shear lag, material nonlinearity and viscoelastic deformation can also contribute to the discrepancies that were found between experimental results and analytical predictions.

3.2.2 Blocked Force

3.2.2.1 Single F²MC Tube

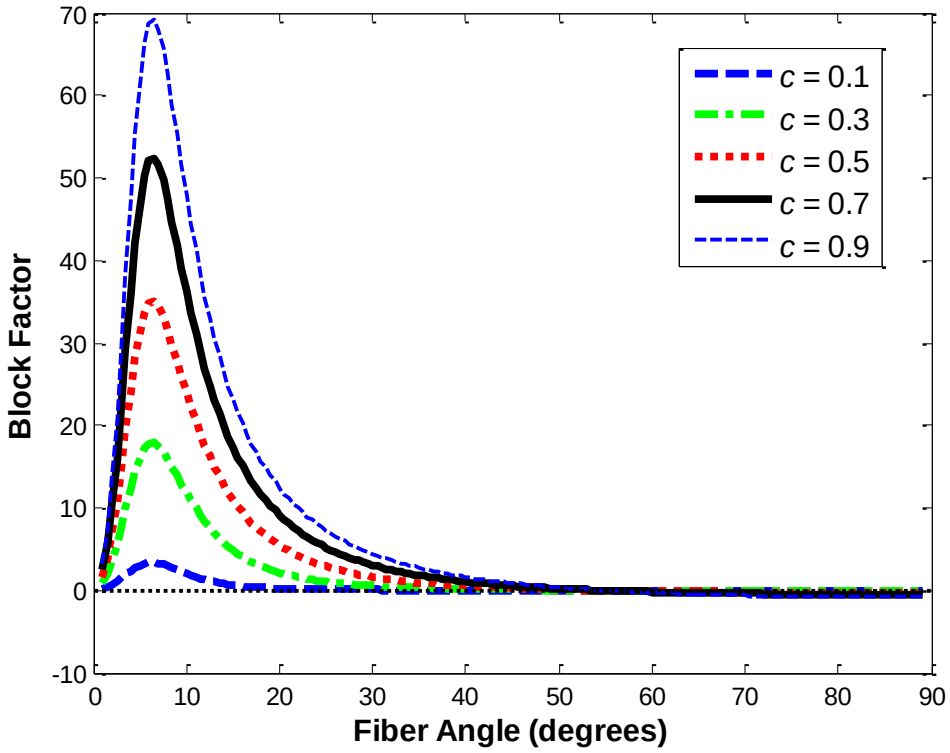

Figure 3-15. Block factor B versus fiber angle $\alpha^{(i)}$ for a single F²MC tube with varied thickness ratios: c = 0.1 (dashed), c = 0.3 (dash-dotted), c = 0.5 (dotted), c = 0.7 (solid), and c = 0.9 (small dashed).

Figure 3-15 illustrates the block factor B versus fiber angle for F²MC tubes with thickness ratios varying from c = 0.1 (thick-walled) to c = 0.9 (thin-walled). Thin-walled F²MC tubes with near-axial fiber orientation have larger block. The maximum block factor of 69 in Figure 3-15 is for a thin-walled F²MC tube and fiber angle of 6.5 °. In this maximum configuration the pressure generated by the F²MC tube is almost 70 times larger than the internal pressurization. For tubes

with wind angles greater than 55°, however, the maximum block factor is around -1 for tubes with large wind angles.

The model is linear and strains are small so the blocked force can be decomposed into two steps. First, the tube is pressurized and allowed to contract/extend. Then an axial force is applied to pull the tube back to its original length. The blocked force is this pulling force, which equals the free displacement times the effective axial stiffness of the F^2MC tube or the free strain times effective modulus times tube length. To achieve high blocked force, there must be high free strain and large effective modulus. High free strain requires a thin FMC wall. Smaller fiber angles lead to higher axial modulus. Thus, maximum blocked force is achieved for F^2MC tubes with thin walls and near-axial fiber orientation. F^2MC tubes with large fiber angles (*i.e.* greater than 55°) only generate a limited amount of blocked force because the effective axial modulus of the tube is low.

3.2.2.2 F^2MC Tube in Epoxy

Figure 3-16 plots the block factor for an F^2MC tube with an outer epoxy layer. The epoxy layer confines the ability of the F^2MC tube to contract and expand in both radial and longitudinal directions. Similar to the free strain case, bi-layer F^2MC tubes have specific wall thicknesses and wind angles that produce maximal performance. The inner FMC tube should have a small wall thickness to produce high blocked force. On the other hand, the inner FMC laminate should compose a significant volume fraction of the overall structure to avoid domination by the confining epoxy layer. The optimal *c* shown in Figure 3-16 balances these effects, producing a maximal contractile block factor of 7.5 at a fiber angle of 11.5° and thickness ratio of 0.5. This is a significant reduction in block factor from the single F^2MC result. The optimal extensile block

factor of 0.67 occurs at a fiber angle of 89.5 ° and thickness ratio of 0.9, relatively close to the single F^{2}MC value.

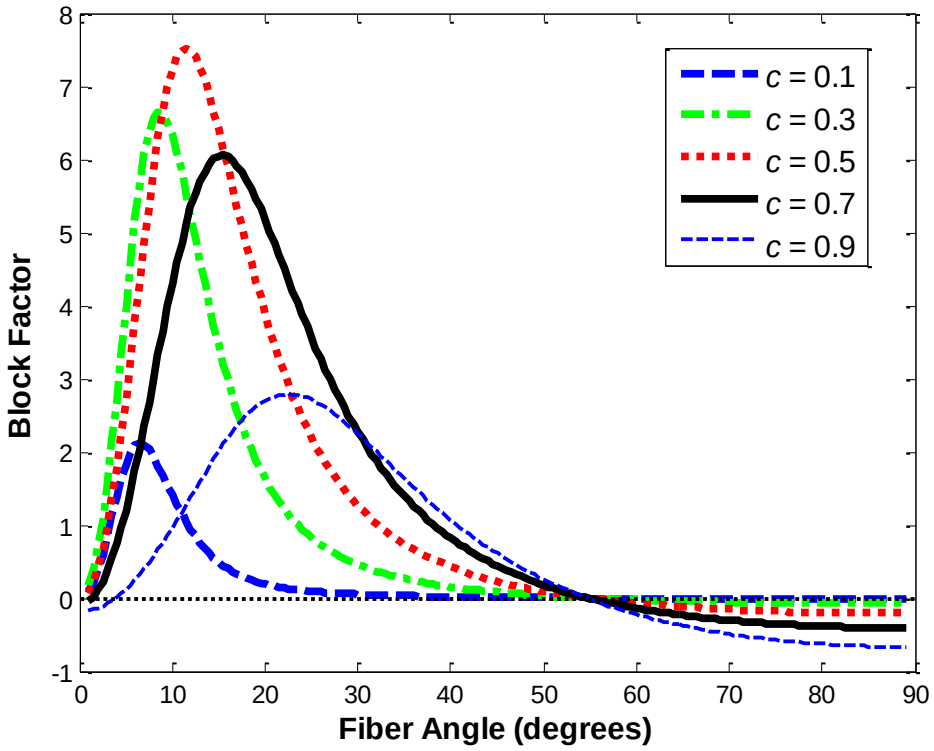

Figure 3-16. Block factor B versus fiber angle $\alpha^{(i)}$ for an F^{2}MC tube in epoxy with varied thickness ratios: c = 0.1 (dashed), c = 0.3 (dash-dotted), c = 0.5 (dotted), c = 0.7 (solid), and c = 0.9 (small dashed).

Figure 3-16 also shows significant movement in the optimal fiber angle for maximal contractile blocking force. The optimal fiber angle shifts rightward as wall thickness decreases, increasing the contraction ability of the F^{2}MC tube as its volume fraction decreases. The optimal extensile blocking force occurs at near the circumferential fiber wind angle regardless of wall thickness.

3.2.2.3 Effect of Epoxy Modulus

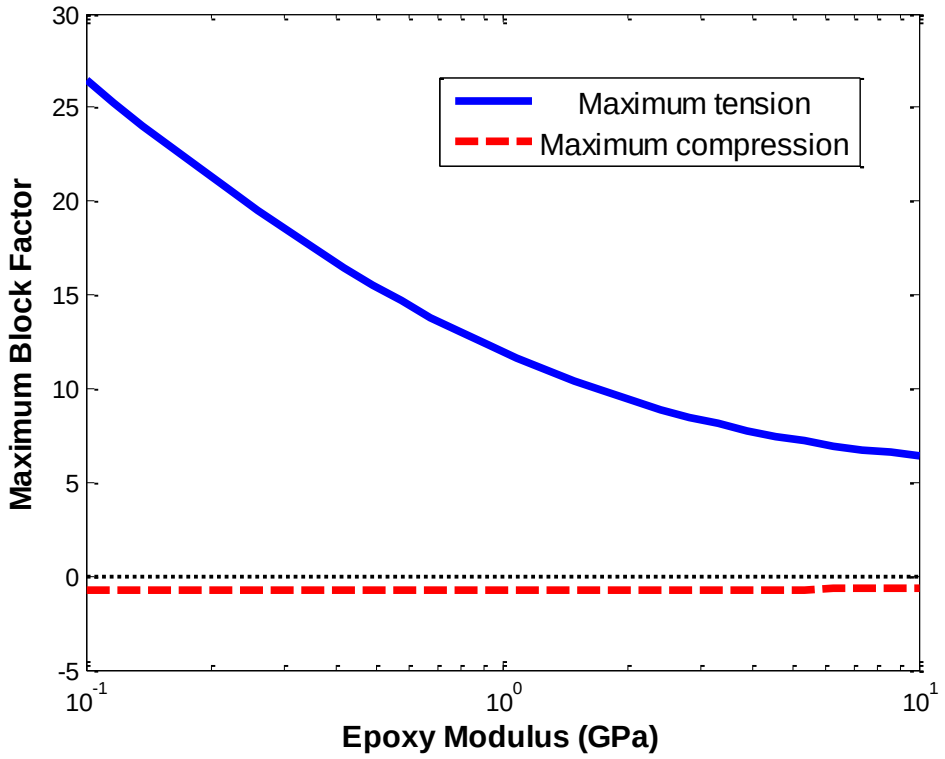

Figure 3-17. Maximum block factor versus epoxy modulus *E* for an F^{2}MC tube in epoxy with optimized thickness ratio *c* (referring to Figure 3-18)

Figures 3-17 and 3-18 show the effect of epoxy modulus on the maximum block factor and optimal wall thickness, respectively. As with the free strain case, stiffer epoxies produce optimized F^{2}MC structures with smaller block factors and thicker walls. As the epoxy modulus varies from 0.1 GPa to 10 GPa, the maximum block factor for contractor tubes reduces from 26.5 to 6.4. The corresponding thickness ratio curve reveals a decreasing trend, dropping drops from 0.7 to 0.43. The reduction in block factor is not as substantial as the reduction in free strain because the load is being carried by the relatively stiff fibers. On the other hand, the optimal block factor is almost constant near -1. Contractor tubes outperform extender tubes because

extender tubes possess low effective axial modulus due to the circumferential fiber orientation and are more easily blocked.

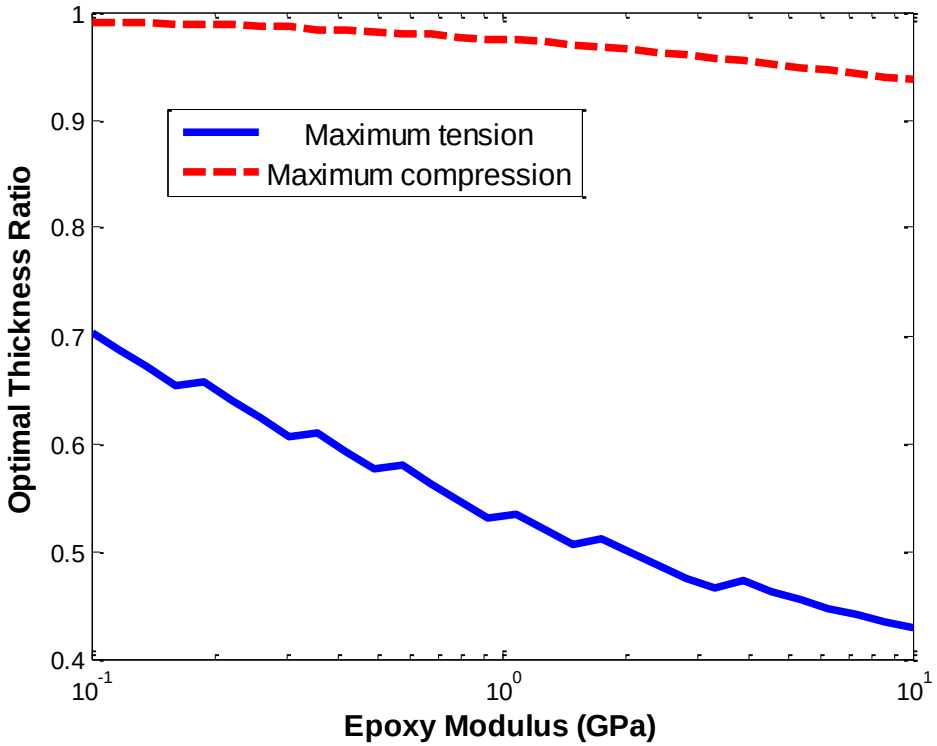

Figure 3-18. Optimal thickness ratio for maximum blocked configuration versus epoxy modulus E for an F^2MC tube in epoxy.

3.2.2.4 F²MC Tube in FMC

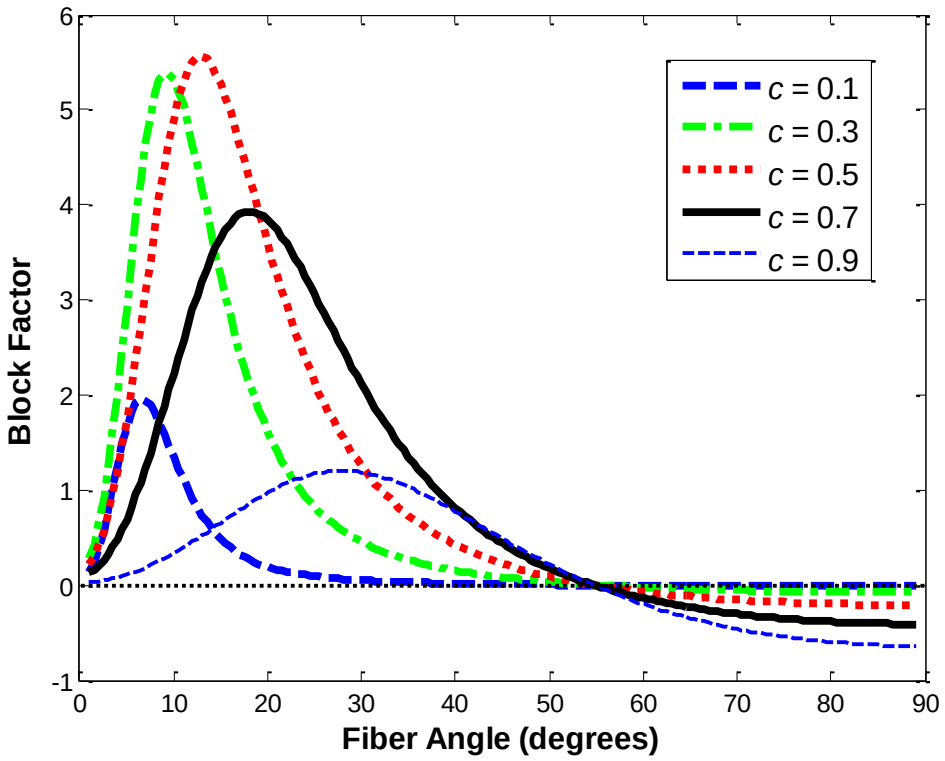

Figure 3-19. Block factor B versus fiber angle $\alpha^{(i)}$ for an F²MC tube in FMC with varied thickness ratios: c = 0.1 (dashed), c = 0.3 (dash-dotted), c = 0.5 (dotted), c = 0.7 (solid), and c = 0.9 (small dashed).

The block factor for F²MC tubes in FMC composite with fiber angle of 55 ° (see Figure 3-19) shows similar trends as with the epoxy outer layer. The extensile results, for example, are almost identical. The optimal fiber angles shift to the right with decreasing thickness. Figure 3-19 shows that the maximum contracting block factor is slightly smaller, however, at 5.56 for a fiber angle of 13 ° and thickness ratio of 0.5.

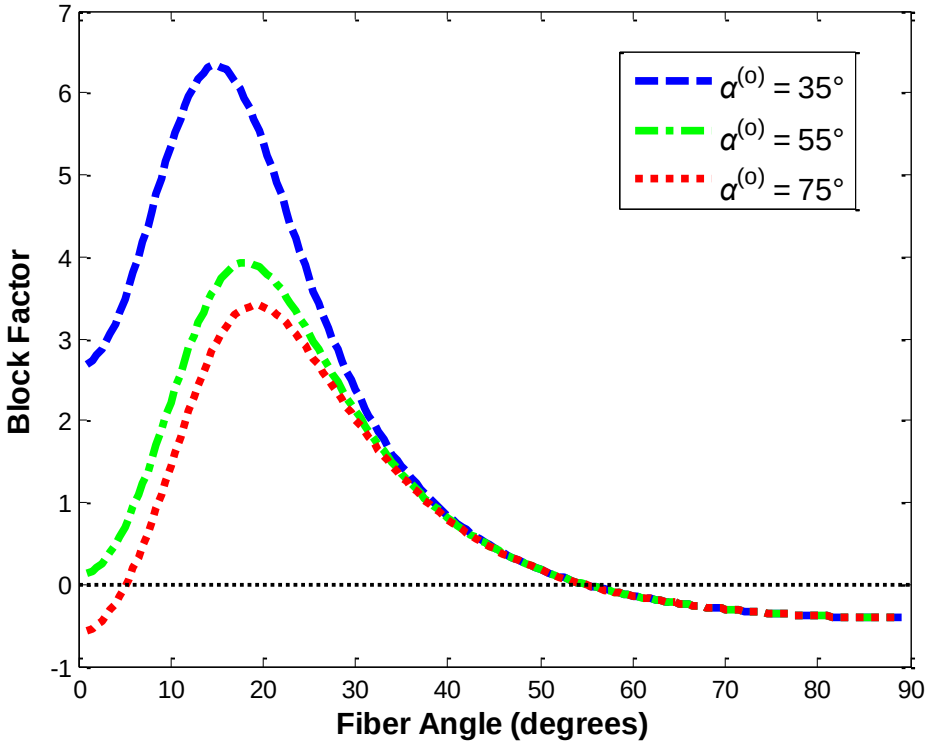

Figure 3-20. Block factor B versus fiber angle $\alpha^{(i)}$ for an F^{2}MC tube in FMC with varied fiber angles: $\alpha^{(o)}$ = 35 °(dashed), $\alpha^{(o)}$ = 55 °(dash-dotted), and$\alpha^{(o)}$ = 75 °(dotted).

Varying the fiber angle of the outer FMC layer greatly influences the blocked force performance of the F^{2}MC structure. Figure 3-20, for example, illustrates that 35 ° outer FMC results in higher block factor than 55 ° or 75 ° composites. The outer layer also contributes to blocked force due to its contractile nature. This has little impact on the extensile performance, however.

Chapter 4

Fluidic Flexible Matrix Composite Damping Treatment for a Cantilever Beam

In this work, we expand the potential applications of F^2MC tubes by studying the concept of bonding a fluidic-circuit-equipped F^2MC patch to a cantilever beam to increase vibration damping. Figure 4-1 shows example applications of F^2MC damping treatment patches that can be easily integrated into beam structures. These patches have multiple F^2MC tubes placed in parallel, built-in fluidic circuits, and mounting points at the ends to fix them to cantilevered structures such as aircraft wings, helicopter tailbooms, etc. to reduce their vibrations.

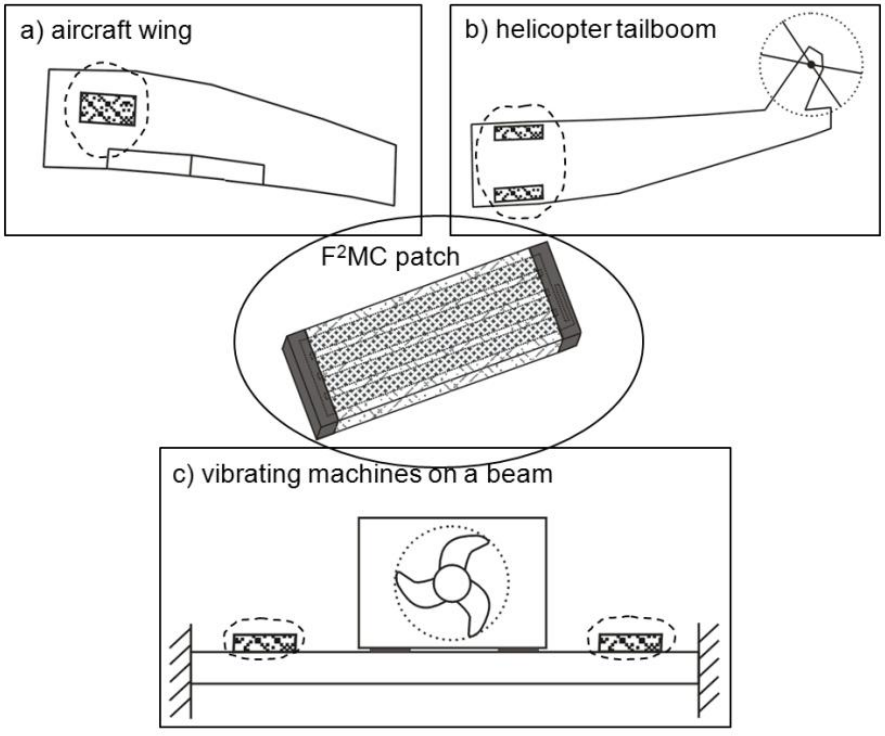

Figure 4-1. Self-contained multi-F^2MC patch for vibration damping on a) an aircraft wing; b) a helicopter tailboom; and c) a beam structure.

In this chapter, we model, analyze, design, and experimentally test a multi-F^{2}MC damping treatment on a cantilever beam as shown in Figure 4-2. The F^{2}MC patch is bonded at two rigid connection points to a cantilever beam with length, L, width, b, and height, h. A tip force $F(t)$ causes transverse vibration $w(x,t)$ and stretches the F^{2}MC patch. This deformation of the F^{2}MC patch changes the interior volume of the tubes and pumps fluid into an accumulator through an orifice, dissipating mechanical energy. The objective of this investigation is to design the F^{2}MC patch and fluidic circuit to suppress the transverse beam vibration as measured by the damping ratios in the frequency response functions (FRF). The model predicted performance is validated with a bench-scale experiment.

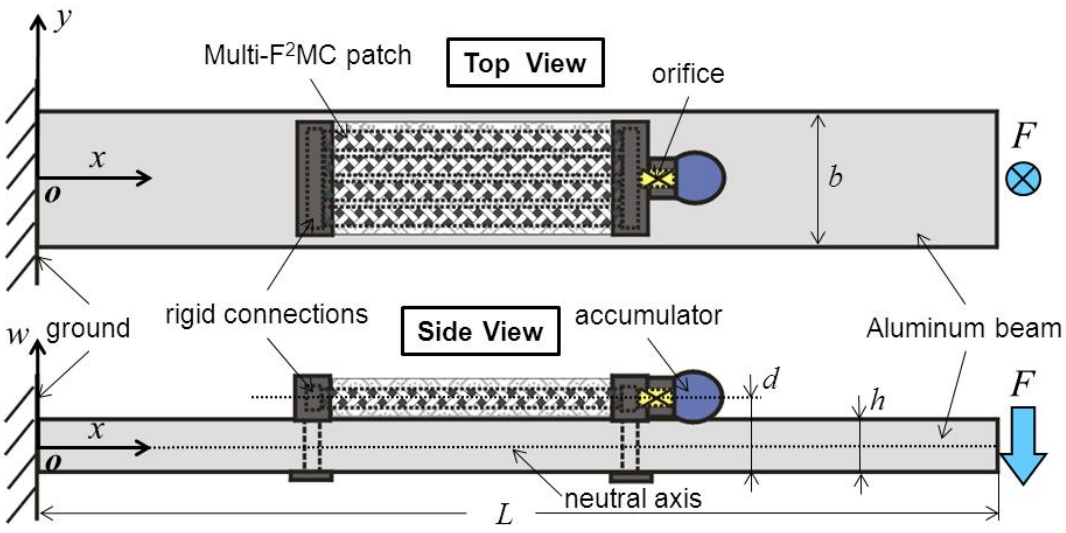

Figure 4-2. Schematic of multi-F^{2}MC patch attached to a cantilever beam

4.1 Mathematical Modeling

4.1.1 Cantilever Beam Model

Figure 4-3 shows the loads on the F^{2}MC patch and the cantilever beam. Point ***o*** is the origin of the coordinate system and the *x*-axis follows the beam centroid. The F^{2}MC patch is rigidly attached to the beam at locations x_1 and x_2. Beam bending causes the F^{2}MC tubes to be stretched or compressed by an axial force F_t. Similarly, the beam is subject to axial force F_t and moment

$$M = F_t d, \tag{4.1}$$

where d is the distance between the centerline of the patch and neutral axis of the beam, as shown in Figure 4-2. The beam is assumed to be inextensible in the longitudinal direction so the effects of the axial force F_t on the beam are neglected.

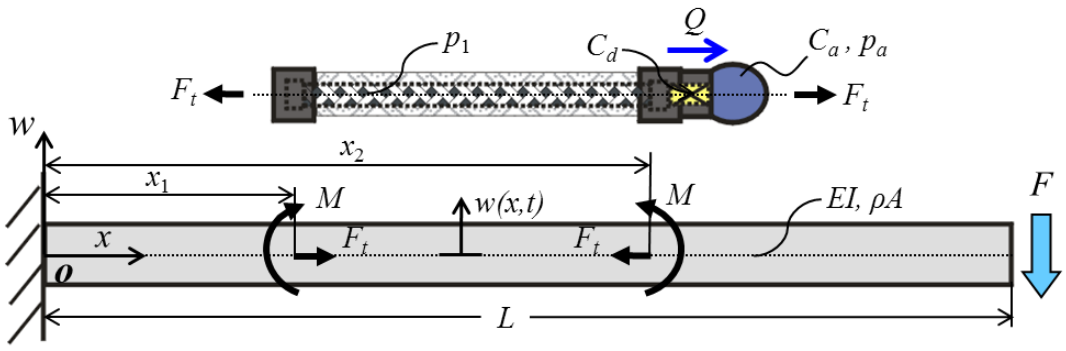

Figure 4-3. The F^{2}MC patch and the cantilever beam (shown separated for clarity)

Under Euler-Bernoulli assumptions, the transverse displacement of the beam, $w(x,t)$, is governed by

$$\rho A\ddot{w} + C\dot{w} + EIw'''' = 0 \text{ for } x \in (0, L), \tag{4.2}$$

where $\dot{()}$ and $()'$ indicate partial differentiation with respect to time, *t*, and *x*, respectively, ρ is the mass density of the beam, *A* is its cross-sectional area, *C* is the damping coefficient, *E* is the Young's modulus, and *I* is the area moment of inertia of the cross-section.

Taking the Laplace transform of Equation (4.2) with zero initial conditions,

$$s^2\rho AW + sCW + EIW'''' = 0, \tag{4.3}$$

where $W(x,s) = \mathcal{L}\{w(x,t)\}$.

After rearranging, we have

$$-\lambda^4 W(x,s) + W''''(x,s) = 0, \tag{4.4}$$

where

$$\lambda^4 = -\frac{s^2\rho A + sC}{EI}. \tag{4.5}$$

The beam has three domains ($x \in (0,x_1) \cup (x_1,x_2) \cup (x_2,L)$), so the general solution is

$$W(x,s) = \begin{cases} W_1(x,s) = A_1 sin\lambda x + B_1 cos\lambda x + C_1 sinh\lambda x + D_1 cosh\lambda x, & x \in (0,x_1) \\ W_2(x,s) = A_2 sin\lambda x + B_2 cos\lambda x + C_2 sinh\lambda x + D_2 cosh\lambda x, & x \in (x_1,x_2), \\ W_3(x,s) = A_3 sin\lambda x + B_3 cos\lambda x + C_3 sinh\lambda x + D_3 cosh\lambda x, & x \in (x_2,L) \end{cases} \tag{4.6}$$

where the constants A_n, B_n, C_n, and D_n (n = 1, 2, 3) are found from the boundary conditions:

(1) The left end (x = 0) of the beam is clamped, so

$$W_1(0,s) = 0, \text{ and} \tag{4.7}$$

$$W_1'(0,s) = 0. \tag{4.8}$$

(2) A moment balance at $x = x_1$ yields

$$EI[W_2''(x_1,s) - W_1''(x_1,s)] = \mathcal{M}(s). \tag{4.9}$$

where $\mathcal{M}(s) = \mathcal{L}\{M(t)\}$. Continuity requires

$$W_1(x_1,s) = W_2(x_1,s), \tag{4.10}$$

$$W_1'(x_1,s) = W_2'(x_1,s), \text{ and} \tag{4.11}$$

$$W_1'''(x_1,s) = W_2'''(x_1,s). \tag{4.12}$$

(3) Similarly, a moment balance at $x = x_2$ gives

$$EI[W_2''(x_2, s) - W_3''(x_2, s)] = \mathcal{M}(s), \tag{4.13}$$

and the continuity conditions are

$$W_2(x_2, s) = W_3(x_2, s), \tag{4.14}$$

$$W_2'(x_2, s) = W_3'(x_2, s), \text{ and} \tag{4.15}$$

$$W_2'''(x_2, s) = W_3'''(x_2, s). \tag{4.16}$$

(4) Shear and moment balances at the tip ($x = L$) yield

$$EIW_3'''(L, s) = \mathcal{F}(s), \text{ and} \tag{4.17}$$

$$EIW_3''(L, s) = 0, \tag{4.18}$$

where $\mathcal{F}(s) = \mathcal{L}\{F(t)\}$. Standard sign conventions for moment and shear force are used (Gere and Timoshenko, 1997).

4.1.2 Three-layer F^{2}MC Tube Model

The F^{2}MC tubes in this work are modeled as infinitely long hollow cylinders with polymer inner and outer layers surrounding a middle layer consisting of two families of stainless steel fibers wound at $\pm\alpha$ to the longitudinal axis of the tube. Figure 4-4 shows the loading on the three-layer composite shell and defines the radii a_1 and a_2 of the inner layer and a_3 and a_4 of outer layer. The axial force F_s acts on the F^{2}MC tube and balances the axial components on individual layers,

$$F_s = F_1 + F_2 + F_3, \tag{4.19}$$

where F_1, F_2, and F_3 are the axial force resultants on the inner, middle, and outer layers of the F^{2}MC tube, respectively.

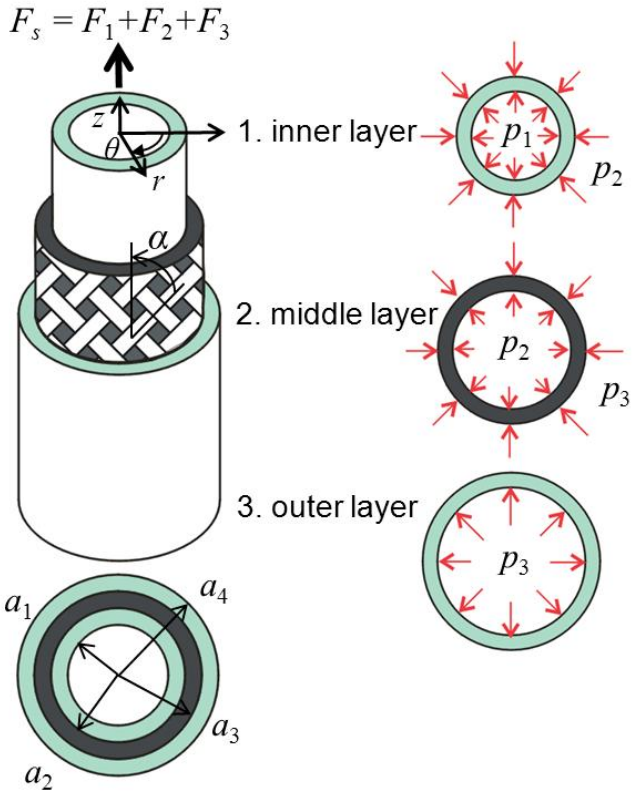

Figure 4-4. Axial force and pressure loading on the three-layer F[2]MC tube

The axial force F_s on the patch can also be obtained from the force balance at the end plug in Figure 4-3,

$$F_s = \frac{1}{N}F_t + p_1\pi a_1^2, \tag{4.20}$$

where p_1 is the internal pressure and N is the number of F[2]MC tubes in the patch.

1) Middle layer

The middle fiber reinforced layer is modeled as an orthotropic cylinder with axial force F_2, and pressures p_2 and p_3 on the interior and exterior surfaces, respectively. Lekhnitskii's solution (Lekhnitskii, 1963) for the axisymmetric stress distributions is

$$\sigma_r^{(m)} = \frac{p_2c^{k+1}-p_3}{1-c^{2k}}\eta^{k-1} + \frac{p_3c^{k-1}-p_2}{1-c^{2k}}c^{k+1}\eta^{-k-1}$$

$$+CK[1 - \frac{1-c^{k+1}}{1-c^{2k}}\eta^{k-1} - \frac{1-c^{k-1}}{1-c^{2k}}c^{k+1}\eta^{-k-1}], \tag{4.21}$$

$$\sigma_\theta^{(m)} = \frac{p_2 c^{k+1} - p_3}{1-c^{2k}} k\eta^{k-1} - \frac{p_3 c^{k-1} - p_2}{1-c^{2k}} k c^{k+1} \eta^{-k-1}$$

$$+\mathcal{C}K[1 - \frac{1-c^{k+1}}{1-c^{2k}} k\eta^{k-1} + \frac{1-c^{k-1}}{1-c^{2k}} k c^{k+1} \eta^{-k-1}], \quad (4.22)$$

$$\sigma_z^{(m)} = \mathcal{C} - \frac{1}{a_{33}}(a_{13}\sigma_r^{(m)} + a_{23}\sigma_\theta^{(m)}), \quad (4.23)$$

where r, θ, and z are the radial, hoop, and longitudinal directions as shown in Figure 4-4,

$$c = \frac{a_2}{a_3}, \quad (4.24)$$

$$\eta = \frac{r}{a_3}, \quad (4.25)$$

$$k = \sqrt{\frac{\beta_{11}}{\beta_{22}}}, \quad (4.26)$$

$$K = \frac{a_{23} - a_{13}}{\beta_{11} - \beta_{22}}, \quad (4.27)$$

and

$$\beta_{11} = a_{11} - \frac{a_{13}^2}{a_{33}}, \quad (4.28)$$

$$\beta_{22} = a_{22} - \frac{a_{23}^2}{a_{33}}. \quad (4.29)$$

The a_{ij} terms are the 3-dimensional effective compliance constants calculated from the fiber angle and the homogenized properties of the middle layer in the cylindrical coordinate system (Sun and Li, 1988). To determine the homogenized properties of the $\pm\alpha$ composite layer, the unidirectionally reinforced $+\alpha$ and $-\alpha$ sub-layers are assumed to be transversely isotropic. These layers therefore have five independent elastic constants: longitudinal Young's modulus, E_1, transverse Young's modulus, E_2, longitudinal Poisson's ratios, v_{12}, transverse (out-of-plane) Poisson's ratio, v_{23}, and longitudinal shear modulus, G_{12}. The axial force

$$F_2 = 2\pi \int_{a_2}^{a_3} \sigma_z^{(m)} r dr, \quad (4.30)$$

from which the constant $\mathcal{C}$ in Equations (4.21)-(4.23) can be solved as a function of pressures p_2 and p_3 and axial force F_2. The strain distributions in the middle fiber reinforced layer are

$$\varepsilon_r^{(m)} = a_{11}\sigma_r^{(m)} + a_{12}\sigma_\theta^{(m)} + a_{13}\sigma_z^{(m)}, \tag{4.31}$$

$$\varepsilon_\theta^{(m)} = a_{12}\sigma_r^{(m)} + a_{22}\sigma_\theta^{(m)} + a_{23}\sigma_z^{(m)}, \tag{4.32}$$

$$\varepsilon_z^{(m)} = a_{13}\sigma_r^{(m)} + a_{23}\sigma_\theta^{(m)} + a_{33}\sigma_z^{(m)}. \tag{4.33}$$

2) Inner and outer layers

The inner and outer layers are modeled as infinitely long isotropic cylinders with axial force and pressure loading. For example, axial force resultant F_1 and pressures p_1 and p_2 act on the inner layer. If the inner layer is neat polyurethane with Young's modulus E_m and Poisson's ratio v, then the stress distribution (Boresi and Schmidt, 2003) is

$$\sigma_r^{(i)} = \frac{p_1 a_1^2 - p_2 a_2^2}{a_2^2 - a_1^2} - \frac{a_1^2 a_2^2 (p_1 - p_2)}{r^2 (a_2^2 - a_1^2)}, \tag{4.34}$$

$$\sigma_\theta^{(i)} = \frac{p_1 a_1^2 - p_2 a_2^2}{a_2^2 - a_1^2} + \frac{a_1^2 a_2^2 (p_1 - p_2)}{r^2 (a_2^2 - a_1^2)}, \tag{4.35}$$

$$\sigma_z^{(i)} = \frac{F_1}{\pi (a_2^2 - a_1^2)}, \tag{4.36}$$

and the strains can be calculated using Hooke's law

$$\varepsilon_r^{(i)} = \frac{1}{E_m}[\sigma_r^{(i)} - \nu(\sigma_\theta^{(i)} + \sigma_z^{(i)})], \tag{4.37}$$

$$\varepsilon_\theta^{(i)} = \frac{1}{E_m}[\sigma_\theta^{(i)} - \nu(\sigma_r^{(i)} + \sigma_z^{(i)})], \tag{4.38}$$

$$\varepsilon_z^{(i)} = \frac{1}{E_m}[\sigma_z^{(i)} - \nu(\sigma_r^{(i)} + \sigma_\theta^{(i)})]. \tag{4.39}$$

Similarly, the stresses and strains in the outer layer can be calculated by replacing F_1 with F_3, p_1 with p_3, and p_2 with zero in the above six equations.

3) Boundary conditions

It is assumed that the three-layer F^{2}MC structure follows a generalized plane strain solution. Therefore, the axial strains in the three layers are the same,

$$\varepsilon_z^{(i)} = \varepsilon_z^{(m)}, \tag{4.40}$$

$$\varepsilon_z^{(m)} = \varepsilon_z^{(o)}. \tag{4.41}$$

In the radial direction, the assumption of perfect bonding between layers means that the hoop strains at the interface are equal,

$$\varepsilon_\theta^{(i)}|_{r=a_2} = \varepsilon_\theta^{(m)}|_{r=a_2}, \tag{4.42}$$

$$\varepsilon_\theta^{(m)}|_{r=a_3} = \varepsilon_\theta^{(o)}|_{r=a_3}. \tag{4.43}$$

The tube is assumed to possess a large length over diameter ratio so that the end restraints have a negligible effect on overall deformation. Given the geometry and material properties of middle reinforced layer and polyurethane layers, the solutions for axial and hoop strains in the F^{2}MC tube can be calculated as a function of F_s and p_1 based on Equations (4.19) and (4.40-4.43).

4.1.3 Multi-F^{2}MC Patch Model

The fluid volume change ratio of an individual F^{2}MC tube can be defined as

$$\frac{\Delta V}{V_0} = \frac{V - V_0}{V_0}, \tag{4.44}$$

where $\Delta V(t)$ is the internal volume change, V is the volume after deformation,

$$V = \pi\left[a_1\left(1 + \varepsilon_\theta|_{r=a_1}\right)\right]^2 (x_2 - x_1)(1 + \varepsilon_z), \tag{4.45}$$

and V_0 is the initial (undeformed) volume,

$$V_0 = \pi a_1^2 (x_2 - x_1). \tag{4.46}$$

Substituting Equations (4.45) and (4.46) into Equations (4.44) yields

$$\frac{\Delta V}{V_0} = \varepsilon_z + 2\varepsilon_\theta|_{r=a_1}, \tag{4.47}$$

where higher order strain terms have been neglected. The axial and hoop strains

$$\varepsilon_z = \varphi_1 F_s + \varphi_2 p_1, \tag{4.48}$$

$$\varepsilon_\theta|_{r=a_1} = \varphi_3 F_s + \varphi_4 p_1, \tag{4.49}$$

where φ_n (n = 1,…,4) are constants that depend on the geometry and properties of the FMC shell.

Taking the compressibility of the fluid into account, the fluid volume pumped out of the F^{2}MC patch, which consists of N F^{2}MC tubes, is

$$\Delta V_f = N[\Delta V - \left(-\tfrac{p_1}{B}V_0\right)] = \left(\tfrac{\Delta V}{V_0} + \tfrac{p_1}{B}\right) NV_0, \tag{4.50}$$

where B is bulk modulus of the working fluid. The fluid volume flow rate

$$Q = -\Delta \dot{V}_f = NS_Q \dot{F}_s + NT_Q \dot{p}_1, \tag{4.51}$$

where

$$S_Q = -(\varphi_1 + 2\varphi_3)V_0, \tag{4.52}$$

$$T_Q = -\left(\varphi_2 + 2\varphi_4 + \tfrac{1}{B}\right)V_0. \tag{4.53}$$

The internal pressure of the accumulator, p_a, and the flow rate Q are governed by the equations of the orifice

$$p_1 - p_a = \tfrac{1}{C_d}Q \tag{4.54}$$

and the accumulator

$$\tfrac{dp_a}{dt} = \tfrac{1}{C_a}Q, \tag{4.55}$$

where C_d is the flow coefficient and C_a is the accumulator capacitance.

Equations (4.20), (4.48), (4.51), (4.54), and (4.55) are combined and solved in the Laplace domain (with zero initial conditions) to find the transfer function from the axial force $\mathcal{F}_t(s) = \mathcal{L}\{F_t(t)\}$ to the axial strain $\mathcal{E}_z(s) = \mathcal{L}\{\varepsilon_z(t)\}$ of the patch as follows,

$$\mathcal{E}_z(s) = G_t(s)\mathcal{F}_t(s), \tag{4.56}$$

where

$$G_t(s) = \tfrac{C_a\left(\varphi_1 T_Q - \varphi_2 S_Q\right)s + C_d\left(\varphi_1 T_Q - \varphi_2 S_Q\right) - \varphi_1 C_a C_d/N}{NC_a(T_Q + \pi a_1^2 S_Q)s + NC_d(T_Q + \pi a_1^2 S_Q) - C_a C_d}. \tag{4.57}$$

4.1.4 F^{2}MC Patch and Beam Coupling

The F^{2}MC tubes in the patch have uniform axial strain as required by the Lekhnitskii's solution. Therefore, the length change of the F^{2}MC tube,

$$\Delta L(s) = \mathcal{E}_z(s)(x_2 - x_1) = -d[W_2'(x_2, s) - W_2'(x_1, s)], \tag{4.58}$$

is proportional to the slope difference at the bonding locations.

4.1.5 Transfer Function from Tip Force to Tip displacement

Solving Equations (4.1), (4.56), and (4.58) for the reaction moment results in

$$\mathcal{M}(\mathrm{s}) = \tfrac{1}{G(s)}[W_2'(x_2, s) - W_2'(x_1, s)], \tag{4.59}$$

where

$$G(s) = \tfrac{x_1 - x_2}{d^2} G_t(s). \tag{4.60}$$

Substitution of Equations (4.6) and (4.59) into the boundary conditions (4.7)-(4.18) yields

$$\mathbf{A}\boldsymbol{v} = \boldsymbol{b}\mathcal{F}(s), \tag{4.61}$$

where

$$\boldsymbol{A} = \begin{bmatrix}
0 & 1 & 0 & 1 & 0 & 0 & 0 & 0 & 0 & 0 & 0 & 0 \\
1 & 0 & 1 & 0 & 0 & 0 & 0 & 0 & 0 & 0 & 0 & 0 \\
GEI\lambda \mathrm{S}\lambda x_1 & GEI\lambda \mathrm{C}\lambda x_1 & -GEI\lambda \mathrm{Sh}\lambda x_1 & -GEI\lambda \mathrm{Ch}\lambda x_1 & A_{35} & A_{36} & A_{37} & A_{38} & 0 & 0 & 0 & 0 \\
0 & 0 & 0 & 0 & A_{45} & A_{46} & A_{47} & A_{48} & GEI\lambda \mathrm{S}\lambda x_2 & GEI\lambda \mathrm{C}\lambda x_2 & -GEI\lambda \mathrm{Sh}\lambda x_2 & -GEI\lambda \mathrm{Ch}\lambda x_2 \\
0 & 0 & 0 & 0 & 0 & 0 & 0 & 0 & -\mathrm{C}\lambda L & \mathrm{S}\lambda L & \mathrm{Ch}\lambda L & \mathrm{Sh}\lambda L \\
0 & 0 & 0 & 0 & 0 & 0 & 0 & 0 & -\mathrm{S}\lambda L & -\mathrm{C}\lambda L & \mathrm{Sh}\lambda L & \mathrm{Ch}\lambda L \\
\mathrm{S}\lambda x_1 & \mathrm{C}\lambda x_1 & \mathrm{Sh}\lambda x_1 & \mathrm{Ch}\lambda x_1 & -\mathrm{S}\lambda x_1 & -\mathrm{C}\lambda x_1 & -\mathrm{Sh}\lambda x_1 & -\mathrm{Ch}\lambda x_1 & 0 & 0 & 0 & 0 \\
\mathrm{C}\lambda x_1 & -\mathrm{S}\lambda x_1 & \mathrm{Ch}\lambda x_1 & \mathrm{Sh}\lambda x_1 & -\mathrm{C}\lambda x_1 & \mathrm{S}\lambda x_1 & -\mathrm{Ch}\lambda x_1 & -\mathrm{Sh}\lambda x_1 & 0 & 0 & 0 & 0 \\
-\mathrm{C}\lambda x_1 & \mathrm{S}\lambda x_1 & \mathrm{Ch}\lambda x_1 & \mathrm{Sh}\lambda x_1 & \mathrm{C}\lambda x_1 & -\mathrm{S}\lambda x_1 & -\mathrm{Ch}\lambda x_1 & -\mathrm{Sh}\lambda x_1 & 0 & 0 & 0 & 0 \\
0 & 0 & 0 & 0 & \mathrm{S}\lambda x_2 & \mathrm{C}\lambda x_2 & \mathrm{Sh}\lambda x_2 & \mathrm{Ch}\lambda x_2 & -\mathrm{S}\lambda x_2 & -\mathrm{C}\lambda x_2 & -\mathrm{Sh}\lambda x_2 & -\mathrm{Ch}\lambda x_2 \\
0 & 0 & 0 & 0 & \mathrm{C}\lambda x_2 & -\mathrm{S}\lambda x_2 & \mathrm{Ch}\lambda x_2 & \mathrm{Sh}\lambda x_2 & -\mathrm{C}\lambda x_2 & \mathrm{S}\lambda x_2 & -\mathrm{Ch}\lambda x_2 & -\mathrm{Sh}\lambda x_2 \\
0 & 0 & 0 & 0 & -\mathrm{C}\lambda x_2 & \mathrm{S}\lambda x_2 & \mathrm{Ch}\lambda x_2 & \mathrm{Sh}\lambda x_2 & \mathrm{C}\lambda x_2 & -\mathrm{S}\lambda x_2 & -\mathrm{Ch}\lambda x_2 & -\mathrm{Sh}\lambda x_2
\end{bmatrix}, \boldsymbol{v} = \begin{Bmatrix} A_1 \\ B_1 \\ C_1 \\ D_1 \\ A_2 \\ B_2 \\ C_2 \\ D_2 \\ A_3 \\ B_3 \\ C_3 \\ D_3 \end{Bmatrix}, \boldsymbol{b} = \begin{Bmatrix} 0 \\ 0 \\ 0 \\ 0 \\ \frac{1}{EI\lambda^3} \\ 0 \\ 0 \\ 0 \\ 0 \\ 0 \\ 0 \\ 0 \end{Bmatrix}, \tag{4.62}$$

and

$$\begin{cases} A_{35} = -GEI\lambda \mathrm{S}\lambda x_1 - \mathrm{C}\lambda x_2 + \mathrm{C}\lambda x_1 \\ A_{36} = -GEI\lambda \mathrm{C}\lambda x_1 + \mathrm{S}\lambda x_2 - \mathrm{S}\lambda x_1 \\ A_{37} = GEI\lambda \mathrm{Sh}\lambda x_1 - \mathrm{Ch}\lambda x_2 + \mathrm{Ch}\lambda x_1 \\ A_{38} = GEI\lambda \mathrm{Ch}\lambda x_1 - \mathrm{Sh}\lambda x_2 + \mathrm{Sh}\lambda x_1 \end{cases}, \begin{cases} A_{45} = -GEI\lambda \mathrm{S}\lambda x_2 - \mathrm{C}\lambda x_2 + \mathrm{C}\lambda x_1 \\ A_{46} = -GEI\lambda \mathrm{C}\lambda x_2 + \mathrm{S}\lambda x_2 - \mathrm{S}\lambda x_1 \\ A_{47} = GEI\lambda \mathrm{Sh}\lambda x_2 - \mathrm{Ch}\lambda x_2 + \mathrm{Ch}\lambda x_1 \\ A_{48} = GEI\lambda \mathrm{Ch}\lambda x_2 - \mathrm{Sh}\lambda x_2 + \mathrm{Sh}\lambda x_1 \end{cases}, \tag{4.63}$$

with S, C, Sh, Ch, and *G* representing *sin*, *cos*, *sinh*, *cosh*, and *G*(*s*), respectively.

The displacement at the beam tip is

$$W(L,s) = A_3 sin\lambda L + B_3 cos\lambda L + C_3 sinh\lambda L + D_3 cosh\lambda L, \quad (4.64)$$

and the transfer function from tip force to tip displacement is

$$\frac{W(L,s)}{\mathcal{F}(s)} = \boldsymbol{c}_w \mathbf{A}^{-1} \boldsymbol{b} = H(s), \quad (4.65)$$

where $\boldsymbol{c}_w = [0\ 0\ 0\ 0\ 0\ 0\ 0\ 0\ sin\lambda L\ \ cos\lambda L\ sinh\lambda L\ \ cosh\lambda L$. The frequency response function (FRF) is $|H(j\omega)|$ plotted with respect to frequency f, and $\omega = 2\pi f$.

Table 4-1. Model Parameters of F^{2}MC-Beam System

Component	Property	Value
Middle Layer of F^{2}MC Tube	E_1	52 GPa
	E_2	18.7 MPa
	v_{12}	0.45
	v_{23}	0.93
	G_{12}	6.24 MPa
	α	±27 °
Inner/Outer Layers of F^{2}MC Tube	E_m	11 MPa
	v	0.498
	a_1	0.83 mm
	a_2	0.90 mm
	a_3	0.95 mm
	a_4	1.02 mm
Aluminum Beam	E	70 GPa
	ρ	2700 kg/m^3
	C	0.2 N·s/m
	L	310 mm
	b	26 mm
	h	1.6 mm
F^{2}MC Patch	x_1	0, [0~310 mm]*
	x_2 [$x_1 < x_2$]	115mm, [0~310 mm]*
	N	2
	d	9 mm
Fluidic Circuit	C_d	[10^{-13}~10^{-10} m^3/s Pa]*
	B	25 MPa
	C_a	1.5×10^{-9} m^3/Pa

*Note: The values inside "[ ]" are the ranges in the design space study.

4.2 Experiments and Validation

Table I shows the parameters for the miniature F^{2}MC tubes, fluidic circuit, and cantilever beam used in the experimental study. The cantilever beam is made of aluminum, while the F^{2}MC tubes are custom-made braided tubing. The F^{2}MC tubes have three layers: neat polyurethane for the inner and outer layers and stainless steel reinforced polyurethane for the middle layer. The working fluid is water. The beam damping coefficient, C = 0.2 N·s/m, provides 0.5% damping in the first mode using the half-power method (Fu and He, 2001). Baseline model parameters as well as the full range of model parameters allowed in the design space study are listed in Table I. The properties of the three layers of the F^{2}MC tubes come from experimental measurements reported elsewhere (Vashisth *et al.*, 2013).

Figure 4-5 shows the a typical modal testing setup to acquire the frequency response function (FRF) of a general F^{2}MC integrated beam structure with shock hammer and Doppler laser vibration (DLV) as excitation and response sensor, respectively.

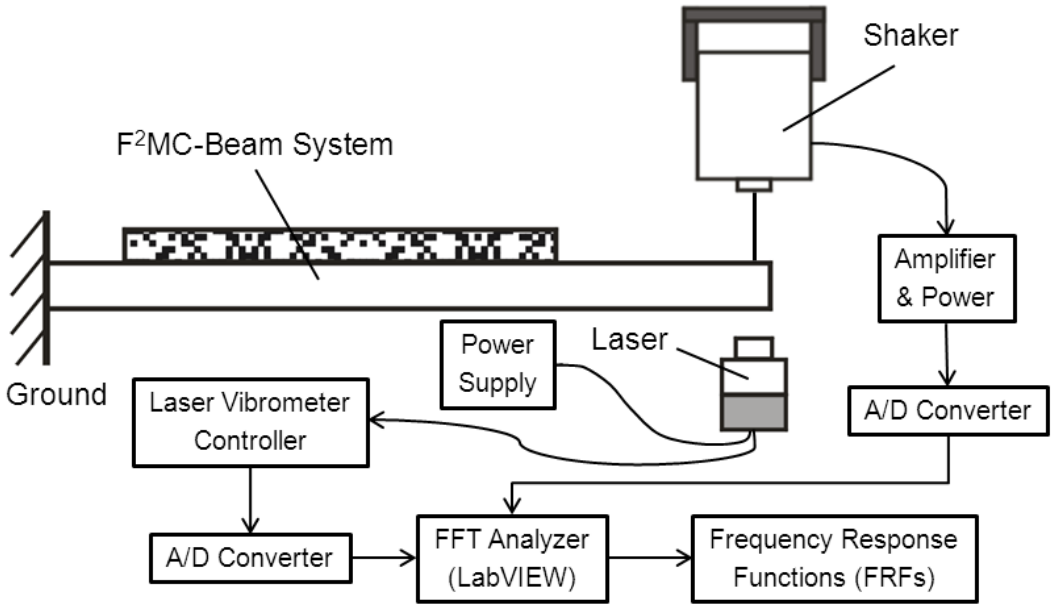

Figure 4-5. Schematic of experimental setup for modal testing of F^{2}MC-beam system

In Figure 4-6 the experimental setup and the equipment used to acquire the system frequency response are demonstrated in details. The F^2MC beam is mounted on an aluminum frame at one end and the other end is fastened to the stinger of an electro-dynamic shaker. The shaker provides a swept-sine signal to excite the cantilever beam, and the force transducer between the beam and the shaker measures the force acting on the beam tip. The laser Doppler vibrometer captures the displacement response signal under the excitation. A LabVIEW-based data acquisition platform performs A/D and D/A conversion, amplification, and FFT analysis. The shaker adds rotational stiffness and added mass at the cantilever beam tip. Together with masses of the fittings, they are included in the model by changing boundary conditions at the attachment locations.

During the experiment, the swept-sine function varies frequency from 0 Hz to 130 Hz. The sampling rate is 10,000 Hz. The number of data points is 300,000. Therefore, the average running time for one round is 30 s. Rectangular window was used to capture the signals. In order to minimize noise and improve curve smoothness, the frequency response was calculated by averaging 3 measurements. Finally, the sensor sensitivities need to be integrated so that the DAC values can be translated into physical values. In this experiment, the laser sensitivity is 640 um/V and the load cell sensitivity is 10,880 mV/kN .

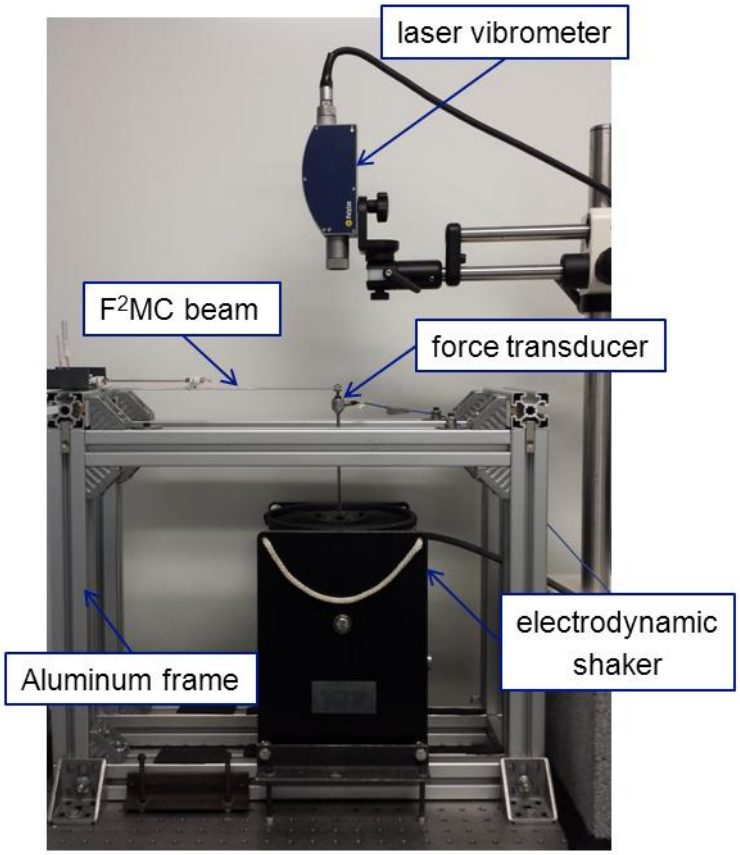

Figure 4-6. Experimental setup for modal analysis of F^2MC beam system.

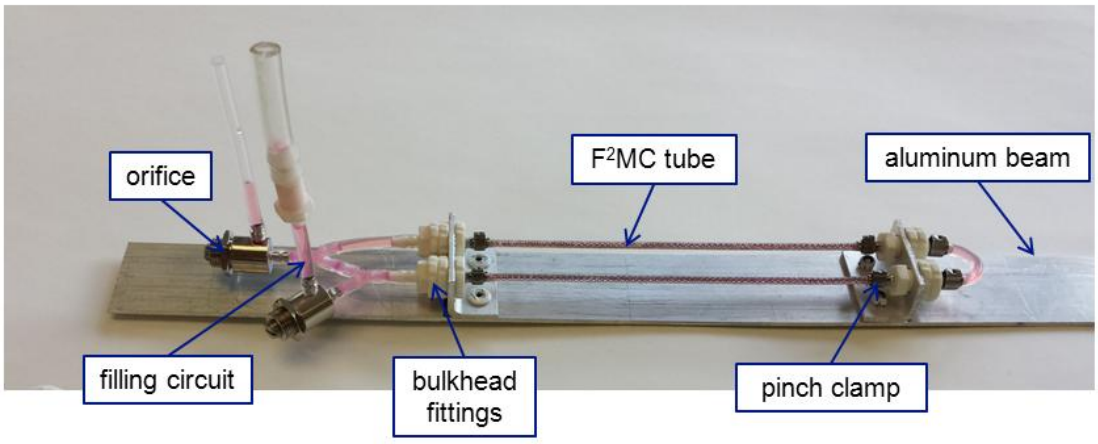

Figure 4-7. Experimental prototype of the F^2MC integrated beam with fluidic circuit.

Figure 4-7 shows a detail photograph of the F^2MC beam prototype. The aluminum cantilever beam has two F^2MC tubes attached at x_1 = 0 mm and x_2 = 115 mm. The F^2MC tubes are connected to panel mount bulkhead fittings with double pinch clamps. The tubes and fittings are attached to aluminum angles at both ends and the assembly is attached to the cantilever beam at the desired position using pop rivets. Water is injected into the tubes through the filling circuit. Plastic tubing guides the fluid from the F^2MC tubes to a needle valve with an adjustable orifice. The tubing is made of Teflon PTFE material and has an inner diameter of 1.6 mm and an outer diameter of 3.2 mm. After the filling process, the filling circuit is blocked by closing the filling valve. Fluid pumping through the orifice dissipates energy and introduces damping to the cantilever beam.

All of the parameters for the experiment shown in Table I are calculated from independent measurements except the fluid bulk modulus and the flow coefficient. The fluid bulk modulus is reduced from the handbook value until the static stiffness and first natural frequency match the experiment for the closed valve case. Closing the valve to the inertia track stiffens the beam and the resulting static stiffness and first natural frequency can be experimentally measured and predicted by the model. The flow coefficient is increased until the shape of the theoretically predicted frequency response curve most closely matches the experimental measurements.

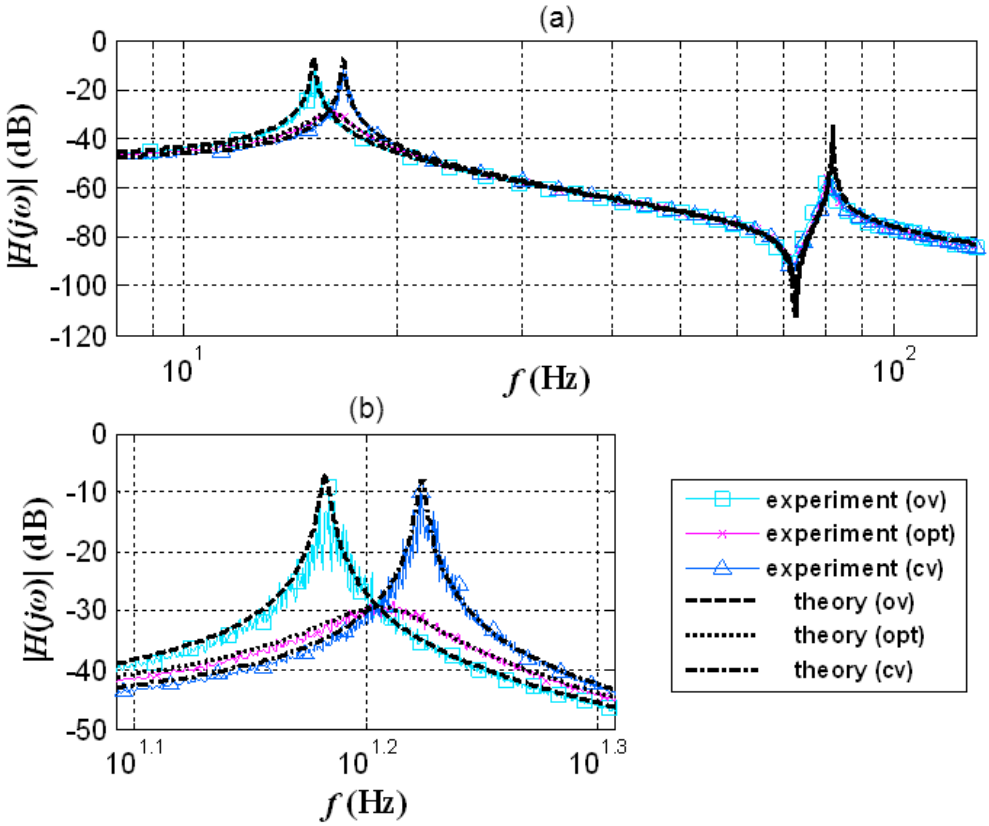

Figure 4-8. F^{2}MC beam experimental and theoretical frequency response functions corresponding to open valve (ov), optimal (opt), and closed valve (cv) conditions: (a) First and second modes; (b) zoom-in view of first mode. [Units of $H(j\omega)$: m/N]

Figure 4-8 compares the experimental results and theoretical predictions for open valve, optimally closed valve, and fully closed valve cases. Figure 4-8(a) shows a comparison of the first and second modes and Figure 4-8(b) shows a zoom-in view of the first mode. The model matches the experimental results to a remarkable degree in all three cases in the first mode. The model slightly under predicts the damping of the second mode but still provides a very good prediction of the effect of the F^{2}MC damping treatment on the second mode response. The first resonant frequency of the F^{2}MC beam increases from 15 Hz to 17 Hz when the valve is closed because the volume change of the F^{2}MC tube is constrained and internal pressurization resists extension, increasing the axial stiffness of the tube. Energy dissipation from the F^{2}MC damping

treatment depends on the flow rate through the orifice and orifice flow coefficient. For the open valve case the flow coefficient is almost zero and there is very little dissipation through the orifice and therefore low damping. For the closed valve case, the flow rate is zero so the experiment and theory predict low damping. There exists an optimal orifice size that maximizes the energy dissipation. With a flow coefficient C_d = 3×10^{-12} m^3/(s·Pa), a damping ratio of 5.3% is achieved from the treatment as shown by the middle curve. The tip response of the cantilever beam is reduced by more than 92% with optimal F^{2}MC damping treatment.

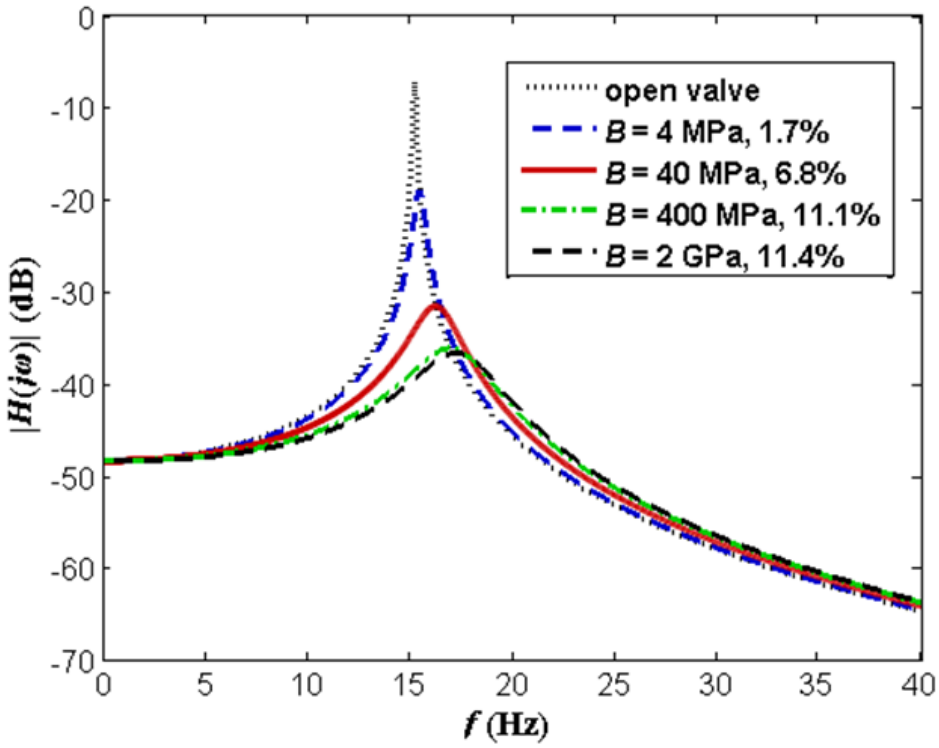

Figure 4-9. Maximally damped (optimal orifice size) theoretical frequency response functions with fluid bulk modulus ranging from 4 MPa to 2 GPa. The legend includes first mode damping ratios. [Units of $H(j\omega)$: m/N]

To obtain the excellent match between theory and experiment shown in Figure 4-8, the bulk modulus of water is greatly reduced from its published value of 2 GPa to only 25 MPa as shown in Table I. We hypothesize that entrained air bubbles reduce the effective modulus of the

fluid. The small volume of fluid in the < 2 mm diameter tubes means that even small bubbles can appreciably change the effective bulk modulus. Bubbles can easily be trapped in the fittings and internal surfaces of the fluidic circuit. Figure 4-9 shows the predicted effect of fluid bulk modulus on the damping performance. The bulk modulus is varied from 4 MPa to 2 GPa and the damping is maximized by tuning the flow coefficient for each case. The results show that a larger damping ratio is achievable with increasing bulk modulus. For instance, when the bulk modulus increases from 40 MPa to 400 MPa, the maximal damping ratio is enhanced by 63%. However, when the modulus is beyond 400 MPa, the fluid is practically incompressible and the damping enhancement is limited.

In practice, several techniques can increase the effective fluid bulk modulus in the fluidic circuit. First, the fluidic circuit is designed with minimal diameter changes, corners, tees, and elbows where bubbles can form. Second, the circuit is filled slowly and vibrated to dislodge air bubbles. Third, once the circuit is filled, it is bled by passing fluid through the circuit to force bubbles out. Fourth, the fluidic circuit can be pre-pressurized to shrink the bubble diameters and increase the effective bulk modulus. Finally, radially soft fluidic circuit elements (*e.g.* tubing) can flex under pressure, accommodating volume changes with small changes in pressure and giving the same low effective fluid bulk modulus as air bubbles. Therefore, stiff-walled tubing and fittings are used for the fluidic circuit.

In this work, the F^2MC tubes are bonded to the beam at two points. Alternatively, the tubes can also be cast in a soft matrix and then continuously attach to the beam. Two point bonding results in discrete forces at the attached locations, while continuous bonding leads to distributed loads across the attached surface. For small deformation and low frequency application, the integral of the distributed loads should equal the discrete forces. These two bonding approaches can generate same amount of coupling and fluid pumping and thereby integrated fluidic damping. However, when the beam vibrates with large amplitude, two point bonding will induce less fluid

pumping than continuous bonding because the tubes do not follow the same curvatures as the beam. In high frequency applications, the F^2MC tubes can even have vibration mode shapes excited that differ from the beam modes. In those situations, continuous bonding has it advantage of enforcing the tubes to have the same deformation as the beam and maximize the coupling. Therefore, it should be implemented in order to use the model developed in this work.

4.3 Parametric Investigation

To further explore the potential performance of the F^2MC damping treatment on multiple modes of a cantilever beam structure, a design space investigation is performed. Three parameters are varied: orifice flow coefficient C_d and attachment point locations x_1 and x_2. The square bracketed numbers in Table I show the physically reasonable ranges used for these parameters.

Figure 4-10 shows the theoretical damping ratios of the first and second modes for the F^2MC-beam using one hundred and fifty thousand designs randomly sampled from the ranges in Table I. Each circle corresponds to a design with specific attachment point locations and a specific flow coefficient. The left and right clusters of circles are for the first and second resonant peaks, respectively. The filled circles in Figure 4-10 have damping ratios of over 20% and 10% at the first and second resonances, respectively, representing the best designs.

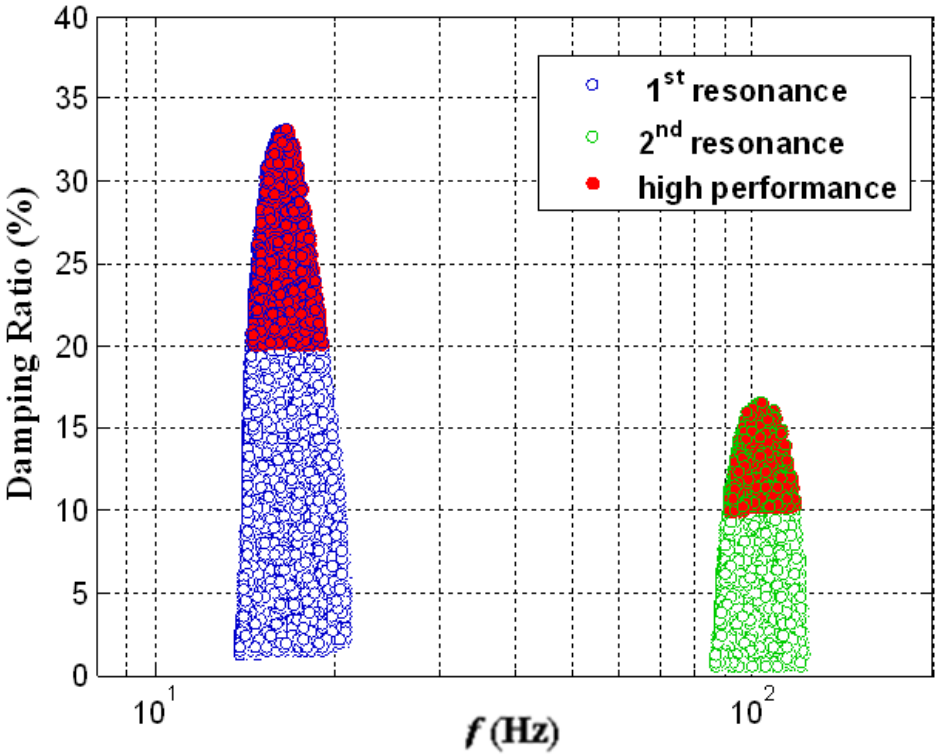

Figure 4-10. Theoretical first and second mode damping ratios for F^{2}MC beam systems with flow coefficients and attachment point locations varied according to the square bracketed ranges in Table I.

The histogram in Figure 4-11(a) shows the attachment point distributions for F^{2}MC beam designs with >20% first mode damping. To achieve maximal first mode damping, the F^{2}MC tube is attached at $x_1/L = 0$ and near $x_2/L = 0.5$. Tube strain is proportional to modal slope difference according to Equation (4.58). Figure 4-11(c) shows that the first modal slope difference is maximized under these conditions. The histogram also demonstrates that the damping is much more sensitive to x_1 than x_2. As long as the left end of the tube is attached near the clamped end, the F^{2}MC tube need not extend to the full length of the beam. The histogram in Figure 4-11(b) shows the attachment point distributions that achieve >10% second mode damping. The results point to the advantage of an F^{2}MC tube attached at $x_1/L = 0.25$ and $x_2/L = 0.8$, maximizing the slope difference in Figure 4-11(d).

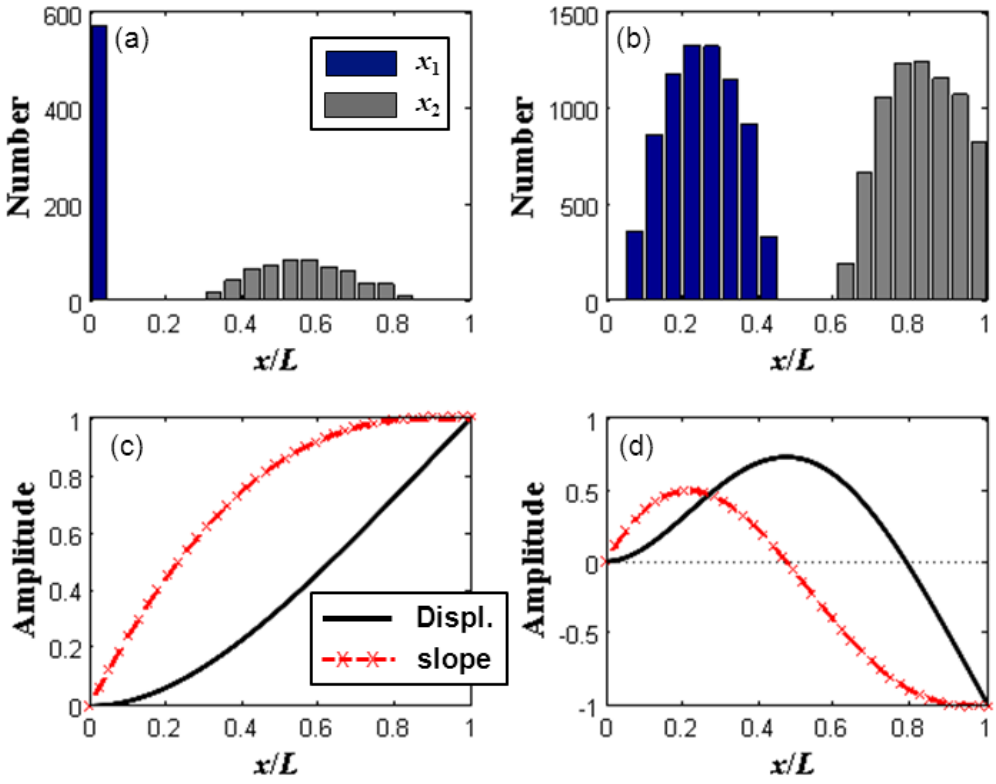

Figure 4-11. Best attachment point locations for F^{2}MC damping treatments: (a) Histogram of left (x_1) and right (x_2) attachment points for >20% first mode damping; (b) Histogram of left (x_1) and right (x_2) attachment points for >10% second mode damping; (c) Normalized first mode displacement and slope distributions; (d) Normalized second mode displacement and slope distributions.

Based on the design space results, damping treatments are designed for the first three modes as shown in Figure 4-12. The frequency response of the bare beam (dotted) has three sharp peaks at resonance frequencies of 14 Hz, 87 Hz, and 244 Hz. Integrating a multi-F^{2}MC patch with the beam and tuning the design parameters introduces significant damping in the first (dashed), second (solid), and third (dash-dotted) modes. Damping ratios of 32%, 16%, and 9.7% are obtained with F^{2}MC-beam designs targeting the first, second, and third modes, respectively. In practice, one could incorporate several damping treatments targeting different modes to

provide broader band damping. Alternatively, the attachment points and flow coefficients could be optimized for less than the maximal damping in more than one mode.

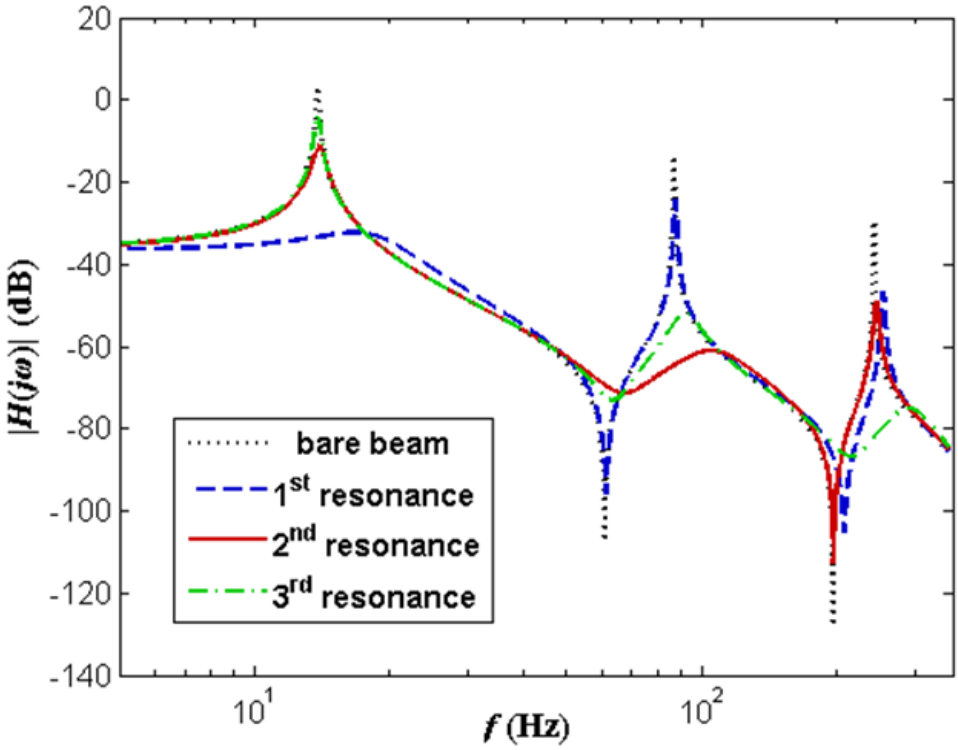

Figure 4-12. Theoretical frequency response functions: Bare beam (dotted), F^{2}MC-beam with C_d = 2.3×10^{-12} m^3/(s·Pa), x_1/L = 0, x_2/L = 0.5 (dashed), F^{2}MC-beam with C_d = 1.5×10^{-11} m^3/(s·Pa), x_1/L = 0.25, x_2/L = 0.8 (solid), and F^{2}MC-beam with C_d = 2.1×10^{-11} m^3/(s·Pa), x_1/L = 0.5, x_2/L = 0.9 (dash-dotted). [Units of $H(j\omega)$: m/N]

Chapter 5

Fluidic Flexible Matrix Composite Vibration Absorber and Isolator for a Cantilever Beam

Figure 5-1 shows the F^{2}MC-beam vibration suppression system investigated in this work. It is composed of a cantilever beam, an F^{2}MC patch, and an external fluidic circuit. The F^{2}MC patch consists of multiple F^{2}MC tubes connected in parallel by end plates with internal fluid manifolds. Under excitation of the tip force $F(t)$, the beam vibration $w(x,t)$ strains the F^{2}MC tubes through the rigid connections. Strain-induced fluid flows through the flow port (or inertia track) and the generated fluid inertia is analogous to the attached mass in the vibration absorber. The accumulator at the end of the inertia track provides the stiffness for the fluidic degree of freedom. The objective of this work is to design and optimize the F^{2}MC-beam system through modeling, experiments, and a parametric study with the goal of predicting, observing, and optimizing a notch in the frequency response at the absorption frequency.

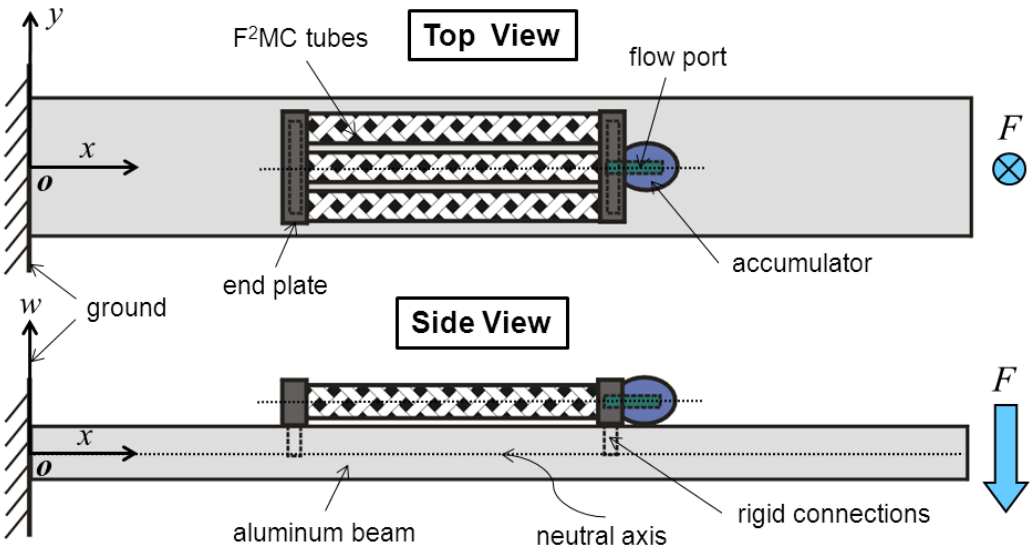

Figure 5-1. Schematic diagram of an F^{2}MC vibration absorber attached to a cantilever beam

5.1 Analytical Model Development

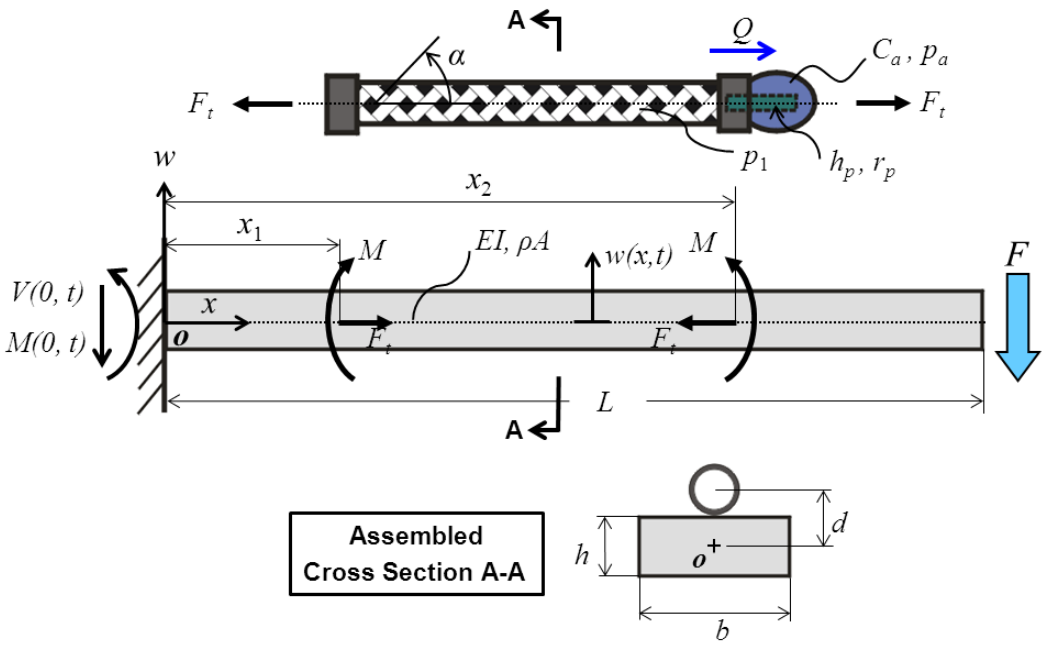

Figure 5-2. Schematic diagram of the F^{2}MC-integrated cantilever beam model: Side view with tube and beam shown separated for clarity (top) and assemble cross section view (bottom).

Figure 5-2 shows a schematic diagram of the F^{2}MC-integrated cantilever beam. Point ***o*** is the origin of the coordinate system and the *x*-axis follows the beam centroid. The cantilever beam has length, *L*, width, *b*, and height, *h*. The F^{2}MC patch is rigidly connected to the beam at x_1 and x_2. Beam bending stretches the F^{2}MC tubes by axial force F_t which has an equal and opposite reaction on the beam and produces the moment

$$M = F_t d, \tag{5.1}$$

where *d* is the distance between the centerline of the tube and neutral axis of the beam, as shown in the assembled cross section view in Figure 5-2. $V(0,t)$ and $M(0,t)$ are the shear force and moment transmitted to the ground during the vibration. The beam is assumed to be inextensible in the longitudinal direction so the effects of the axial force F_t on the beam are neglected.

The cantilever beam model and triple-layer F^{2}MC tube model have been presented in Chapter 4 through Equations (4.2) to (4.43). For simplicity reason, they will not be repeated here.

5.1.1 Fluid System Model

The fluid volume change ratio of the F^{2}MC tube can be defined as

$$\frac{\Delta V}{V_0} = \frac{V - V_0}{V_0}, \tag{5.2}$$

where $\Delta V(t)$ is the volume change,

$$V = \pi\left[a_1\left(1 + \varepsilon_\theta|_{r=a_1}\right)\right]^2 (x_2 - x_1)(1 + \varepsilon_z), \text{ and} \tag{5.3}$$

$$V_0 = \pi a_1^2 (x_2 - x_1). \tag{5.4}$$

Substituting Equations (5.3)-(5.4) into Equations (5.2) yields

$$\frac{\Delta V}{V_0} = \varepsilon_z + 2\varepsilon_\theta|_{r=a_1}, \tag{5.5}$$

where higher order strain terms have been neglected. The axial and hoop strains

$$\varepsilon_z = \varphi_1 F_s + \varphi_2 p_1, \tag{5.6}$$

$$\varepsilon_\theta|_{r=a_1} = \varphi_3 F_s + \varphi_4 p_1, \tag{5.7}$$

where φ_n (n = 1,…,4) are constants that depend on the geometry and properties of the FMC shell.

Taking the compressibility of the fluid into account, the fluid volume pumped out of the F^{2}MC tubes is

$$\Delta V_f = N[\Delta V - \left(-\tfrac{p_1}{B_{w1}} V_0\right)] = \left(\tfrac{\Delta V}{V_0} + \tfrac{p_1}{B_{w1}}\right) N V_0, \tag{5.8}$$

and the fluid volume pumped through the inertia track is

$$\Delta V_p = \Delta V_f - \left(-\tfrac{p_1 + p_a}{2B_{w2}} V_p\right)] = \left(\tfrac{\Delta V}{V_0} + \tfrac{p_1}{B_{w1}}\right) N V_0 + \tfrac{p_1 + p_a}{2B_{w2}} V_p, \tag{5.9}$$

where B_{w1} and B_{w2} are bulk moduli of the working fluid inside the tube and inertia track, respectively, and p_a is the internal pressure of the accumulator. Here, average pressure is used to calculate the fluid compliance inside the inertia track. The fluid volume flow rate

$$Q = -\Delta\dot{V}_p = S_Q\dot{F}_s + T_Q\dot{p_1} + U_Q\dot{p_a}, \tag{5.10}$$

where

$$S_Q = -N(\varphi_1 + 2\varphi_3)V_0, \tag{5.11}$$

$$T_Q = -N\left(\varphi_2 + 2\varphi_4 + \tfrac{1}{B_{w1}}\right)V_0 - \tfrac{1}{2B_{w2}}V_p, \text{ and} \tag{5.12}$$

$$U_Q = -\tfrac{1}{2B_{w2}}V_p. \tag{5.13}$$

Assuming laminar flow inside the inertia track, the governing equation for the fluid system (Kundu and Cohen, 2004) is

$$p_1 - p_a = I_w\dot{Q} + (R + R_z)Q, \tag{5.14}$$

where the flow inertance is

$$I_w = \tfrac{\rho_w h_p}{\pi r_p^2}, \tag{5.15}$$

the flow resistance (Merritt, 1967) is

$$R = \tfrac{8\mu h_p}{\pi r_p^4}\left(1 + \tfrac{2.28 r_p R_n}{32 h_p}\right), \tag{5.16}$$

and R_z represents the energy loss from sources other than head loss in the inertia track (*e.g.* elbows, tees, diameter changes, *etc.*). In Equations (5.15) and (5.16), ρ_w is the fluid density, μ is the dynamic viscosity of fluid, R_n is the Reynolds number, h_p is the length of flow port, and r_p is the radius of the flow port. The assumption of laminar flow through the inertia track is questionable due to the oscillatory flow and wide ranging Reynolds number. Therefore, in the current investigation, the total resistance is a tuning parameter that accounts for all the losses in the fluidic circuit, from both laminar and turbulent sources.

The governing equation for the accumulator is

$$\frac{dp_a}{dt} = \frac{1}{C_a}Q, \tag{5.17}$$

where C_a is the accumulator capacitance.

Equations (4.20), (5.6), (5.10), and (5.14)-(5.17) are combined and solved in the Laplace domain (with zero initial conditions) to find the transfer function from the axial force $\mathcal{F}_t(s) = \mathcal{L}\{F_t(t)\}$ to the axial strain $\mathcal{E}_z(s) = \mathcal{L}\{\varepsilon_z(t)\}$ of the tube as follows,

$$\mathcal{E}_z(s) = G_t(s)\mathcal{F}_t(s), \tag{5.18}$$

where

$$G_t(s) = \frac{(\varphi_1 T_Q - \varphi_2 S_Q)\left[I_W s^2 + (R+R_Z)s + \frac{1}{C_a}\right] - \varphi_1\left(1 - \frac{U_Q}{C_a}\right)}{N\left(T_Q + \pi a_1^2 S_Q\right)\left[I_W s^2 + (R+R_Z)s + \frac{1}{C_a}\right] - N\left(1 - \frac{U_Q}{C_a}\right)}. \tag{5.19}$$

5.1.2 Coupling between F^{2}MC Patch and Beam

The F^{2}MC tube is assumed to undergo uniform axial strain corresponding to the strain calculated along the centerline of the tube. Therefore, the elongation/contraction of the F^{2}MC tube,

$$\Delta L(s) = \mathcal{E}_z(s)(x_2 - x_1) = -d[W_2'(x_2, s) - W_2'(x_1, s)], \tag{5.20}$$

is proportional to the slope difference of the beam between the attachment points.

5.1.3 Transfer Function from Tip Force to Tip displacement

Solving Equations (5.1), (5.18) and (5.20) for reaction moment,

$$\mathcal{M}(s) = \frac{1}{G(s)}[W_2'(x_2, s) - W_2'(x_1, s)], \tag{5.21}$$

where

$$G(s) = \frac{x_1 - x_2}{d^2}G_t(s). \tag{5.22}$$

Substitution of Equations (4.6) and (5.21) into the boundary conditions (4.7)-(4.18) yields

$$\mathbf{A}\boldsymbol{v} = \boldsymbol{b}\mathcal{F}(s). \tag{5.23}$$

where

$$\boldsymbol{A} = \begin{bmatrix} 0 & 1 & 0 & 1 & 0 & 0 & 0 & 0 & 0 & 0 & 0 & 0 \\ 1 & 0 & 1 & 0 & 0 & 0 & 0 & 0 & 0 & 0 & 0 & 0 \\ GEI\lambda S\lambda x_1 & GEI\lambda C\lambda x_1 & -GEI\lambda \mathrm{Sh}\lambda x_1 & -GEI\lambda \mathrm{Ch}\lambda x_1 & A_{35} & A_{36} & A_{37} & A_{38} & 0 & 0 & 0 & 0 \\ 0 & 0 & 0 & 0 & A_{45} & A_{46} & A_{47} & A_{48} & GEI\lambda S\lambda x_2 & GEI\lambda C\lambda x_2 & -GEI\lambda \mathrm{Sh}\lambda x_2 & -GEI\lambda \mathrm{Ch}\lambda x_2 \\ 0 & 0 & 0 & 0 & 0 & 0 & 0 & 0 & -C\lambda L & S\lambda L & Ch\lambda L & Sh\lambda L \\ 0 & 0 & 0 & 0 & 0 & 0 & 0 & 0 & -S\lambda L & -C\lambda L & Sh\lambda L & Ch\lambda L \\ S\lambda x_1 & C\lambda x_1 & Sh\lambda x_1 & Ch\lambda x_1 & -S\lambda x_1 & -C\lambda x_1 & -Sh\lambda x_1 & -Ch\lambda x_1 & 0 & 0 & 0 & 0 \\ C\lambda x_1 & -S\lambda x_1 & Ch\lambda x_1 & Sh\lambda x_1 & -C\lambda x_1 & S\lambda x_1 & -Ch\lambda x_1 & -Sh\lambda x_1 & 0 & 0 & 0 & 0 \\ -C\lambda x_1 & S\lambda x_1 & Ch\lambda x_1 & Sh\lambda x_1 & C\lambda x_1 & -S\lambda x_1 & -Ch\lambda x_1 & -Sh\lambda x_1 & 0 & 0 & 0 & 0 \\ 0 & 0 & 0 & 0 & S\lambda x_2 & C\lambda x_2 & Sh\lambda x_2 & Ch\lambda x_2 & -S\lambda x_2 & -C\lambda x_2 & -Sh\lambda x_2 & -Ch\lambda x_2 \\ 0 & 0 & 0 & 0 & C\lambda x_2 & -S\lambda x_2 & Ch\lambda x_2 & Sh\lambda x_2 & -C\lambda x_2 & S\lambda x_2 & -Ch\lambda x_2 & -Sh\lambda x_2 \\ 0 & 0 & 0 & 0 & -C\lambda x_2 & S\lambda x_2 & Ch\lambda x_2 & Sh\lambda x_2 & C\lambda x_2 & -S\lambda x_2 & -Ch\lambda x_2 & -Sh\lambda x_2 \end{bmatrix}, \boldsymbol{v} = \begin{Bmatrix} A_1 \\ B_1 \\ C_1 \\ D_1 \\ A_2 \\ B_2 \\ C_2 \\ D_2 \\ A_3 \\ B_3 \\ C_3 \\ D_3 \end{Bmatrix}, \boldsymbol{b} = \begin{Bmatrix} 0 \\ 0 \\ 0 \\ 0 \\ \frac{1}{EI\lambda^3} \\ 0 \\ 0 \\ 0 \\ 0 \\ 0 \\ 0 \\ 0 \end{Bmatrix}, \tag{5.24}$$

and

$$\begin{cases} A_{35} = -GEI\lambda S\lambda x_1 - C\lambda x_2 + C\lambda x_1 \\ A_{36} = -GEI\lambda C\lambda x_1 + S\lambda x_2 - S\lambda x_1 \\ A_{37} = GEI\lambda \mathrm{Sh}\lambda x_1 - \mathrm{Ch}\lambda x_2 + \mathrm{Ch}\lambda x_1 \\ A_{38} = GEI\lambda \mathrm{Ch}\lambda x_1 - \mathrm{Sh}\lambda x_2 + \mathrm{Sh}\lambda x_1 \end{cases}, \begin{cases} A_{45} = -GEI\lambda S\lambda x_2 - C\lambda x_2 + C\lambda x_1 \\ A_{46} = -GEI\lambda C\lambda x_2 + S\lambda x_2 - S\lambda x_1 \\ A_{47} = GEI\lambda \mathrm{Sh}\lambda x_2 - \mathrm{Ch}\lambda x_2 + \mathrm{Ch}\lambda x_1 \\ A_{48} = GEI\lambda \mathrm{Ch}\lambda x_2 - \mathrm{Sh}\lambda x_2 + \mathrm{Sh}\lambda x_1 \end{cases}, \tag{5.25}$$

with S, C, Sh, Ch, and *G* representing *sin*, *cos*, *sinh*, *cosh*, and *G*(*s*), respectively.

The displacement at the beam tip is

$$W(L,s) = A_3 sin\lambda L + B_3 cos\lambda L + C_3 sinh\lambda L + D_3 cosh\lambda L \tag{5.26}$$

and the transfer function from tip force to tip displacement is

$$\frac{W(L,s)}{\mathcal{F}(s)} = \boldsymbol{c}_w \mathbf{A}^{-1} \boldsymbol{b} = H(s), \tag{5.27}$$

where $\boldsymbol{c}_w = \begin{bmatrix} 0 & 0 & 0 & 0 & 0 & 0 & 0 & 0 & sin\lambda L & cos\lambda L & sinh\lambda L & cosh\lambda L \end{bmatrix}$. The Frequency Response Function (FRF) is the magnitude of the transfer function (5.27) evaluated at $s = j\omega$, or $|H(j\omega)|$. It is plotted with respect to frequency f, and $\omega = 2\pi f$.

5.1.4 Transfer Function from Tip Force to Shear Force and Moment Transmitted

The shear force that is transmitted to the ground is

$$V(0,s) = EIW'''(x,s)|_{x=0} = EI\lambda^3(-A_1 + C_1), \tag{5.28}$$

and the transfer function from tip force to root shear force is

$$\frac{V(0,s)}{\mathcal{F}(s)} = \boldsymbol{c}_V \mathbf{A}^{-1} \boldsymbol{b} = G_V(s), \tag{5.29}$$

where $\boldsymbol{c}_V = \begin{bmatrix} -EI\lambda^3 & 0 & EI\lambda^3 & 0 & 0 & 0 & 0 & 0 & 0 & 0 & 0 & 0 \end{bmatrix}$.

On the other hand, the moment that is transmitted to the ground is

$$M(0,s) = EIW''(x,s)|_{x=0} = EI\lambda^2(-B_1 + D_1), \tag{5.30}$$

and the transfer function from tip force to root moment is

$$\frac{M(0,s)}{\mathcal{F}(s)} = \boldsymbol{c}_M \mathbf{A}^{-1} \boldsymbol{b} = G'_M(s), \tag{5.31}$$

where $\boldsymbol{c}_M = \begin{bmatrix} 0 & -EI\lambda^2 & 0 & EI\lambda^2 & 0 & 0 & 0 & 0 & 0 & 0 & 0 & 0 \end{bmatrix}$. The previous transfer function is further divided by the length of the cantilever beam so that

$$G_M(s) = G'_M(s)/L \tag{5.32}$$

is dimensionless. Transfer functions (5.29) and (5.32) are also evaluated in the following analysis.

Table 5-1. Baseline Values for Model Parameters

	Property	Value
Middle Layer of F^2MC Tube	E_1	52 GPa
	α	27 °
	E_2	18.7 MPa
	v_{12}	0.45
	v_{23}	0.93
	G_{12}	6.24 MPa
Inner/Outer Layer of F^2MC Tube	E_m	11 MPa
	v_m	0.498
	a_1	0.83 mm
	a_2	0.90 mm
	a_3	0.95 mm
	a_4	1.02 mm
Aluminum Beam	E	70 GPa
	ρ	2700 kg/m3
	C	0.2 N·s/m
	L	310 mm
	b	26 mm
	h	1.6 mm
Fluidic Circuit	ρ_w	1000 kg/m^3
	μ	8.94×10^{-4} Pa·s
	R_n	2000
	R_z	2.5×10^{10} Pa·s/ m^3
	B_{w1}	25 MPa
	B_{w2}	200 MPa
	C_a	1.5×10^{-9} m^3/Pa

Table 5-2. Baseline Values and Variance Ranges for Design Parameters

Parameter	Baseline Value	Range
h_p	4 m	0.4 ~ 8 m
r_p	0.8 mm	0.4 ~ 1.2 mm
x_1 ($x_1 < x_2$)	0	0 ~ 310 mm
x_2	115 mm	0 ~ 310 mm

5.2 Experimental Validation

Tables 1 and 2 show the parameters for a laboratory-scale F^{2}MC-beam system. The F^{2}MC tube properties are for custom-made braided tubing consisting of a composite shell with polyurethane matrix and stainless steel fibers, as shown in Figure 5-3. The volume fraction of fiber in the middle is 26%, from which the lamina properties are calculated from micro-mechanics using the matrix and fiber properties (Vashisth *et al.*, 2013). The beam is aluminum and the working fluid is water. The beam damping coefficient C is 0.2 N·s/m, corresponding to 0.5% damping in the first mode calculated with the half-power approach.

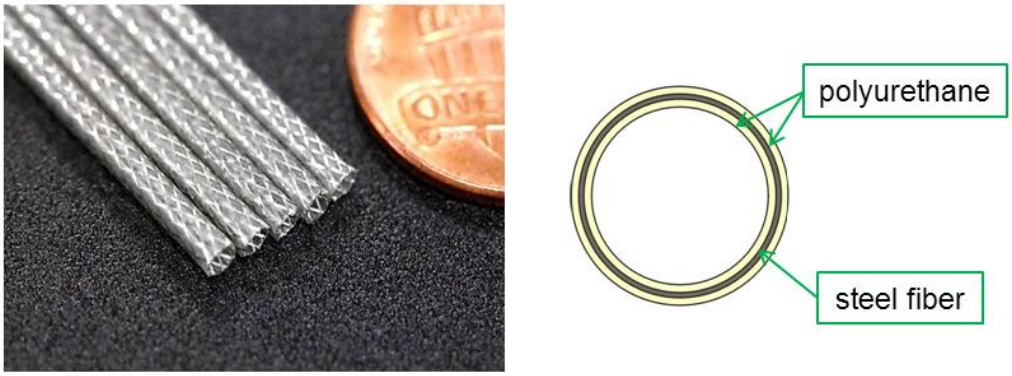

Figure 5-3. FMC tubes used in the experimental study with a US penny for scale (left), and an illustration of the wall cross-section (right).

Figure 5-4 shows the F^{2}MC beam prototype designed and built for the experimental testing. The aluminum beam supports two miniature F^{2}MC tubes, connecting elements, and a fluidic circuit. The F^{2}MC tubes are clamped to the bulkhead fittings and sealed using barbed fittings and pinch clamps. The tubes and fittings are attached to aluminum angles at both ends and the assembly is riveted to the cantilever beam. The F^{2}MC tubes are positioned at $x_1 = 0$ and extend roughly 1/3 of the beam length. Water, tinted red to better detect air bubbles, is filled into the tubes via an inlet valve. Air bubbles make the working fluid more compliant, reducing the fluid

pumping and effectiveness of the absorber. During the filling process, water is constantly injected into the inlet valve, through the plastic tubing, a needle valve, and the inertia track. Once the filling is complete, the inlet valve is closed to block out the filling circuit. The outlet valve is fully open during testing to minimize energy dissipation through the orifice. The inertia track is Teflon PTFE tubing with an inner diameter of 1.6 mm and an outer diameter of 3.2 mm.

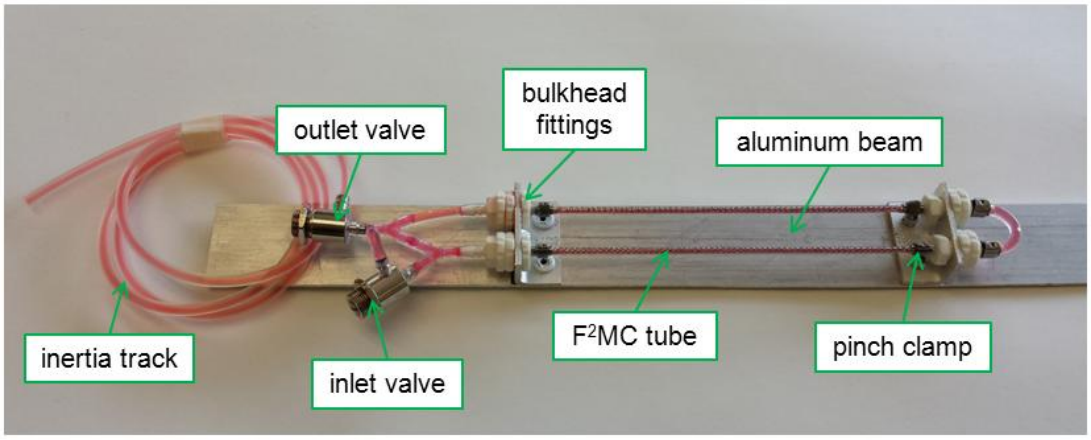

Figure 5-4. Experimental F^{2}MC beam prototype.

The frequency response of the F^{2}MC beam prototype in Figure 5-4 is experimentally acquired using an electro-dynamic shaker and laser vibrometer as shown in Figure 5-5. The cantilever beam is mounted to an aluminum frame at the base and connected to the electro-dynamic shaker through a stinger at the tip. The shaker provides a transverse force excitation, sweeping through a frequency range of interest. The force transducer measures the tip force transmitted through the stinger. The laser Doppler vibrometer measures the tip displacement under the excitation. A LabVIEW-based data acquisition system provided the shaker amplifier input and acquired the laser vibrometer output using A/D and D/A converters and amplifiers. A rotational spring and added mass at the tip are included in the model to account for the stinger rotational constraint and weight. The added mass was measured independently and the rotational

spring constant was calculated based on the static stiffness of the F^2MC beam structure in the experiment. In addition, the masses of fittings were also measured and included in the model.

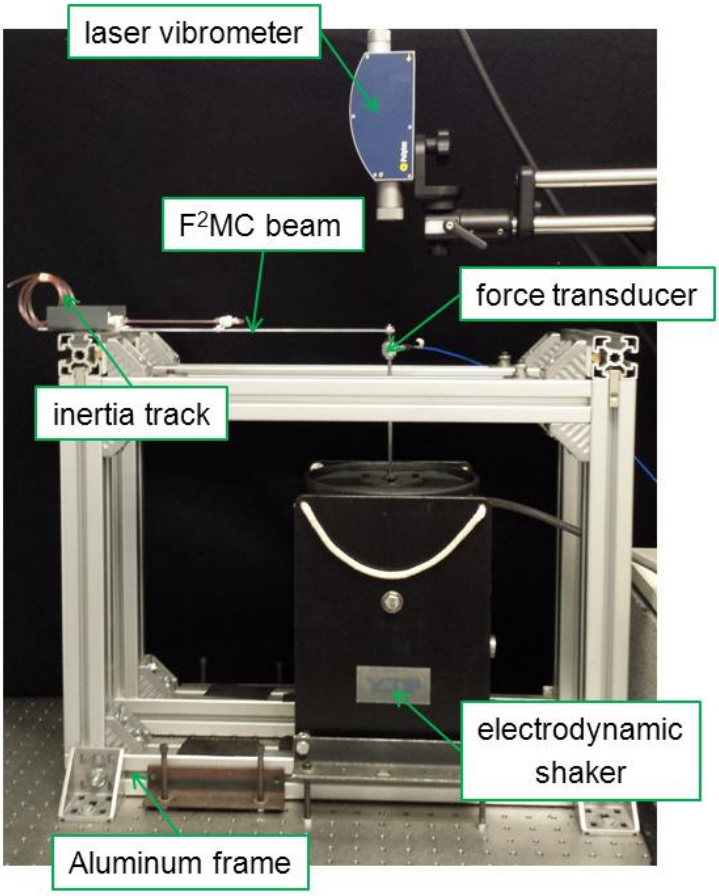

Figure 5-5. Experimental setup for testing of the F^2MC beam system.

All of the parameters for the experiment shown in Tables 1 and 2 are calculated from independent measurements except the fluid bulk modulus and total flow resistance. The fluid bulk modulus is reduced from the handbook value until the static stiffness and first natural frequency match the experiment for the closed valve case. Closing the valve to the inertia track stiffens the beam and the resulting static stiffness and first natural frequency can be experimentally measured and predicted by the model. The total flow resistance is adjusted

upward from the theoretically predicted value until the shape of the theoretically predicted frequency response curve most closely matches the experimental measurements.

Figure 5-6 shows the experimental and analytical frequency response functions for the baseline F^2MC-beam system parameters in Tables 1 and 2. In Figure 5-6(a), the match between theory and experiment is excellent, validating the assumptions and modeling approach. Figure 5-6(b) focuses on the comparison in the first mode with a clearer view. The (ov) results are for a fluid filled system with an open valve between the tube and the inertia track. The curve shows a lightly damped first mode resonance at 15.2 Hz. The (cv) results are when the valve between the tube and the inertia track is closed. The closed valve constrains fluid flow, increasing the pressure in the tube, stiffening the beam, and increasing the first mode frequency to 16.8 Hz. Opening the valve allows the fluid to flow through the inertia track and into the accumulator. The sloshing fluid in the inertia track introduces a valley in the frequency response, associated with fluid inertance and accumulator stiffness. The notch frequency decreases with increasing inertia track length because the fluid inertance is increasing. Figure 5-6 shows that when the inertia track length increases from 3 m to 5 m, the valley frequency drops from 18 Hz to 13 Hz. With an inertia length of 4 m, an attenuation of 35 dB is attained at the first resonance, reducing the tip response of the cantilever beam by more than 98%. The depth of the notch is limited by the energy dissipated by wall friction in the small diameter inertia track. The damping can be reduced by increasing the inertia track diameter but a longer track would be required to generate the optimal inertance (See Equations (5.15-5.16)).

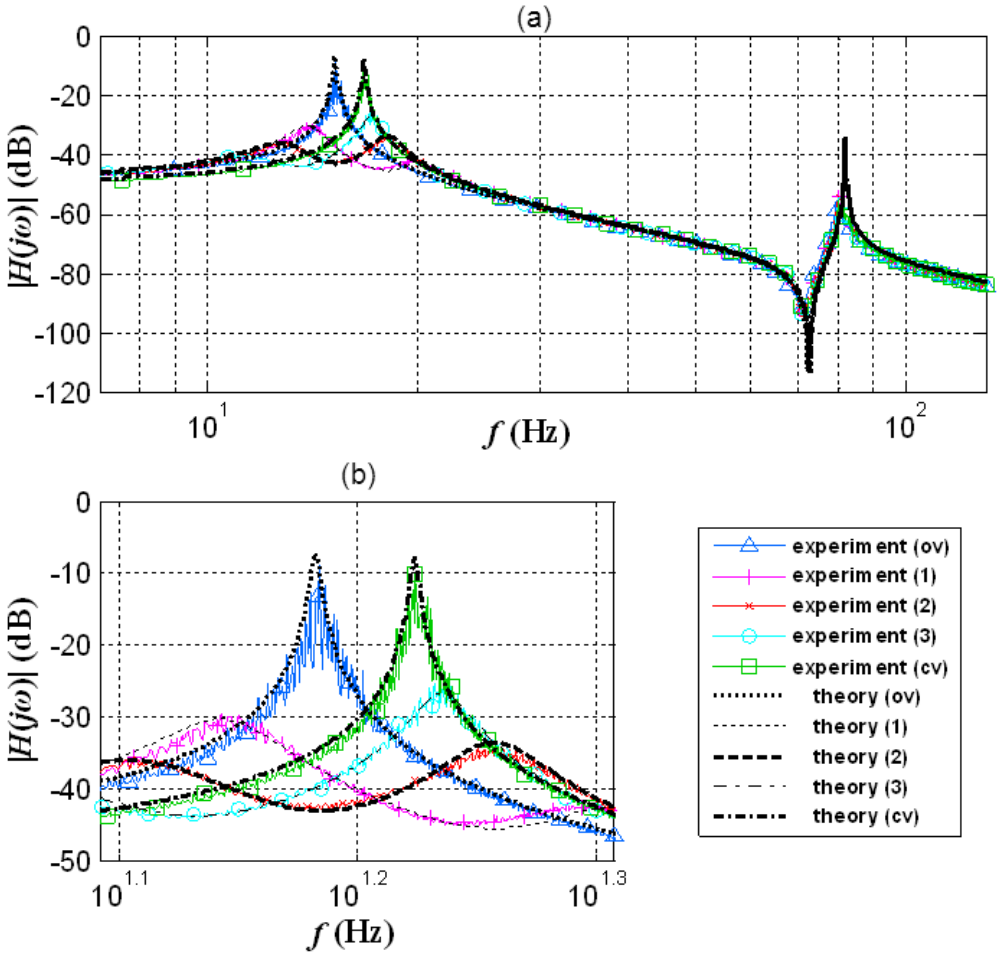

Figure 5-6. Experimental and theoretical frequency response functions for an F^{2}MC beam without fluid (ov) and with fluid and the inertia track closed (cv) or open with different inertia track lengths of (1) h_p = 3 m, (2) h_p = 4 m, and (3) h_p = 5 m for (a) first and second modes; (b) a zoom-in view of first mode. [Units of $H(j\omega)$: m/N]

In order to obtain a good match between theory and experiment, the fluid bulk modulus is greatly reduced from the handbook value of 2 GPa to 25 MPa. Air bubbles in the fluid compresses instead of generating pressure for fluid pumping and the absorber performance suffers. Figure 5-7 shows the effect of fluid bulk modulus on the absorber performance. The bulk moduli in the tube and inertia track vary from 20 MPa to 200 MPa and from 200 MPa to 2 GPa, respectively. The tube with its various fittings and connections is thought to contain more air bubbles than the smooth walled inertia track and hence the difference in bulk moduli. The tube

and inertia track bulk moduli are equally important. When both bulk moduli are increased by 10 times (B_{w1} = 200 MPa, B_{w2} = 2 GPa), a deep valley of -46.3 dB is attained, leading to a magnitude reduction of 39.3 dB (equivalent to 99% reduction in tip response) at the first resonance. Clearly, the elimination of air bubbles through smooth walled design, careful filling, bleeding air from the circuit and possibly pre-pressurizing the circuit to reduce air bubble diameters, can greatly improve the performance of F^{2}MC vibration absorbers.

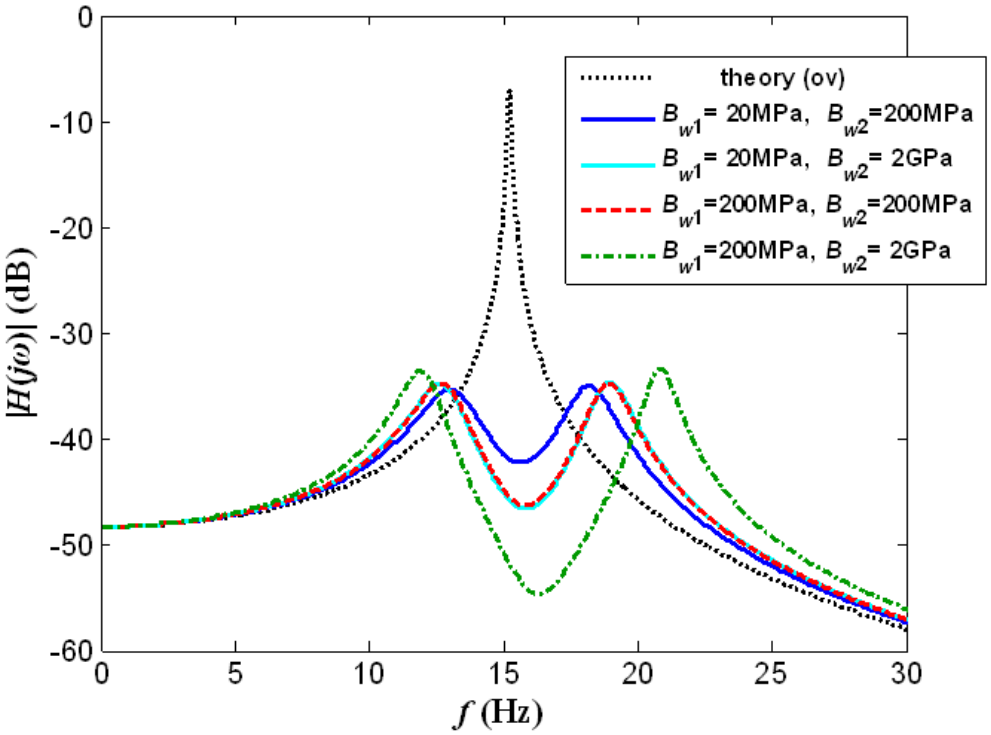

Figure 5-7. Theoretical frequency response function of F^{2}MC-beams with fluid bulk modulus varied from 20 MPa to 2 GPa. [Units of $H(j\omega)$: m/N]

5.3 Parametric Study

A parametric study is undertaken to find the best performing F^{2}MC vibration absorbers and gain insight into their design. In the following design space investigation, four parameters are varied: flow port length, h_p; flow port radius, r_p; and attachment point locations x_1 and x_2. The

baseline and range of parameters for the design space investigation are summarized in Table 2. The handbook value of 2 GPa is used as the fluid bulk modulus in the tube as well as in the inertia track.

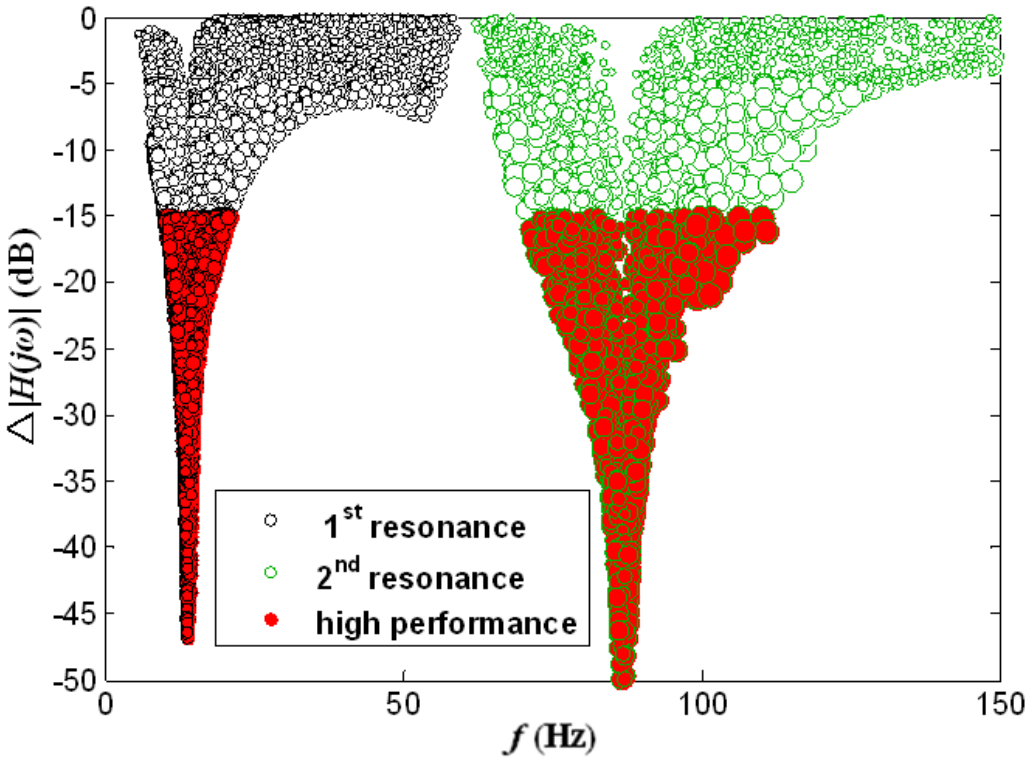

Figure 5-8. Theoretical vibration attenuation for F^{2}MC absorbers with parameters from Tables 1 and 2. Filled circles indicate designs with >15 dB attenuation. [Units of $\Delta H(j\omega)$: m/N]

Figure 5-8 shows the first and second mode attenuations for 400,000 randomly generated cases. Each circle in the graph represents a possible configuration of the F^{2}MC tube with parameters in the ranges from Table 2. The circle size is proportional to the frequency range over which the absorber is effective or the width of the notch. Designs with high attenuation and a wide notch are preferred. The results show that vibration absorption is achievable across a wide frequency range, with the maximum attenuation near the resonant frequencies (*i.e.* 14 Hz, 87 Hz)

of the bare beam. The filled circles are high performance designs that provide vibration attenuations of over 15 dB, equivalent to an 82% reduction in tip response.

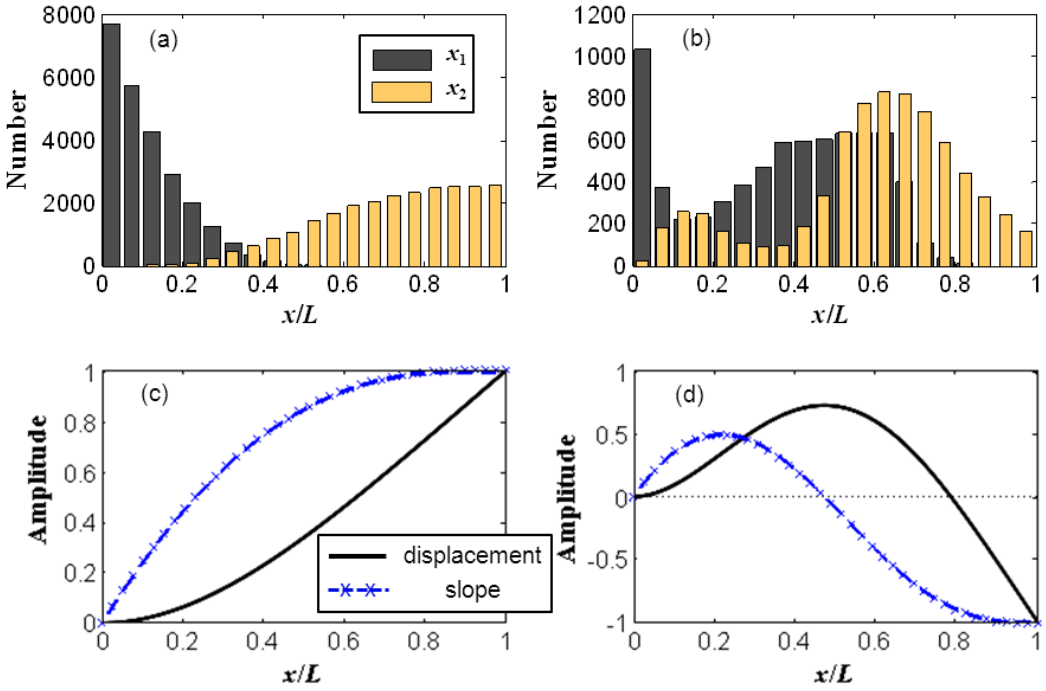

Figure 5-9. F^{2}MC tube attachment point locations with >15 dB first and second mode attenuation: (a) Histogram of left (x_1) and right (x_2) attachment points for first mode; (b) Histogram of left (x_1) and right (x_2) attachment points for second mode; (c) Normalized first mode displacement (solid line) and slope (dashed with x) distributions; (d) Normalized second mode displacement (solid line) and slope (dashed with x) distributions.

The histogram in Figure 5-9(a) shows the bonding location distributions for F^{2}MC beam designs with best first mode attenuation. Maximal reduction is achieved by attaching the F^{2}MC tube at the left end ($x_1/L = 0$) and at $x_2/L \approx 0.8$ because this maximizes the coupling between first mode and the tube strain as indicated by the modal slope difference plotted in Figure 5-9(c). The histogram also shows that attenuation is much more sensitive to x_1 than x_2. As long as the tube attaches near the clamped end, it does not need to extend along the entire length of the beam. The histogram in Figure 5-9(b) shows the attachment point distributions that achieve maximum

reduction at the second resonance have x_1/L = 0 and x_2/L = 0.15 or x_1/L = 0.35 and x_2/L = 0.7, again matching the maximum slope difference regions in the second mode shown in Figure 5-9(d).

Figure 5-10 shows plots of the flow port length, radius, and fluid inertance histograms for maximum absorption in the first (dark/thick bar) and second (light/thin bar) modes. Figures 5-10(a)&(b) show that shorter and larger diameter inertia tracks achieve the best attenuation in the second mode. According to Equation (5.15), this results in a smaller fluid inertance (as shown in Figure 5-10(c)) and matches the absorber and structural natural frequencies.

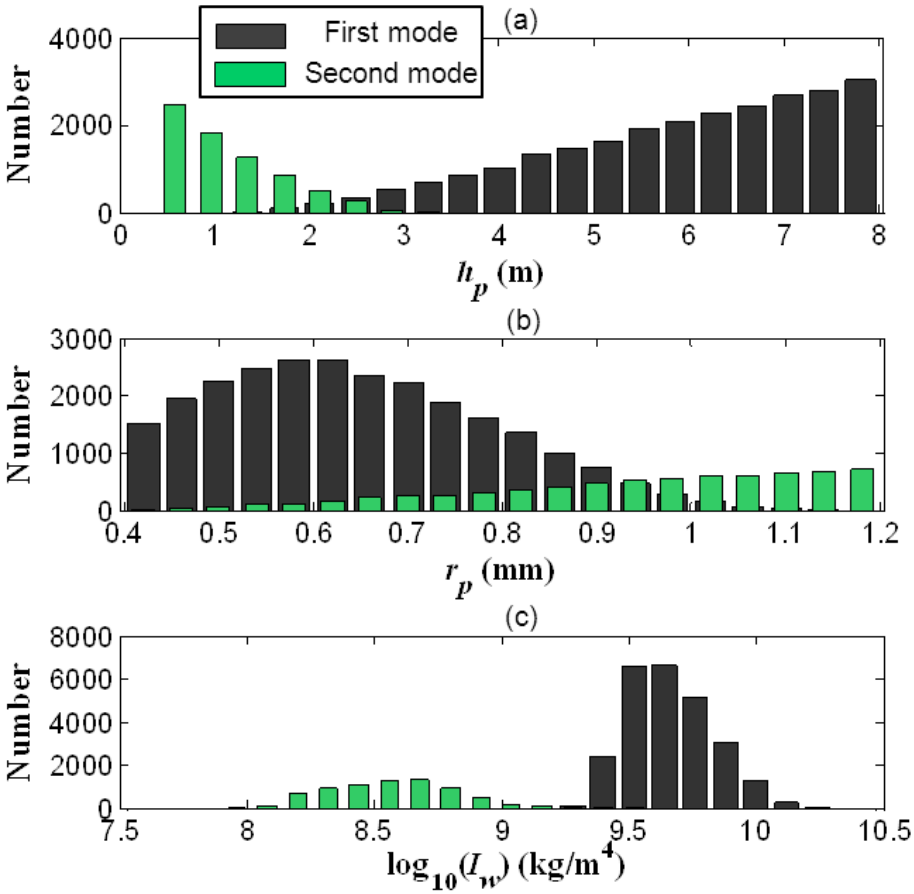

Figure 5-10. Distributions of (a) h_p, (b) r_p, and (c) I_w with >15 dB vibration attenuation in the first (dark/thick bar) and second (light/thin bar) modes.

Figure 5-11 shows two high performance designs that attenuate the responses at the first and second resonances of the bare beam. When an F^{2}MC vibration absorber is attached at x_1 = 0 and x_2 = 150 mm with a 0.5 mm radius and 5.9 m inertia track, a broad and deep notch reduces the response by 49 dB at the first resonance. Attenuation of 82.5 dB at the second natural frequency is achieved with an F^{2}MC vibration absorber attached at x_1 = 90 and x_2 = 240 mm with a 1.1 m long and 0.8 mm radius inertia track.

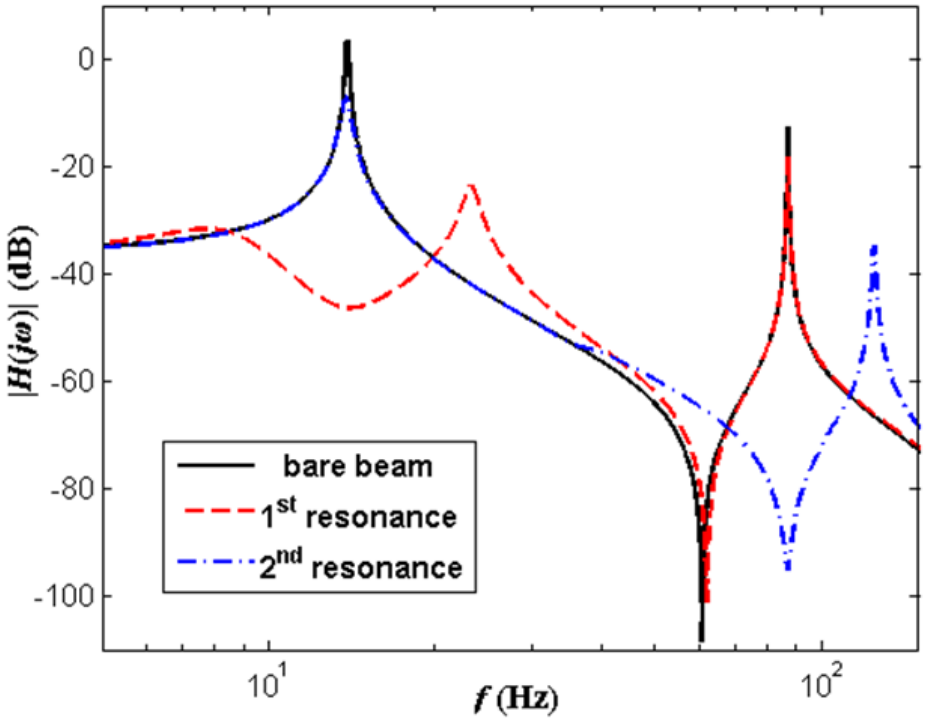

Figure 5-11. Theoretical frequency response functions: Bare beam (solid), F^{2}MC-beam with h_p = 5.9 m, r_p = 0.5 mm, x_1 = 0, x_2 = 150 mm (dashed), and F^{2}MC -beam with h_p = 1.1 m, r_p = 0.8 mm, x_1 = 90 mm, x_2 = 240 mm (dash-dotted). [Units of $H(j\omega)$: m/N]

5.4 F²MC Vibration Isolator

Following the same approach as the absorber, the F²MC vibration isolator can also be designed and optimized by tailoring the tube attachment locations, inertia track length, and inertia track radius to minimize the force transmission.

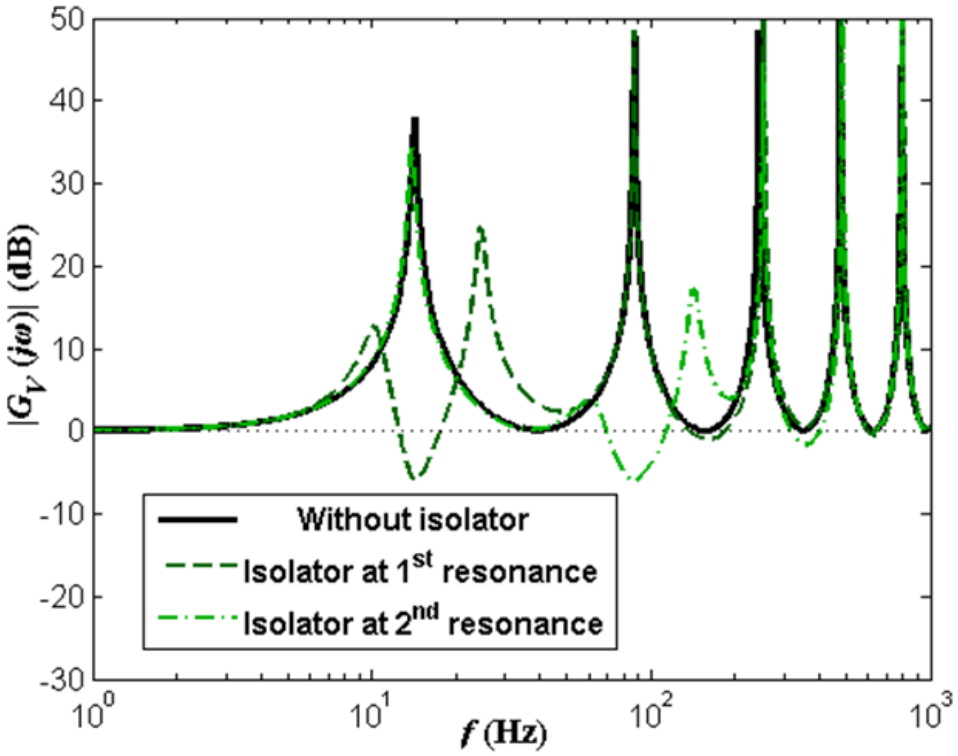

Figure 5-12. Theoretical frequency response functions of shear force: Bare beam (solid), F²MC-beam with h_p = 7.9 m, r_p = 0.8 mm, x_1 = 0, x_2 = 150 mm (dashed), and F²MC -beam with h_p = 0.45 m, r_p = 1 mm, x_1 = 90 mm, x_2 = 240 mm (dash-dotted). [$G_V(j\omega)$ is dimensionless]

Figure 5-12, for instance, shows two high performance designs that reduces the shear force transmitted to the base at the first and second resonances of the bare beam. According to Equation (5.29), the frequency responses in Figure 5-12 evaluates the magnitude of shear force as compared with the tip load. The solid line is for the bear beam and its magnitude is always greater than zero, which means a cantilever beam naturally amplifies the shear force transmitted

to the ground. At the first resonance at 14 Hz, the bare beam achieves a magnitude of 37.4 dB, meaning the shear force is about 74 times of the tip force. With an F^{2}MC isolator attached at x_1 = 0 and x_2 = 150 mm with a 0.8 mm radius and 7.9 m inertia track, the shear force is reduced to 50% of the tip force (equivalent to 5.9 dB reduction). That yields an overall shear force attenuation of 99.3% as compared with the bare beam. Attenuation of 54.4 dB at the second natural frequency is achieved with an F^{2}MC vibration isolator attached at x_1 = 90 and x_2 = 240 mm with a 450 mm long and 1 mm radius inertia track.

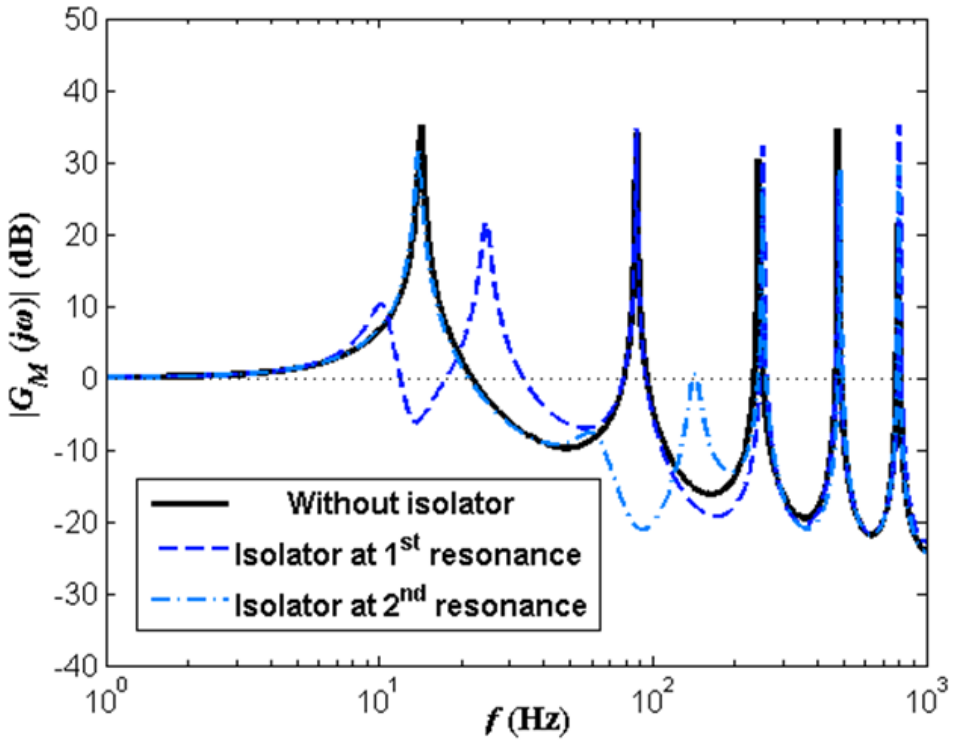

Figure 5-13. Theoretical frequency response functions of moment: Bare beam (solid), F^{2}MC-beam with h_p = 7.9 m, r_p = 0.8 mm, x_1 = 0, x_2 = 150 mm (dashed), and F^{2}MC -beam with h_p = 0.45 m, r_p = 1 mm, x_1 = 90 mm, x_2 = 240 mm (dash-dotted). [$G_M(j\omega)$ is dimensionless]

Figure 5-13 are the frequency response functions of moment transmitted to ground with the same F^{2}MC tube designs as in Figure 5-12. Magnitude reductions of 40.8 dB and 55.3 dB are achieved targeting the first and the second modes, respective.

Chapter 6

Conclusions and Future Work

6.1 Conclusions

In this research, the modeling, analysis, design, and experiment of integrated fluidic flexible matrix composite structures is presented. It explores the potential of achieving tunable structural stiffness, actuation, damping, and absorption properties utilizing F^2MC tubes. Firstly, an analytical model of a composite structure consisting of an F^2MC tube embedded in epoxy is used to study the impact of confining structural media on the ability of F^2MC tubes to pump fluid and change stiffness. The surrounding stiff epoxy reduces the performance relative to an isolated F^2MC tube but this can be minimized by tailoring the tube wall thickness and fiber angle. A pumping factor of over 250 can be achieved with a thick shell wall and a near-axial fiber orientation. With a moderately thick wall and low fiber angle the closed valve axial stiffness can be increased by a factor of 2.2 relative to the open valve stiffness. The maximum pumping factor and modulus ratio, however, are 80% and 2.6% of the F^2MC tube without the surrounding epoxy.

This work then models and analyzes the free strain and blocked force of F^2MC actuators embedded in structural media. The analytical results show that actuation performance is generally reduced compared to that of an isolated F^2MC tube due to the radial and longitudinal constraints imposed by the surrounding structural medium. Free strain is generally two orders of magnitude smaller for an F^2MC tube in structural media, requiring higher actuation pressures for bi-layer F^2MC structures. The blocked force of F^2MC embedded in structural media is roughly an order of magnitude smaller than that of an isolated F^2MC tube. The analysis shows a great degree of tailorability in actuation properties, based on the F^2MC tube design that can minimize these

differences. Higher actuation performance is achieved, for example, with a thick walled F^2MC tube, as opposed to the thin wall that maximizes performance in an isolated F^2MC tube. Experiments were also carried out to validate the theoretical models. Experimental and analytical results achieved a reasonably good match for the free strain. The biggest discrepancies happen for F^2MC tubes with fiber angles smaller than 25 °. The main cause of the disagreement is believed to be shear lag and end effects which are not included in the analytical models.

The great fluid pumping ability of F^2MC tubes reveal their potential for vibration reduction applications. For example, attaching a multi-tube F^2MC patch with an orifice to a cantilever beam can increase the damping in a target mode. The F^2MC tubes are offset from the beam centroid so that bending vibration causes tube strain and fluid pumping through an energy-dissipating orifice. The pressure generated in the tube by the orifice then applies moments at the tube attachment points to dampen the beam vibration. Optimal design of the F^2MC tube for a given cantilever requires an optimized orifice flow coefficient, a high effective fluid bulk modulus, and attachment points that maximize modal slope difference. Tuning the fluid bulk modulus and orifice resistance in the model produces results that closely match the experimentally measured damping ratio of 5.3%. This corresponds to a 92% reduction in the tip response of the cantilever beam. Using a patch consisting of two F^2MC tubes, the model predicts damping ratios of up to 32% and 16% in the first and second modes, respectively. Multiple tubes targeted at different modes can also be provided for optimal, multi-modal damping.

Finally, the research shows that F^2MC tubes with resonant fluidic circuits can absorb and/or isolate vibration at a specific frequency when bonded to flexible structures. The transverse structural vibration stretches the F^2MC tubes and the anisotropic fibers in the composite tube amplify the axial strain to produce large internal volume change. The volume change forces fluid through a flow port and into an external accumulator. The fluid inertance in the inertia track and the stiffness of the accumulator are analogous to the vibration absorbing mass and stiffness in a

conventional tuned vibration absorber. Tuning the fluid bulk modulus and total flow resistance in an F^2MC-integrated cantilever beam model produces results that accurately match the collocated tip frequency response function that is measured on a laboratory-scale F^2MC beam structure with miniature tubes and fluidic components. The resonant peaks become absorber notches in the frequency response function if the inertia track length and diameter are properly tuned. The experimental and theoretical results match well, predicting a magnitude reduction of 35 dB at the first resonance using an F^2MC absorber. Based on the experimentally validated model, analysis results show that the cantilever beam vibration can be reduced by more than 99% with optimally designed tube attachment points and flow port geometry. The model also predicts 99.3% reduction of transmitted forces and moments from the tip force. For a given fluidic circuit design, however, the absorber, shear isolation, and moment isolation frequencies are different.

6.2 Future Work

6.2.1 Applications of F^2MC Absorber/Isolator and Damper

The F^2MC damper, absorber, and isolator can be applied in many fields including helicopter tailbooms, aircraft wings, and actuator arms in hard disk drive (HDD). The research findings in this work can be used to guide such an implementation. These structures have more complex geometry and mass distribution and these factors have to be included in the model. If multi-modal vibration treatment is desired, then multiple F^2MC tubes are needed. This will require a redesign of the layout of the tubes and the fluidic circuits, and the consideration of the interactions between the tubes. Li and Wang (2013), for instance, demonstrate a synthesis procedure to design multicellular F^2MC structures for specified poles and zeros in the frequency response. Besides, with multiple fluidic circuits, semi-active control technique (Cunefare *et al.*,

2000; Jalili, 2002) is recommended to regulate the on/off states of the valves and improve the vibration attenuation effects with low cost. From the practical perspective, there are also challenging things to consider as well such as limited space available, limit on the added weight/cost, and the bonding/ or attaching techniques. In addition, the F^2MC absorber, isolator and damper can be combined for use to achieve more comprehensive vibration attenuation. For example, a damped F^2MC absorber can form by integrating an orifice, an inertia track, and an external accumulator into F^2MC beams, which helps to achieve broadband damping compared with the damper alone. If both an F^2MC absorber and isolator are implemented, displacement response as well as force transmission can be minimized. However, since the absorption frequency and isolation frequency differ, more investigation is needed to achieve an optimal design.

In addition, air bubbles in the fluid can significantly reduce the amount of fluid pumping and furthermore fluidic damping. This is one of the challenges for either small or large scale applications. Improved filling process and even air bubble monitoring system are recommended. For small scale application in particular, the hardware like fittings should be minimized simultaneously in order to accommodate more tubes. On the other hand, strong and well-sealed fittings are in demand when it comes to large scale applications. There will be large force and pressure generated from the fluid volume change and the hardware should meet those requirements.

6.2.2 High Frequency Applications, Noise Control

F^2MC integrated plates/panels can also be used to reduce noise transmission by utilizing the fluid pumping. This is especially promising for the aerospace industry, where both high material stiffness/and strength, and light weight are desired and fluidic composites can satisfy

these requirements. One example is the rotorcraft transmission housings. Large acoustic noise is generated from the rotor transmission and is transmitted through the housing. Increasing the mass of the housing tends to reduce the noise transmitted, but meanwhile it reduces the rotorcraft payload capability. Composites with F^2MC tubes integrated have the potential to provide with the high stiffness and strength and also achieve noise attenuation by properly directing the induced fluid flow inside the plates/panels, similar to the F^2MC-beam structures presented in this work. An optimal design will involve the consideration of the plate modes and frequencies, the fluidic circuit design (may require built-in manifold), the choosing of composite material systems, and drilling/sealing techniques. Furthermore, in the high frequency domain, the material properties of the composites are very likely to be rate and temperature dependent. Therefore, dynamic mechanical analysis (DMA) testing has to be performed to obtain the corresponding storage and loss moduli data at the lamina level. The effects of high frequency excitation on the fluid performance should also be addressed.

Appendices

Appendix A

The Derivation of the Magic Number $\alpha = 55^{\circ}$, a Kinematic Approach

The work in this dissertation has demonstrated the behavior of the F^2MC actuator with internal pressurization. The fiber angle α basically determines whether the actuator will contract or elongate. It has been observed that when the fiber angle $\alpha = 55^{\circ}$, the F^2MC actuator has zero axial strain with response to pressure. The physical meaning for that is the actuator achieves the maximum internal volume in that case and it cannot inflate more even with high pressure. This appendix is intended to derive that magic number with a kinematic approach. The following assumptions are made:

1) The FMC tube is thin-walled;

2) The tube is assumed to be infinitely long, or the length over radius ratio is very large, so that the end effects are neglected and the tube is perfectly cylindrical in shape;

3) The fibers in the FMC tube are inextensible.

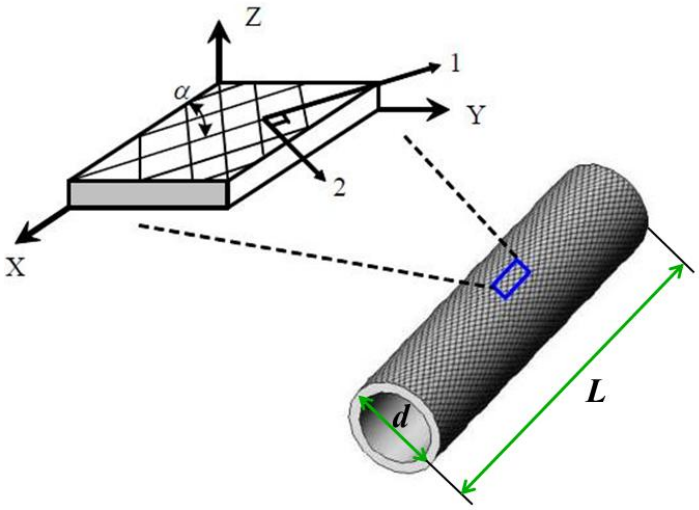

Figure A1-1. The schematic of fiber orientation in an FMC tube.

For the FMC tube in Figure A1-1, the fiber winding angle is α. We assume the total length of one single strand of fibers is L_0. The fibers are wound a total of n turns in the circumferential direction. If one strand of fibers is peeled off the tube as the FMC tube rolls down a flat surface, it will form the right triangle ΔABC, as shown in Figure A1-2.

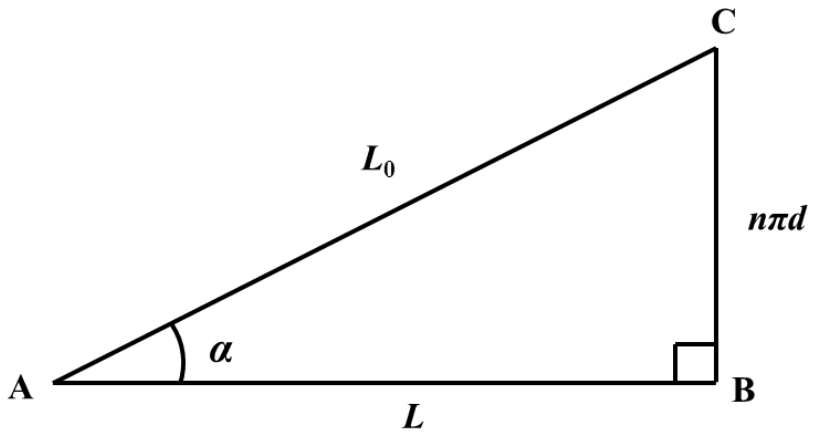

Figure A1-2. The geometric relationships between length of FMC tube, length of fibers, and the circumference of the cylindrical tube.

The hypotenuse $\overline{\mathrm{AC}}$ is the total length of the fibers L_0. The angle ∠CAB is same as the winding angle α. The length of the tube equals the bottom side of the triangle $\overline{\mathrm{AB}}$

$$L = L_0 \cos\alpha \tag{A1.1}$$

The diameter of the tube d is calculated from

$$n\pi d = L_0 sin\alpha \tag{A1.2}$$

Therefore,

$$d = \frac{L_0 sin\alpha}{n\pi} \tag{A1.3}$$

The volume of the tube is calculated as

$$V = \frac{1}{4}\pi d^2 L \tag{A1.4}$$

Substituting Equations (A1.1) and (A1.3) to the above equation yields

$$V = \frac{L_0^3}{4\pi n^2} sin^2\alpha cos\alpha \tag{A1.5}$$

The FMC tube volume V is a function of the fiber angle α. In order to find the local maximums for V, first let the derivative of V with respect to winding angle α to be zero. That is

$$\frac{dV}{d\alpha} = \frac{d}{d\alpha}\left(\frac{L_0^3}{4\pi n^2} sin^2\alpha cos\alpha\right) = \frac{L_0^3}{4\pi n^2} sin\alpha(2cos^2\alpha - sin^2\alpha) = 0 \tag{A1.6}$$

The winding angle α is the orientation between the fiber and the longitudinal axis. Therefore, it is always greater than zero and smaller than 90 º. The solution to Equation (A1.6) is

$$2cos^2\alpha - sin^2\alpha = 0 \tag{A1.7}$$

Combining with the Pythagorean identity

$$sin^2\alpha + cos^2\alpha = 1 \tag{A1.8}$$

and solving for $sin^2\alpha$, we have

$$sin^2\alpha = \frac{2}{3} \tag{A1.9}$$

Therefore, one critical point for the volume function V is

$$\alpha_c = 54.7356103\cdots^\circ \approx 55^\circ \tag{A1.10}$$

The second derivative of function V is

$$\frac{d^2V}{d^2\alpha} = \frac{L_0^3}{4\pi n^2} cos\alpha(2cos^2\alpha - 7sin^2\alpha) \quad \text{(A1.11)}$$

Evaluating at the critical point $\alpha_c = 55°$,

$$\frac{d^2V}{d^2\alpha}|_{\alpha=55°} = \frac{L_0^3}{4\pi n^2} \times (-2.3094) < 0 \quad \text{(A1.12)}$$

Besides, $\alpha_c = 55°$ is the only solution of Equation (A1.6), so it is not only a local maximum but also the global maximum of the tube volume function.

Therefore, at the magic number α = 55 º, the FMC tube has the maximum internal volume. This is the reason why the following phenomena were observed in Chapters 2 & 3.

1) Free Strain = 0: The F^{2}MC actuator already has the maximal volume at 55 º. Further increment in pressure cannot inflate the tube/change tube volume any more.

2) Block Factor = 0: The tube has no free strain/stroke with internal pressurization. As a result, the blocking force is zero.

3) Pumping Factor P = 0: α = 55 ºresults in a maximum for tube volume. Therefore, a small increment in axial strain leads to no change in the internal volume.

4) Modulus Ratio R = 1: Because of the zero fluid pumping, there will be no extra pressure/ or confining force acting on the interior wall. The closed valve stiffness of the F^{2}MC tube is same as the open valve.

However, it should be noted that the tube wall thickness, wall compliance, and fiber extensibility are included in the models in Chapters 2&3. The derivation in this appendix is an approximate estimation. The actual "magic number" in the theoretical predictions may not be exactly 55 º. However, it is very close in many cases.

Appendix B

Refined Modeling for Experiment

A rotational spring and added mass at the tip are included in the model to account for the stinger rotational constraint and weight because of instrumentation. The added mass was measured independently and the rotational spring constant was calculated based on the static stiffness of the F^{2}MC beam structure in the experiment. In addition, the masses of fittings were also measured and included in the model.

1) Add end mass to count the added weight of shaker stinger and load cell;

2) Add lumped masses at bonding locations to represent the weights of fittings and aluminum angles;

3) Add torsional spring to model the extra constant imposed by the shaker stinger to prevent beam tip from rotating freely.

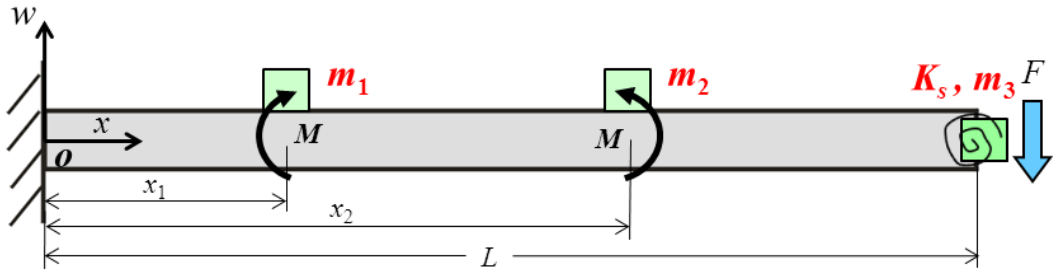

Figure A2-1. The schematic of F^{2}MC beam structure with added torsional spring and lumped masses at bonding locations and constrained beam tip.

By measurement: m_1 = 4 g, m_2 = 8.5 g, m_3 = 14.5 g;

The aluminum beam is 310 mm long, 26 mm wide, and 1.6 mm thick. The weight of the beam is 34.8 g. The two F^{2}MC tubes are filled with water and they have a diameter of 2 mm and a length of 115 mm. The weight of the tubes are 0.7 g in total. So the F^{2}MC tubes weighs about 2% of the beam weight. The fitting weight, which is the sum of m_1 and m_2, is 12.5 g and it is approximately 36% of the beam weight.

The torsional stiffness constant K_s needs to be calibrated based on the static stiffness of the F^{2}MC beam structure from the FRF (at zero frequency).

This appendix will explain in details the change in the modeling approach. Take the damping modeling as an example, there are mainly four boundary conditions (marked with *) changed because of this. The updated boundary conditions for this particular case are the following:

(1) The left end ($x = 0$) of the beam is clamped, so

$$W_1(0,s) = 0, \text{ and} \tag{A2.1}$$

$$W_1'(0,s) = 0. \tag{A2.2}$$

(2) A moment and force balance at $x = x_1$ yields

$$EI[W_2''(x_1,s) - W_1''(x_1,s)] = \mathcal{M}(s), \text{ and} \tag{A2.3}$$

$$EIW_1'''(x_1,s) - EIW_2'''(x_1,s) = m_1 s^2 W_1(x_1,s), \tag{*A2.4}$$

where $\mathcal{M}(\mathrm{s}) = \mathcal{L}\{M(t)\}$. Continuity requires

$$W_1(x_1,s) = W_2(x_1,s), \text{ and} \tag{A2.5}$$

$$W_1'(x_1,s) = W_2'(x_1,s). \tag{A2.6}$$

(3) Similarly, a moment and force balance at $x = x_2$ gives

$$EI[W_2''(x_2,s) - W_3''(x_2,s)] = \mathcal{M}(s), \text{ and} \tag{A2.7}$$

$$EIW_2'''(x_2,s) - EIW_3'''(x_2,s) = m_2 s^2 W_2(x_2,s), \tag{*A2.8}$$

and the continuity conditions are

$$W_2(x_2,s) = W_3(x_2,s), \text{ and} \tag{A2.9}$$

$$W_2'(x_2, s) = W_3'(x_2, s). \tag{A2.10}$$

(4) Shear and moment balances at the tip ($x = L$) yield

$$EIW_3'''(L, s) - m_3 s^2 W_3(L, s) = \mathcal{F}(s), \text{ and} \tag{*A2.11}$$

$$EIW_3''(L, s) = -K_s W_3'(L, s). \tag{*A2.12}$$

where $\mathcal{F}(s) = \mathcal{L}\{F(t)\}$.

Due to changes in the boundary conditions, Equations (4.61)-(4.63) will be updated as well. Substitution of Equations (4.6) and (4.59) into the boundary conditions (A2.1)-(A2.12) yields

$$\mathbf{A}\boldsymbol{v} = \boldsymbol{b}\mathcal{F}(s), \tag{A2.13}$$

where

$$\boldsymbol{A} = \begin{bmatrix}
0 & 1 & 0 & 1 & 0 & 0 & 0 & 0 & 0 & 0 & 0 & 0 \\
1 & 0 & 1 & 0 & 0 & 0 & 0 & 0 & 0 & 0 & 0 & 0 \\
GEI\lambda S\lambda x_1 & GEI\lambda C\lambda x_1 & -GEI\lambda \mathrm{Sh}\lambda x_1 & -GEI\lambda \mathrm{Ch}\lambda x_1 & A_{35} & A_{36} & A_{37} & A_{38} & 0 & 0 & 0 & 0 \\
0 & 0 & 0 & 0 & A_{45} & A_{46} & A_{47} & A_{48} & GEI\lambda S\lambda x_2 & GEI\lambda C\lambda x_2 & -GEI\lambda \mathrm{Sh}\lambda x_2 & -GEI\lambda \mathrm{Ch}\lambda x_2 \\
0 & 0 & 0 & 0 & 0 & 0 & 0 & 0 & A_{59} & A_{5a} & A_{5b} & A_{5c} \\
0 & 0 & 0 & 0 & 0 & 0 & 0 & 0 & A_{69} & A_{6a} & A_{6b} & A_{6c} \\
S\lambda x_1 & C\lambda x_1 & \mathrm{Sh}\lambda x_1 & \mathrm{Ch}\lambda x_1 & -S\lambda x_1 & -C\lambda x_1 & -\mathrm{Sh}\lambda x_1 & -\mathrm{Ch}\lambda x_1 & 0 & 0 & 0 & 0 \\
C\lambda x_1 & -S\lambda x_1 & \mathrm{Ch}\lambda x_1 & \mathrm{Sh}\lambda x_1 & -C\lambda x_1 & S\lambda x_1 & -\mathrm{Ch}\lambda x_1 & -\mathrm{Sh}\lambda x_1 & 0 & 0 & 0 & 0 \\
A_{91} & A_{92} & A_{93} & A_{94} & -EI\lambda^3 C\lambda x_1 & EI\lambda^3 S\lambda x_1 & EI\lambda^3 \mathrm{Ch}\lambda x_1 & EI\lambda^3 \mathrm{Sh}\lambda x_1 & 0 & 0 & 0 & 0 \\
0 & 0 & 0 & 0 & S\lambda x_2 & C\lambda x_2 & \mathrm{Sh}\lambda x_2 & \mathrm{Ch}\lambda x_2 & -S\lambda x_2 & -C\lambda x_2 & -\mathrm{Sh}\lambda x_2 & -\mathrm{Ch}\lambda x_2 \\
0 & 0 & 0 & 0 & C\lambda x_2 & -S\lambda x_2 & \mathrm{Ch}\lambda x_2 & \mathrm{Sh}\lambda x_2 & -C\lambda x_2 & S\lambda x_2 & -\mathrm{Ch}\lambda x_2 & -\mathrm{Sh}\lambda x_2 \\
0 & 0 & 0 & 0 & A_{c5} & A_{c6} & A_{c7} & A_{c8} & -EI\lambda^3 C\lambda x_2 & EI\lambda^3 S\lambda x_2 & EI\lambda^3 \mathrm{Ch}\lambda x_2 & EI\lambda^3 \mathrm{Sh}\lambda x_2
\end{bmatrix}, \boldsymbol{v} = \begin{Bmatrix} A_1 \\ B_1 \\ C_1 \\ D_1 \\ A_2 \\ B_2 \\ C_2 \\ D_2 \\ A_3 \\ B_3 \\ C_3 \\ D_3 \end{Bmatrix}, \boldsymbol{b} = \begin{Bmatrix} 0 \\ 0 \\ 0 \\ 0 \\ 1 \\ 0 \\ 0 \\ 0 \\ 0 \\ 0 \\ 0 \\ 0 \end{Bmatrix}, \tag{A2.14}$$

and

$$\begin{cases} A_{35} = -GEI\lambda S\lambda x_1 - C\lambda x_2 + C\lambda x_1 \\ A_{36} = -GEI\lambda C\lambda x_1 + S\lambda x_2 - S\lambda x_1 \\ A_{37} = GEI\lambda \mathrm{Sh}\lambda x_1 - \mathrm{Ch}\lambda x_2 + \mathrm{Ch}\lambda x_1 \\ A_{38} = GEI\lambda \mathrm{Ch}\lambda x_1 - \mathrm{Sh}\lambda x_2 + \mathrm{Sh}\lambda x_1 \end{cases}, \begin{cases} A_{45} = -GEI\lambda S\lambda x_2 - C\lambda x_2 + C\lambda x_1 \\ A_{46} = -GEI\lambda C\lambda x_2 + S\lambda x_2 - S\lambda x_1 \\ A_{47} = GEI\lambda \mathrm{Sh}\lambda x_2 - \mathrm{Ch}\lambda x_2 + \mathrm{Ch}\lambda x_1 \\ A_{48} = GEI\lambda \mathrm{Ch}\lambda x_2 - \mathrm{Sh}\lambda x_2 + \mathrm{Sh}\lambda x_1 \end{cases}, \tag{A2.15}$$

and

$$\begin{cases} A_{59} = -EI\lambda^3 C\lambda L - m_3 s^2 S\lambda L \\ A_{5a} = EI\lambda^3 S\lambda L - m_3 s^2 C\lambda L \\ A_{5b} = EI\lambda^3 \mathrm{Ch}\lambda L - m_3 s^2 \mathrm{Sh}\lambda L \\ A_{5c} = EI\lambda^3 \mathrm{Sh}\lambda L - m_3 s^2 \mathrm{Ch}\lambda L \end{cases}, \begin{cases} A_{69} = -\lambda S\lambda L + K_s C\lambda L \\ A_{6a} = -\lambda C\lambda L - K_s S\lambda L \\ A_{6b} = \lambda \mathrm{Sh}\lambda L + K_s \mathrm{Ch}\lambda L \\ A_{6c} = \lambda \mathrm{Ch}\lambda L + K_s \mathrm{Sh}\lambda L \end{cases}, \tag{A2.16}$$

and

$$\begin{cases} A_{91} = & EI\lambda^3 \mathrm{C}\lambda x_1 + m_1 s^2 \mathrm{S}\lambda x_1 \\ A_{92} = & -EI\lambda^3 \mathrm{S}\lambda x_1 + m_1 s^2 \mathrm{C}\lambda x_1 \\ A_{93} = & -EI\lambda^3 \mathrm{Ch}\lambda x_1 + m_1 s^2 \mathrm{Sh}\lambda x_1 \\ A_{94} = & -EI\lambda^3 \mathrm{Sh}\lambda x_1 + m_1 s^2 \mathrm{Ch}\lambda x_1 \end{cases}, \begin{cases} A_{c5} = & EI\lambda^3 \mathrm{C}\lambda x_2 + m_2 s^2 \mathrm{S}\lambda x_2 \\ A_{c6} = & -EI\lambda^3 \mathrm{S}\lambda x_2 + m_2 s^2 \mathrm{C}\lambda x_2 \\ A_{c7} = & -EI\lambda^3 \mathrm{Ch}\lambda x_2 + m_2 s^2 \mathrm{Sh}\lambda x_2 \\ A_{c8} = & -EI\lambda^3 \mathrm{Sh}\lambda x_2 + m_2 s^2 \mathrm{Ch}\lambda x_2 \end{cases}. \quad \text{(A2.17)}$$

with S, C, Sh, Ch, and *G* representing *sin*, *cos*, *sinh*, *cosh*, and *G*(*s*), respectively.

Bibliography

Allemang, R. J., 1999. "Vibrations: experimental modal analysis," *Course Notes (UC-SDRL-CN-20-263-663/664)*, Structural Dynamics Research Laboratory, University of Cincinnati, Cincinnati. Available from: http://www.sdrl.uc.edu/academic-course-info/.

Avitabile, P., 2001. "Experimental modal analysis," *Sound and Vibration*, *35*(1), 20-31.

Bae, J. S., Kwak, M. K., and Inman, D. J., 2005. "Vibration suppression of a cantilever beam using eddy current damper," *Journal of Sound and Vibration*, 284, 805-824.

Bailey, T., and Hubbard, J. E., 1985. "Distributed piezoelectric-polymer active vibration control of a cantilever beam," *Journal of Guidance, Control and Dynamics*, 8, 605-611.

Baz, A., and Ro, J., 1994. "Performance characteristics of active constrained layer damping," *Shock and Vibration*, 2(1): 33-42.

Beard, A. M., Schubert, D. W., and von Flotow, A. H, 1994. "Practical product implementation of an active/passive vibration isolation system," In *Society of Photo-Optical Instrumentation Engineers (SPIE) Conference Series* (Vol. 2264, pp. 38-49).

Boresi, A. P. and Schmidt, R. J., 2003. "The thick-wall cylinder," *Advanced Mechanics of Materials*. Ch. 11, 6th edition, John Wiley & Sons Inc., New York.

Cafeo, J. A., Trethewey, M. W., and Sonuner, H. J., 1992. "University," *International Journal of Analytical and Experimental Modal Analysis, 7*(4), 255-269.

Caldwell, D., Medrano-Cerda, G. and Goodwin, M., 1995. "Control of pneumatic muscle actuators," *Control Systems, IEEE, 15*(1), 40-48.

Chou, C-P. and Hannaford, B., 1994. "Static and dynamic characteristics of McKibben pneumatic artificial muscles," *Proceedings of ICRA*, vol. 1, pp. 281-286.

Chou, C. P., and Hannaford, B., 1996. "Measurement and modeling of McKibben pneumatic artificial muscles," *Robotics and Automation, IEEE Transactions on*, *12*(1), 90-102.

Crede, C. E., and Ruzicka, J. E., 1996. "Theory of vibration isolation," in *Shock and Vibration Handbook*, C. M. Harris, Ed. New York: Mcgraw-Hill, ch. 30.

Cunefare, K. A., De Rosa, S., Sadegh, N., and Larson, G., 2000. "State-switched absorber for semi-active structural control," *Journal of Intelligent Material Systems and Structures, 11*(4), 300-310.

Daerden, F. and Lefeber, D., 2002. "Pneumatic artificial muscles: actuators for robotics and

automation," *European Journal of Mechanical and Environmental Engineering*, 47, pp. 10-21.

Davis, C. L., Lesieutre, G. A., and Dosch, J., 1997. "A tunable electrically shunted piezoceramic vibration absorber," In *SPIE Symposium on Smart Structures and Materials* (pp. 51-59).

Davis, S., Tsagarakis, N., Canderle, J., and Caldwell, D. G., 2003. "Enhanced modelling and performance in braided pneumatic muscle actuators," *The International Journal of Robotics Research*, *22*(3-4), 213-227.

Den Hartog, J. P., 1985. *Mechanical Vibrations*, Dover Publication, Mineola, NY.

Deng, H. X., Gong, X. L., and Wang, L. H., 2006. "Development of an adaptive tuned vibration absorber with magnetorheological elastomer," *Smart materials and structures*, *15*(5), N111.

Du Plooy, N. F., Heyns, P. S., and Brennan, M. J., 2005. "The development of a tunable vibration absorbing isolator," *International Journal of Mechanical Sciences, 47*(7), 983-997.

Esmailzadeh, E., and Jalili, N., 1998. "Optimum design of vibration absorbers for structurally damped Timoshenko beams," *ASME Journal of Vibration and Acoustics*, 120, 833-841.

Ewins, D. J., 1995. *Modal testing: theory and practice*. 52-55 Taunton: Research Studies Press.

Frahm, H., 1911. "Device for damping vibrations of bodies," *US Patent 989,958*.

Fu, Z. F., and He, J., 2001. *Modal analysis*. Butterworth-Heinemann.

Gandhi, M. V. and Thompson B. S., 1992. *Smart materials and structures*, Chapman & Hall, London, UK.

Gao, H., Kwok, K. C. S., and Samali, B., 1997. "Optimization of tuned liquid column dampers," *Engineering structures*, *19*(6), 476-486.

Gere, J. M., and Timoshenko, S. P., 1997. *Mechanics of Materials*, PWS Pub. Co., Boston.

Hagood, N. W., and von Flotow, A., 1991. "Damping of structural vibrations with piezoelectric materials and passive electrical networks," *Journal of Sound and Vibration*, *146*(2), 243-268.

Halwes, D. R., 1980. "LIVE–liquid inertia vibration eliminator," In *American Helicopter Society 36th Annual Forum, Washington, DC*.

Harris, C. M., and Piersol, A. G., 2002. *Harris' Shock and Vibration Handbook* (Vol. 5). McGraw-Hill.

Hashin, Z. and Rosen, B. W., 1964. "The elastic moduli of fiber-reinforced materials," *Journal of Applied Mechanics*, Transactions ASME, 31, 223–232.

Hiemenz, G. J., Hu, W., and Wereley, N. M., 2008. "Semi-active magnetorheological helicopter crew seat suspension for vibration isolation," *Journal of Aircraft, 45*(3), 945-953.

Hodgson, D. A., and Duclos, T. G., 1990. *U.S. Patent No. 4,969,632*. Washington, DC: U.S. Patent and Trademark Office.

Hollkamp, J. J., 1994. "Multimodal passive vibration suppression with piezoelectric materials and resonant shunts," *Journal of Intelligent Material Systems and Structures, 5*(1), 49-57.

Hollkamp, J. J., and Starchville, T. F. Jr., 1994. "A self-tuning piezoelectric vibration absorber," *Journal of Intelligent Material Systems and Structures, 5*(4), 559-566.

Housner, G. W., Bergman, L. A., Caughey, T. K., Chassiakos, A. G., Claus, R. O., Masri, S. F., Skelton, R. E., Soong, T. T., Spencer, B. F., and Yao, J. T. P., 1997. "Structural control: past, present, and future," *Journal of Engineering Mechanics, 123*(9), 897-971.

Hunt, J. B., and Nissen, J. C., 1982. "The broadband dynamic vibration absorber," *Journal of sound and vibration, 83*(4), 573-578.

Ibrahim, R. A., 2008. "Recent advances in nonlinear passive vibration isolators," *Journal of sound and vibration, 314*(3), 371-452.

Igusa, T., and Xu, K., 1994. "Vibration control using multiple tuned mass dampers," *Journal of sound and vibration*, *175*(4), 491-503.

Jacquot, R. G., 1978. "Optimal dynamic vibration absorbers for general beam systems," *Journal of Sound and Vibration*, *60*(4), 535-542.

Jalili, N., 2002. "A comparative study and analysis of semi-active vibration control systems," *Journal of vibration and acoustics*, *124*(4), 593-605.

Johnson, C. D., 1995. "Design of passive damping systems," *Journal of Vibration and Acoustics*, Vol. 117, Special 50th Anniversary Design Issue, pp 171-176.

Jones, P. J., and Downing, M. W., 1993. *U.S. Patent No. 5,197,692*. Washington, DC: U.S. Patent and Trademark Office.

Karnopp, D., 1995. "Active and semi-active vibration isolation," *Journal of Mechanical Design*, *117*(B), 177-185.

Karnopp, D., Crosby, M. J., and Harwood, R. A., 1974. "Vibration control using semi-active force generators," *Journal of Engineering for Industry, 96*, 619.

Kim, S. M., Elliott, S. J., and Brennan, M. J., 2001. "Decentralized control for multichannel active vibration isolation," *Control Systems Technology, IEEE Transactions on, 9*(1), 93-100.

Kitis, L., Wang, B. P., and Pilkey, W. D., 1983. "Vibration reduction over a frequency range," *Journal of Sound and Vibration, 89*(4), 559-569.

Koo, J. H., Ahmadian, M., Setareh, M., and Murray, T., 2004. "In search of suitable control methods for semi-active tuned vibration absorbers," *Journal of Vibration and Control*, *10*(2), 163-174.

Kothera, C.S., Jangid, M., Sirohi, J. and Wereley, N. M., 2009. "Experimental characterization and static modeling of McKibben actuators," *ASME Journal of Mechanical Design*, 131, p.10.

Kundu, P. K., and Cohen, I. M., 2004. *Fluid Mechanics*, Boston: Elsevier Academic Press.

Lam, M. J., Inman, D. J., and Saunders, W. R., 1997. "Vibration control through passive constrained layer damping and active control," *Journal of Intelligent Material Systems and Structures, 8*(8): 663-677.

Lee, S., and Sinha, A., 1986. "Design of an active vibration absorber," *Journal of Sound Vibration*, 109, 347-352.

Lekhnitskii, S.G., 1963. *Theory of elasticity of an anisotropic body*, Holden-Day Inc., San Francisco, CA.

Li, S., and Wang, K. W., 2012. "On the dynamic characteristics of biological inspired multicellular fluidic flexible matrix composite structures," *Journal of Intelligent Material Systems and Structures, 23*(3): 291-300.

Li, S., and Wang, K. W.. 2013. "Synthesizing fluidic flexible matrix composite–based multicellular adaptive structure for prescribed spectral data," *Journal of Intelligent Material Systems and Structures* : 1045389X13505254.

Lin, J. C., and Nien, M. H., 2005. "Adaptive control of a composite cantilever beam with piezoelectric damping-modal actuators/sensors," *Composite Structures*, Vol. 70, No. 2, pp. 170-176.

Lin, J., and Liu, W. Z., 2006. "Experimental evaluation of a piezoelectric vibration absorber using a simplified fuzzy controller in a cantilever beam," *Journal of sound and vibration*, *296*(3), 567-582.

Liu, W. and Rahn, C., 2003. "Fiber-reinforced membrane models of McKibben actuators," *Journal of Applied Mechanics, Transactions ASME*, *70*(6), pp. 853-859.

Lotfi-Gaskarimahalle A., Scarborough III, L. H., Rahn, C. D., and Smith, E. C., 2009. "Fluidic composite tuned vibration absorbers," *ASME conference on Smart Materials, Adaptive Structures and Intelligent Systems*, 2009- 1349, September 21-23, 2009, Oxnard, CA.

Makris, N., and Constantinou, M. C., 1992. "Spring–viscous damper systems for combined seismic and vibration isolation," *Earthquake Engineering & Structural Dynamics*, *21*(8), 649-664.

McGuire, D. P., 2003. "High stiffness ("rigid") helicopter pylon vibration isolation systems," *American Helicopter Society 59th Annual Forum*, Phoenix, Arizona.

Merritt, H. E., 1967. *Hydraulic control systems*, New York: Wiley.

Miller, L. R., 1988. "Tuning passive, semi-active, and fully active suspension systems," *IEEE Proceedings of the 27th Conference on Decision and Control*, pp. 2047-2053.

Nakra, B. C., 1998. "Vibration control in machines and structures using viscoelastic damping," *Journal of Sound and Vibration*, 211(3), 449-465.

Ormondroyd, J., and Den Hartog J., 1928. "The theory of the dynamic vibration absorber," *ASME Transactions – Applied Mechanics, 50*(17), 9-22.

Özgüven, H. N., and Candir, B., 1986. "Suppressing the first and second resonances of beams by dynamic vibration absorbers," *Journal of Sound and Vibration, 111*(3), 377-390.

Philen, M., 2011. "Semi-active vibration isolation using fluidic flexible matrix composite mounts: Analysis and experiment", *Proceedings of SPIE – The International Society for Optical Engineering*, 7977, p. 797709.

Philen, M., Shan, Y., Bakis, C., Wang, K., and Rahn, C., 2006. "Variable stiffness adaptive structures utilizing hydraulically pressurized flexible matrix composites with valve control," in AIAA/ASME/ASCE/AHS/ASC Structures, *Structural Dynamics and Materials Conference*, vol. 9, pp. 6387-6397.

Philen, M., Shan, Y., Prakash, P., Wang, K., Rahn, C., Zydney, A. and Bakis, C., 2007. "Fibrillar network adaptive structure with ion-transport actuation," *Journal of Intelligent Material Systems and Structures*, 18(4), pp. 323-334.

Preumont, A., 2002. *Vibration Control of Active Structures: An Introduction*, 2nd Edition, Kluwer Academic Publishers, Dordrecht.

Rana, R., and Soong, T. T., 1998. "Parametric study and simplified design of tuned mass dampers," *Engineering Structures, 20*(3), 193-204.

Rao, S. S., and Yap, F. F., 1995. *Mechanical Vibrations* (Vol. 4). New York: Addison-Wesley.

Rita, A. D., McGarvey, J. H., and Jones, R., 1978. "Helicopter rotor isolation evaluation utilizing the dynamic antiresonant vibration isolator," *Journal of the American Helicopter Society*, *23*(1), 22-29.

Rivin, E. I., 1995. "Vibration isolation of precision equipment," *Precision Engineering*, *17*(1), 41-56.

Rivin, E. I., 2003. *Passive Vibration Isolation*, ASME press, New York.

Roberson, R. E., 1952. "Synthesis of a nonlinear dynamic vibration absorber," *Journal of the Franklin Institute*, *254*(3), 205-220.

Rusovici, R., Dosch, J. J., and Lesieutre, G. A., 2002. "Design of a single-crystal piezoceramic vibration absorber," *Journal of Intelligent Material Systems and Structures*, *13*(11), 705-712.

Sadek, F., Mohraz, B., and Lew, H. S., 1998. "Single-and multiple-tuned liquid column dampers for seismic applications," *Earthquake Engineering and Structural Dynamics*, *27*(5), 439-464.

Sakai, F., Takaeda, S., and Tamaki, T., 1989. "Tuned liquid column damper-new type device for suppression of building vibrations," In *Proceedings of International Conference on Highrise Buildings*, pp. 926-931.

Scarborough, L., Rahn, C., and Smith, E., 2012. "Fluidic composite tunable vibration isolators," *ASME Journal of Vibration and Acoustics*, Vol. 134, 011010.

Schwarz, B. J., and Richardson, M. H., 1999. "Experimental modal analysis," *CSI Reliability Week, 36*(3), 30-32.

Sciulli, D., 1997. *Dynamics and Control for Vibration Isolation Design* (Doctoral dissertation, Virginia Polytechnic Institute and State University, Blacksburg, VA.).

Sciulli, D., and Inman, D. J., 1998. "Isolation design for a flexible system," *Journal of Sound and Vibration*, *216*(2), 251-267.

Shan, Y., 2006. *Flexible Matrix Composites: Dynamic Characterization, Modeling, and Potential for Driveshaft Applications* (Doctoral dissertation, Pennsylvania State University, University Park, PA)

Shan, Y., Philen M., Bakis, C., Wang, K., and Rahn, C., 2006. "Nonlinear-elastic finite axisymmetric deformation of flexible matrix composite membranes under internal pressure and axial force," *Composites Science and Technology*, 66(15), pp. 3053-3063.

Shan, Y., Philen, M., Lotfi, A., Li, S., Bakis, C. E., Rahn, C. D., and Wang, K. W., 2009. "Variable stiffness structures utilizing fluidic flexible matrix composites," *Journal of Intelligent Material Systems and Structures,* 20, pp. 443-456.

Smith, M. R., and Redinger, W. S., 1999. "The model 427 pylon isolation system," *American Helicopter Society 55th Annual Forum*, Vol. 1, pp. 195-201.

Smith, M. R., and Stamps, F. B., 1995. *U.S. Patent No. 5,435,531*. Washington, DC: U.S. Patent and Trademark Office.

Snowdon, J. C., 1966. "Vibration of cantilever beams to which dynamic absorbers are attached," *The Journal of the Acoustical Society of America*, *39*(5A), 878-886.

Soong, T. T., and Constantinou, M. C., 1994. *Passive and Active Structural Vibration Control in Civil Engineering*, Springer: Vienna and New York.

Soong, T. T., and Dargush, G. F., 1997. *Passive Energy Dissipation Systems in Structural Engineering*, Wiley, New York.

Sun, C. T., and Li, S., 1988. "Three dimensional effective elastic constants for thick laminates," *Journal of Composite Materials*, 22(7), pp. 629-645.

Sun, J. Q., Jolly, M. R., and Norris, M. A., 1995. "Passive, adaptive and active tuned vibration absorbers: a survey," *Journal of mechanical design*, *117*(B), 234-242.

Tondu, B., and Lopez, P., 2000. "Modeling and control of McKibben artificial muscle robot actuators," *Control Systems, IEEE*, *20*(2), 15-38.

Tsagarakis, N., and Caldwell, D., 2000. "Improved modeling and assessment of pneumatic muscle actuators," *Proceedings of ICRA*, vol. 4, pp. 3641-3646.

Tsai, M. S., and Wang, K. W., 1999. "On the structural damping characteristics of active piezoelectric actuators with passive shunt," *Journal of Sound and Vibration*, 221, 1-22.

Vashisth, A., Zhu, B., Bakis, C. E., and Rahn, C. D., 2013. "Evaluation of millimeter-size fluidic flexible matrix composite tubes," *ASME SMASIS2013*, 3344, Snowbird, Utah.

Viana, F. A. C., and Steffen Jr, V., 2006. "Multimodal vibration damping through piezoelectric patches and optimal resonant shunt circuits," *Journal of the Brazilian Society of Mechanical Sciences and Engineering*, *28*(3), 293-310.

Walsh, P. L., and Lamancusa, J. S., 1992. "A variable stiffness vibration absorber for minimization of transient vibrations," *Journal of Sound and Vibration*, *158*(2), 195-211.

Williams, K., Chiu, G., and Bernhard, R., 2002. "Adaptive-passive absorbers using shape-memory alloys," *Journal of Sound and Vibration*, *249*(5), 835-848.

Wimmer, B. M., Zhu, B., Bakis, C. E., and Rahn, C. D., 2012. "Actuation Behavior of Multi-layer Flexible Matrix Composite Tubes with Internal Pressurization," *Proc. SAMPE 2012 Conference and Exposition*, Society for the Advancement of Materials and Process Engineering, Covina, CA, 2012, 15 p. (CD-ROM).

Woods, B.K.S., Kothera, C.S., Sirohi, J., and Wereley, N.M., 2011. "Pneumatic artificial muscles for trailing edge flap actuation: a feasibility study". *Smart Materials and Structures*, 20(10), 105021.

Yalla, S. K., and Kareem, A., 2000. "Optimum absorber parameters for tuned liquid column dampers," *Journal of Structural Engineering*, *126*(8), 906-915.

Yalla, S. K., and Kareem, A., 2003. "Semiactive tuned liquid column dampers: experimental study," *Journal of Structural Engineering*, *129*(7), 960-971.

Young, D., 1952. "Theory of dynamic vibration absorbers for beams," In *Proceedings of the First US National Congress of Applied Mechanics*, pp. 91-96.

Zhang, Z., and Philen, M., 2012. "Pressurized artificial muscles," *Journal of Intelligent Material Systems and Structures*, *23*(3), 255-268.

Zhang, Z., Philen, M., and Neu, W., 2010. "A biologically inspired artificial fish using flexible matrix composite actuators: analysis and experiment," *Smart Materials and Structures*, *19*(9), 094017.

Zhu, B., Rahn, C. D., and Bakis, C. E., 2011. "Tailored fluidic composites for stiffness or volume change," *ASME SMASIS2011- 4962*, Scottsdale, AZ.

Zhu, B., Rahn, C. D., and Bakis, C. E., 2012. "Actuation of fluidic flexible matrix composites in structural media," *Journal of Intelligent Material Systems and Structures*, *23*(3): 269-278.

Zupan, M., Ashby, M. F., and Fleck, N. A., 2002. "Actuator classification and selection—the development of a database," *Advanced Engineering Materials*, *4*(12), 933-940.

VITA

Bin Zhu

EDUCATION

The Pennsylvania State University, University Park, PA (*August, 2014*)
Ph.D. Mechanical Engineering, Minor in Engineering Mechanics
The Pennsylvania State University, University Park, PA (*May, 2013*).
M.S. Mechanical Engineering
Hong Kong University of Science & Technology, Hong Kong (*Fall 2007*)
Exchange Student in Mechanical Engineering
Xi'an JiaoTong University, Xi'an, China (*July, 2009*)
B.S. in Mechanical Engineering and Automation

HONORS AND AWARDS

- **Kulakowski Travel Award**, University Park, Pennsylvania, 2013.
- **Graduate of the Year** in Dept. of Mechanical Engineering at XJTU, Xi'an, China, 2009.
- **Cyrus Tang Scholarships** from Cyrus Tang Foundation, Xi'an, China, 2005 ~ 2008.
- **Dean's List** in College of Engineering at HKUST, Hong Kong, 2007.
- **Bekaert Enterprise Award**, Xi'an, China, 2007.

PUBLICATIONS

[1] **B. Zhu**, C. D. Rahn, and C. E. Bakis, "Fluidic Flexible Matrix Composite Damping Treatment for a Cantilever Beam," submitted to *Journal of Sound and Vibration*. (April, 2014)

[2] **B. Zhu**, C. D. Rahn, and C. E. Bakis, "Fluidic Flexible Matrix Composite Vibration Absorber for a Cantilever Beam," submitted to *Journal of Vibration and Acoustics*. (April, 2014)

[3] **B. Zhu**, C. D. Rahn, and C. E. Bakis, "Design of a Fluidic Flexible Matrix Composite Damping Treatment for a Cantilever Beam," *American Society for Composites 28th Technical Conference*. (2013)

[4] **B. Zhu**, C. D. Rahn, and C. E. Bakis, "Tunable Vibration Absorption of a Cantilever Beam Utilizing Fluidic Flexible Matrix Composites," *ASME International Design Engineering Technical Conference*. (2013)

[5] A. Vashisth, **B. Zhu**, B. M. Wimmer, C. E. Bakis, and C. D. Rahn, "Evaluation of Millimeter Size Fluidic Flexible Matrix Composite Tubes," *ASME Conference on Smart Materials, Adaptive Structures and Intelligent Systems*. (2013)

[6] **B. Zhu**, C. D. Rahn, and C. E. Bakis, "Vibration Damping of a Cantilever Beam Utilizing Fluidic Flexible Matrix Composites," *SPIE Smart Structures/NDE Conference*. (2013)

[7] B. M. Wimmer, **B. Zhu**, C. E. Bakis, and C. D. Rahn, "Actuation Behavior of Multi-layer Flexible Matrix Composite Tubes with Internal Pressurization," *Society for the Advancement of Materials and Process Engineering Conference*. (2012)

[8] **B. Zhu**, C. D. Rahn, and C. E. Bakis, "Actuation of fluidic flexible matrix composites in structural media," *Journal of Intelligent Material Systems and Structures*. (2012)

[9] **B. Zhu**, C. D. Rahn, and C. E. Bakis, "Tailored Fluidic Composites for Stiffness or Volume Change," *ASME Conference on Smart Materials, Adaptive Structures and Intelligent Systems*. (2011)